2010, VOLUME 3

PROGRESS IN PHYSICS

"All scientists shall have the right to present their scientific research results, in whole or in part, at relevant scientific conferences, and to publish the same in printed scientific journals, electronic archives, and any other media." — Declaration of Academic Freedom, Article 8

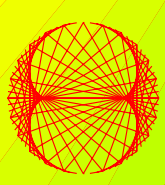

ISSN 1555-5534

The Journal on Advanced Studies in Theoretical and Experimental Physics, including Related Themes from Mathematics

PROGRESS IN PHYSICS

A quarterly issue scientific journal, registered with the Library of Congress (DC, USA). This journal is peer reviewed and included in the abstracting and indexing coverage of: Mathematical Reviews and MathSciNet (AMS, USA), DOAJ of Lund University (Sweden), Zentralblatt MATH (Germany), Scientific Commons of the University of St. Gallen (Switzerland), Open-J-Gate (India), Referativnyi Zhurnal VINITI (Russia), etc.

To order printed issues of this journal, contact the Editors. Electronic version of this journal can be downloaded free of charge:
http://www.ptep-online.com

Postal address

Department of Mathematics and Science,
University of New Mexico,
200 College Road,
Gallup, NM 87301, USA

ISSN: 1555-5534 (print)
ISSN: 1555-5615 (online)

Standard Address Number: 297-5092
Printed in the United States of America

JULY 2010 **VOLUME 3**

CONTENTS

Information for Authors and Subscribers

Progress in Physics has been created for publications on advanced studies in theoretical and experimental physics, including related themes from mathematics and astronomy. All submitted papers should be professional, in good English, containing a brief review of a problem and obtained results.

All submissions should be designed in LaTeX format using *Progress in Physics* template. This template can be downloaded from *Progress in Physics* home page http://www.ptep-online.com. Abstract and the necessary information about author(s) should be included into the papers. To submit a paper, mail the file(s) to the Editor-in-Chief.

All submitted papers should be as brief as possible. We accept brief papers, no larger than 8 typeset journal pages. Short articles are preferable. Large papers can be considered in exceptional cases to the section *Special Reports* intended for such publications in the journal. Letters related to the publications in the journal or to the events among the science community can be applied to the section *Letters to Progress in Physics*.

All that has been accepted for the online issue of *Progress in Physics* is printed in the paper version of the journal. To order printed issues, contact the Editors.

This journal is non-commercial, academic edition. It is printed from private donations. (Look for the current author fee in the online version of the journal.)

Calibration of Microwave Reference Blackbodies and Targets for Use in Satellite Observations: An Analysis of Errors in Theoretical Outlooks and Testing Procedures

Pierre-Marie Robitaille

Department of Radiology, The Ohio State University, 395 W. 12th Ave, Suite 302, Columbus, Ohio 43210, USA
E-mail: robitaille.1@osu.edu

Microwave reference blackbodies and targets play a key role in astrophysical and geophysical studies. The emissivity of these devices is usually inferred from return-loss experiments which may introduce at least 10 separate types of calibration errors. The origin of these inaccuracies depends on test conditions and on the nature of each target. The most overlooked errors are related to the geometry adapted in constructing reference loads and to the effects of conduction or convection. Target shape and design can create an imbalance in the probabilities of absorption and emission. This leads to loss of radiative equilibrium, despite the presence of a thermodynamic steady state. Heat losses or gains, through conduction and convection, compensate for this unexpected physical condition. The improper calibration of blackbodies and targets has implications, not only in global climate monitoring, but also relative to evaluating the microwave background.

1 Introduction

Blackbodies [1–4] can be difficult to construct and analyze. For example, by unknowingly pumping normal radiation [2, 3] into cavities using their detectors, scientists can easily make the interior of enclosures appear black [4]. They thereby create the illusion that all cavities emit normal radiation [1–3]. Relative to microwave reference targets, the situation is further complicated by the realization that these devices are pseudo-cavities and become subject to geometrical considerations. These problems are important as microwave targets are present on numerous satellites monitoring the microwave background [5–7] and global climate (e.g. [8]).

Calibration targets for microwave frequencies [9–15] are typically made from carbon or iron containing foams and epoxy resins, such as Eccosorb foams and Eccosorb CR-110 and 117 [Emerson and Cuming, Randolph, MA]. Recently, an aqueous blackbody has been proposed for calibration purposes [16]. Such a device takes advantage of the powerful microwave absorbance of water. As for Eccosorb surfaces used in the microwave [5,7], unlike graphite and carbon black paints in the infrared [3, 17–20], they manifest significantly increased absorbance as a function of thickness. Therefore, it is impossible to obtain a blackbody emission from a thin layer of Eccosorb, irrespective of claims to the contrary. For example, a 1 cm layer of Eccosorb CR-110 has an absorbance of only ~6 dB at 18 GHz [21]. Despite this reality, space restrictions aboard spacecraft often limit the volume available for satellite reference targets [7]. Further complicating the situation, these materials permit transmission at microwave frequencies and are not opaque. Consequently, the correct treatment of their properties involves the consideration of transmission. Unfortunately, since reference targets are often backed by highly reflective metal casings [10–15], it becomes easy to ignore the effects of transmission in the absorber. This can lead to a serious overestimation of calibrator emissions, as will be demonstrated.

2 The testing of reference targets

Almost without exception, the testing of microwave reference targets involves their placement within an anechoic chamber (e.g. [10–15]). Here, they are subjected to incident microwave radiation emitted from a test horn, typically driven at the frequency of interest by a network analyzer. This is achieved while making the assumption that the target, with its absorbing material and metal casing (e.g. [10–15]), can be treated as a single opaque unit. By measuring the return-loss produced in this configuration, the emissivity of the target can be inferred, but not without risk of error.

Return loss measurements are based on the validity of Stewart's formulation, which advances the equivalence of emission and absorption under conditions of thermal equilibrium [22, 23]. This statement is commonly viewed by the scientific community as Kirchhoff's law [1]. However, Kirchhoff's law differs from Stewart's formulation by advocating that all radiation within cavities must be black. Such a concept is demonstrably false [4, 17, 23]. As a result, the law of equivalence between emissivity and absorptivity, must be attributed uniquely to Stewart [22, 23].

The emissivity of a target is usually estimated through the relationship $\varepsilon_t = 1 - \sigma_{tn}$, where ε_t and σ_{tn} represent target emissivity and normal reflectivity, respectively (i.e. [10–15]. This treatment assumes that only normal reflection takes place and also constitutes an implicit formulation of Stewart's law [23]. Nonetheless, in this discussion, we will consider the

measurement of absorption, rather than emission, and write $\kappa_t = 1 - \sigma_{tn}$, where κ_t represents the absorptivity of the target. In the end, it is demonstrated that the measurement of absorptivity from return loss measurements in no way implies that the emissivity of the target has been properly evaluated.

2.1 Type-1, -2, -3 and -4 errors

The first error in the determination of emissivity using return loss measurements, involves leakage of incident radiation from the horn, directly into the anechoic chamber, without ever striking the target. This will be referred to as a Type-1 error (see Figure 1A) and symbolized as Γ_{bp}, as it depends on the beam pattern of the horn. Type-2 errors can occur when incident radiation is diffracted around the edges of the horn on transmission, as shown in Figure 1A. Type-2 errors will be symbolized as Γ_{dh} as they represent diffraction on the horn. These errors are also associated with the beam pattern. Since corrugated edging can be placed on a horn to minimize the effects of diffraction, it is treated as a separate error. Type-3 errors are similar in nature to Type-2 errors, but involve the diffraction of incoming radiation on the edges of the target, Γ_{dt}. This term also includes radiation which is scattered by the target. Finally, a Type-4 error results from the neglect of diffuse reflection off the target surface, σ_{td}.

Each of these error types result in radiation being lost to the walls of the anechoic chamber. Such radiation will not be available to the horn and will subsequently contribute to lowering the measured return radiation. In order to overcome this problem, it is important to numerically evaluate the beam pattern of the horn, thereby inferring the percentage of incident radiation that does, in fact, strike the target. It is also possible to place pick-up horns in the anechoic chamber and evaluate the beam patterns directly, in the absence of a target. Thus, whether through calculations or direct measurement, the magnitude of these errors can be understood and are usually properly addressed. Nonetheless, and for the sake of completeness, it is clear that the absorptivity of the target is actually given by:

$$\kappa_t = 1 - \sigma_{tn} - \sigma_{td} - \Gamma_{bp} - \Gamma_{dh} - \Gamma_{dt} \,. \qquad (1)$$

When viewing the target as a single unit, Type-1, -2, -3, and -4 errors can lead to the inaccurate assessment of target emissivity from return-loss experiments. Yet, it is the effect of using a transmissive absorber, in the presence of a metal casing or support, which can lead to the greatest errors in evaluating emissivity.

2.2 Type-5 and -6 errors

The emissivity of microwave targets is exclusively dominated by an absorbing material, like Eccosorb, which is also transmissive [9, 21]. Accordingly, it is unwise to treat these devices as single units. Instead, clearer insight into the problem can be gained if one views the target as made from its two components: the absorbent material and the perfectly reflective metallic backing. In this scenario, the absorbent material can be considered as possessing absorptivity, κ_a, and emissivity, ε_a, equal to one another ($\kappa_a = \varepsilon_a$), along with normal reflectivity, σ_{an}, diffuse reflectivity, σ_{ad}, and transmissivity, τ_a. The metallic casing, c, often constructed from aluminum, is viewed as having perfect reflectivity ($\sigma_c = 1$).

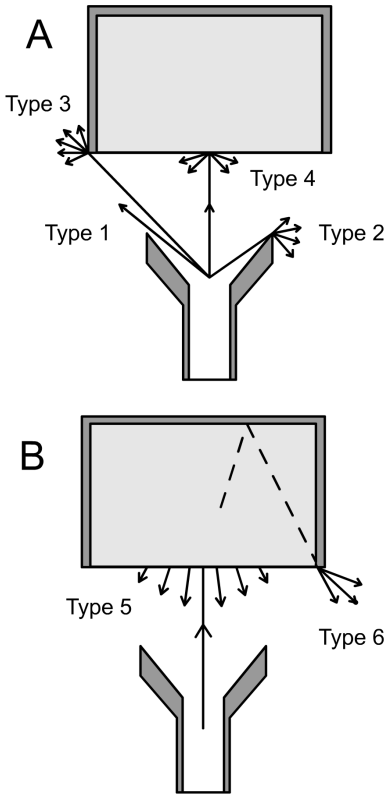

Fig. 1: Schematic representation of error types when assessing effective emissivity using return-loss measurements.

Under such conditions, the difficulties in ascertaining the emissivity of the target become evident, since for any non-opaque substance, $\varepsilon = 1 - \sigma - \tau$, rather than $\varepsilon = 1 - \sigma$. Because the absorber has transmittance, it can permit microwave energy to pass through its body and strike the metallic backing at virtually any angle. While an object transmits incident radiation, it is not required to preserve either phase or angle of incidence. As such, when the transmitted component strikes the casing, it can do so in a manner whereby the microwave energy, following reflection, re-enters the absorber only to be absorbed, transmitted towards the horn, scattered into space, or diffracted by the edge of the casing. This would lead to a good return-loss measurement on the network analyzer; but it would be improper to assume that $\varepsilon = 1 - \sigma$. Therefore, it becomes nearly impossible to measure emissivity, as will be demonstrated.

In reality, by treating the target as an opaque unit made up of two components (i.e. the absorber and the reflective

casing), it is apparent that its absortivity is now given by:

$$\kappa_t = 1 - \sigma_{an} - \sigma_{ad} - \Gamma_{bp} - \Gamma_{dh} - \Gamma_{dc} - \\ - \kappa_a \tau_a \sigma_c - \tau_a \tau_a \sigma_c - s_a \tau_a \sigma_c - d_a \tau_a \sigma_c \,, \quad (2)$$

where the normal and diffuse reflection of the absorber are now being considered (σ_{an} and σ_{ad}), along with the diffraction of incident radiation on the casing, Γ_{dc} (previously viewed as Γ_{dt}), and four new terms arise, whose coefficients sum to 1 (i.e. $\kappa_a + \tau_a + s_a + d_a = 1$). The seventh term, $\kappa_a \tau_a \sigma_c$, corresponds to that fraction of transmitted power which is reflected by the casing, σ_c, and absorbed, κ_a, upon reentry into the absorber. The eighth term, $\tau_a \tau_a \sigma_c$, represents that fraction of the transmitted power which is reflected by the casing and is subsequently re-transmitted, τ_a, towards the horn. The seventh term, like the eighth term, has been innocently considered when treating the target as an opaque unit in section 2.1. These terms introduce no errors in the return-loss measurement itself. For instance, it is evident that, with rearrangement, Eq. (2) becomes:

$$\kappa_{t_{\text{eff}}} = (\kappa_t + \kappa_a \tau_a \sigma_c) = 1 - (\sigma_{an} + \tau_a \tau_a \sigma_c) - \sigma_{ad} - \\ - \Gamma_{bp} - \Gamma_{dh} - \Gamma_{dc} - s_a \tau_a \sigma_c - d_a \tau_a \sigma_c \,. \quad (3)$$

In this expression, the seventh term in Eq. (2), $\kappa_a \tau_a \sigma_c$, is moved to the left as it makes a positive contribution to the effective absorptivity of the target, where on measurement, κ_t is indistinguishable from $\kappa_a \tau_a \sigma_c$. Unfortunately, we must now consider the effective absorptivity, $\kappa_{t_{\text{eff}}}$, from the target. In fact, the seventh term, $\kappa_a \tau_a \sigma_c$, brings such difficulty in the determination of emissivity that it will be considered below separately as a Type-7 problem. This occurs as the targets permit repeated cycles of absorption and reflection. The associated Type-7 errors experience geometric growth. It is also clear that, in Eq. (2), the eighth term, $\tau_a \tau_a \sigma_c$, can be paired with normal reflection, σ_{an}, the two being indistinguishable.

The ninth term in Eq. (2), $s_a \tau_a \sigma_c$, generates a Type-5 error as shown in Figure 1B. It accounts for that fraction of the transmitted power which is reflected by the casing, re-enters the absorber, and is then scattered, s_a, into the anechoic chamber. The term resembles a Type-4 error, σ_{td}, involving the effect of diffuse reflection when considering the entire target. However, it is not diffuse reflection, though indistinguishable from such a process. It is properly viewed, as a Type-5 error, as it involves scattering by the absorber following reflection on the casing.

Finally, the tenth term in Eq. (2), $d_a \tau_a \sigma_c$, introduces a Type-6 error. It corresponds to that fraction of the transmitted power which is reflected by the aluminum casing, re-enters the Eccosorb and is then diffracted, d_a, by the edge of the casing into the anechoic chamber (see Figure 1B). The tenth term involves diffraction on the casing from a direction opposite to the incident radiation. It resembles a Type-3 error, Γ_{dc} (previously referred to as Γ_{dt}), in being indistinguishable from it on measurement, but is distinct in its origin. It is really a "reverse diffraction" since it is produced from radiation which was previously reflected by the metallic casing. It will be properly viewed as a Type-6 error. The distinction is important because, while corrugations can be placed on horns to minimize diffractions on their edges during transmission, they are often not present on the metallic casings of their reference targets [7]. Hence, the diffraction produced as radiation exits the interior of the target is often ignored [7].

If we now represent the seventh through the tenth terms as $\Gamma_{\kappa\sigma}$, $\Gamma_{\tau\sigma}$, $\Gamma_{s\sigma}$, and $\Gamma_{d\sigma}$, Eq. (2) can be re-expressed, with pairing of indistinguishable terms, as follows:

$$\kappa_{t_{\text{eff}}} = (\kappa_t + \Gamma_{\kappa\sigma}) = 1 - (\sigma_{an} + \Gamma_{\tau\sigma}) - (\sigma_{ad} + \Gamma_{s\sigma}) - \\ - (\Gamma_{bp} + \Gamma_{dh}) - (\Gamma_{dc} + \Gamma_{d\sigma}) \,. \quad (4)$$

2.3 Type-7 errors

The most serious problem with microwave target return-loss measurements can be viewed as Type-7 errors which involve the geometry of the targets themselves. This problem exists in all determinations of emissivity from return-loss measurements in the presence of a metal casing. In reality, we are returning to the $\kappa_a \tau_a \sigma_c$, or $\Gamma_{\kappa\sigma}$ term. As previously mentioned, this term does not lead to an error in the return-loss measurement. But, it can cause an enormous error in the determination of emissivity from such measurements. This is a geometric effect, which is best understood by considering targets of varying geometry.

2.3.1 The Planck LFI

Consider, for instance, the target geometry for the ~4 K references on the Planck LFI [7]. These targets are box-like in appearance. They are composed of various layers of Eccosorb, including a small pyramid, enclosed on 5 sides by an aluminum casing (see Figures 8, 10 and 12 in [7]). Given incident radiation from the test horn and neglecting Type-1 through -4 errors, the layer of Eccosorb can initially absorb some of the microwave power. The radiation which is not absorbed is transmitted through the Eccosorb and strikes the aluminum casing. At this point, it ideally experiences normal reflection on the casing and travels back through the absorber. If this radiation is not absorbed following reentry, it travels into space. There, neglecting Type-5 and -6 errors, it can be detected by the horn and registered as return radiation. Note that, now, there are two chances for the incident microwave radiation to be absorbed: first on incidence and then following reflection on the metal casing (term $\kappa_a \tau_a \sigma_c$ above). The situation is not balanced on emission.

Relative to pure emission, the absorber is unable to provide the same performance. For instance, microwaves emitted from the upper surface of the absorber can travel uninterrupted towards the detector. Conversely, radiation emitted through the lower surface of the absorber immediately encounters reflection on striking the metal casing and then re-

enters the material of origin. Once in the absorber, the radiation which had been emitted from the lower surface has a chance of being absorbed before exiting towards the test horn. Furthermore, it is unlikely that the lower surface of such a test target can emit any photons towards the casing, since conduction is also taking place at the interface of the Eccosorb and the aluminum casing (see section 2.4). The effective emissivity, ε_{eff}, of the absorber is reduced by the presence of the metal casing, whereas the effective absorptivity, κ_{eff}, is being increased.

Speaking in quantum mechanical terms, the presence of the metal casing has created a condition where the probability of absorption is no longer equal to the probability of emission. Herein lays the major flaw associated with such approaches. Geometry has produced a condition where return-loss measurements can no longer properly evaluate the effective emissivity of the target. The effective absorbtivity has been enhanced by geometry and the effective emissivity reduced. This is a Type-7 error. Effective radiative equilibrium is being destroyed by geometry and $\varepsilon_{\text{eff}} \neq \kappa_{\text{eff}}$. This occurs precisely because the highly conductive metallic casing ensures that thermodynamic steady state remains. Conduction now compensates for the imbalance created in effective absorptivity and emissivity. In fact, conduction and convection can introduce Type-8 and 9 errors, respectively, as will be discussed in section 2.4.

2.3.2 Pyramidal targets

In order to emphasize the effect of geometry, consider a target where a metal casing is built, composed of a group of small pyramidal structures [10–12]. Such targets are important on geophysical satellites and in radiometry standards laboratories [8, 10–12]. In these targets, each pyramid is about 4 cm in height with a 1×1 cm base [10–12]. A large array of such pyramids, coated with a thin layer of absorber, will form the target. Often, the aluminum casing supports a thin layer of Eccosorb, as seen in the ARIS instrument [8] and other calibration sources [10–12]. In Figure 2A and B, a section of these calibrators is expanded, displaying only the valley created by two adjacent pyramids. Figure 2A treats the situation experienced in measuring absorption from such a target. Conversely, in Figure 2B, emission from a small surface element, at the bottom of the valley, is being considered. In order to simplify the presentation, only absorption and emission towards or away from a single element at the bottom of the valley is considered.

Thus, when radiation is incident on such a structure (see Figure 2A), it has an initial probability of being absorbed when it first enters the Eccosorb, P_1. If the radiation is not absorbed at this interface, it is transmitted to the metal casing where it is immediately reflected. At this point, the radiation re-enters the Eccosorb, where it still has another probability of being absorbed, P_2. Should the photons not be absorbed, the radiation travels to the adjacent pyramid. Here, once again, it has a probability of being absorbed, P_3. This scenario continues through many reflections and absorptions. As the photons travel towards the element at the bottom of the valley, a tremendous increase in the probability of being absorbed is generated. This effective absorptivity is made up of the sum of all individual absorption probabilities created from geometry in the presence of the casing. Because of repeated chances of absorption and reflection, the total probability for effective absorptivity, κ_{eff}, is tremendous as shown in Table 1. In fact, this represents geometric growth. For instance, if one permits a total of 8 interactions with the Eccosorp on the way to the small element (9 interactions in total), any photon will have nearly an 87% chance of being absorbed even if the emissivity of the Eccosorb layer (in isolation) was only 0.2. To make matters worse, if that same photon then tries to leave the valley, it must do so while dealing with the probabilities of absorption on exit. Other examples are provided in Table 1. Of course, the effective absorptivity of the target involves the sum of all probabilities for all photons and for all elements. The path through the Eccosorb layers will also be slightly different with each crossing. Nonetheless, it is easy to visualize why these geometric configurations give such outstanding results for effective absorptivity. This is true, even when extremely thin layers of absorber are placed on the surfaces of the metal casing.

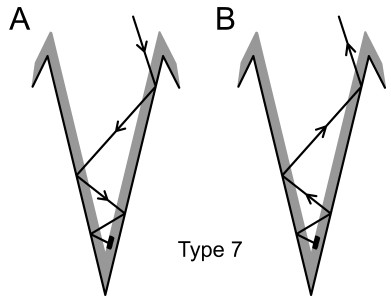

Fig. 2: Schematic representation of geometric, or Type-7 errors, in the assessment of effective emissivity. A) Path of a photon towards an absorptive element at the bottom of the valley. B) Path of a photon emitted by an element at the bottom of the valley. See Table 1 for the effect of geometries on effective emissivity of this element.

Unfortunately, while this situation is outstanding for absorption, it is suboptimal relative to emission. Consequently, a photon produced by a surface element at the bottom of the valley, which is not emitted directly in the direction of the horn, will be subject to repeated chances of being absorbed as it tries to make its way out of this microwave "death valley" (see Table 1). For instance, in considering the reverse path of Figure 2B, we can see that an element with an emissivity of 0.2, will be able to contribute an effective emissivity of only 0.034 after 8 interactions with the Eccosorb (4 changes in direction). Just 4 interactions would more than half the effective emissivity from this element. Once again, the effec-

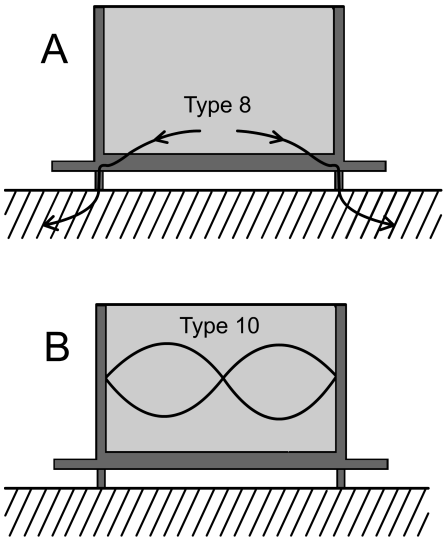

Fig. 3: Schematic representation of A) Type-8, or conductive, errors and B) Type-10, or standing wave errors. These errors can occur when assessing effective emissivity using return-loss measurements.

tive emissivity must include emission over all possible angles. Nonetheless, the situation is unfavorable, as geometry is hindering free emission from most elements.

Moreover, the situation is greatly accentuated if each element of the Eccosorb has a real emissivity of 0.7. In this case, after only 4 interactions with the Eccosorb (2 changes in direction), a photon leaving the bottom of the valley would contribute an effective emissivity of only 0.006. As such, superior absorptive characteristics of the surface absorber lead to inferior performance on effective emission. Furthermore, even a photon emitted near the tips of the pyramid has a chance of doing so in the direction of the valley, not the detector. Such a photon would have almost no chance of escaping the valley. This demonstrates the profoundness of Type-7 errors and the impact of geometry on calibration targets.

It is clear that the probability of absorption or the effective absorptivity, in this geometry, far surpasses the effective emissivity and all return-loss measurements involving such configurations improperly overestimate emission. In fact, rather than building a calibration target which ensures good emission, scientists unknowingly accomplished exactly the opposite. For instance, using infrared imaging, thermal variations in the targets are revealed, wherein the pyramidal tips display a reduced temperature (see Figure 5 in [10]). Such temperature distributions within calibration targets point to the presence of conductive and radiative imbalances which prove that the targets are not black (see section 2.4.1). Figure 5 in [10] constitutes a direct manifestation of Type-7 errors. Relative to emission, it would have been better to provide a very thick surface of Eccosorb. Unfortunately, return-loss measurement would indicate considerable diffuse reflection from such a surface. This had been circumvented by using valleys.

κ_{eff}	κ	N	ε_{eff}	ε	N
0.865	0.2	8	0.034	0.2	8
0.672	0.2	4	0.082	0.2	4
0.488	0.2	2	0.128	0.2	2
0.2	0.2	0	0.2	0.2	0
0.99	0.4	8	0.0067	0.4	8
0.922	0.4	4	0.0518	0.4	4
0.784	0.4	2	0.144	0.4	2
0.4	0.4	0	0.4	0.4	0
0.99998	0.7	8	0.00005	0.7	8
0.9975	0.7	4	0.00567	0.7	4
0.973	0.7	2	0.063	0.7	2
0.7	0.7	0	0.7	0.7	0

Table 1: Summary of calculated effective absorptivity and emissivity. In this table, κ_{eff} represents the effective absorptivity obtained after N interactions of an incoming photon with the absorber and 1 interaction with the element at the bottom of the valley (see Figure 2). It is assumed that Eccosorb is coating the 4×1×1 cm metallic pyramids [10–12]. The process involves geometric growth as given by $\kappa_{\text{eff}} = 1 - (1 - \kappa)^{N+1}$. Similarly, ε_{eff} represents the effective emissivity from a single element obtained after N interactions of an emitted photon with the Eccosorb. If the emitted photon travels directly to the detector, without further interactions with the Eccosorb, then $N = 0$. For effective emissivity, geometric decay is occurring corresponding to $\varepsilon_{\text{eff}} = \varepsilon - \varepsilon[1 - (1 - \kappa)^N]$. As a consequece of thermodynamic steady state, it is assumed that the ability of an individual element to absorb or emit radiation remains equal ($\kappa = \varepsilon$). The total effective emissivity of the target constitutes the summation of effective emissivities over all elements, e, and angles (θ and φ): $\varepsilon_{\text{eff}_T} = \Sigma\Sigma\Sigma\, \varepsilon_{\text{eff}}$.

2.4 Type-8, -9 errors

Type-8 and -9 errors can occur when heat flows out of the target through either conductive or convective paths, respectively. To ensure that radiative heat transfer dominates the equilibrium thermodynamics of the target, it is important to minimize all contacts.

A conductive path out of the reference target created with metallic fixtures can set up a Type-8 error as shown in Figure 3A. In this case, it is possible to produce an imbalance between thermal absorption and emission which immediately renders return-loss measurements invalid.

It is evident that a target bombarded with incident microwave radiation on absorption can dissipate such energy through conduction out of the target. It does not need to resort to emission. In this situation, the effective absorptivity of the target will not be equal to its effective emissivity ($\varepsilon_{\text{eff}} \neq \kappa_{\text{eff}}$), even though thermodynamic steady state is being maintained. This also explains why geometry can produce imbalances in effective emissivity and absorptivity while still maintaining a fixed target temperature.

In theory, a Type-9 error could also be produced, with the same consequences, if convective paths out of the target are

present. Such effects are unlikely to be significant in most scenarios as convective heat transfer is usually ineffective relative to conductive mechanisms.

Consequently, the presence of conduction and convection can introduce two new error terms, Γ_{cond} and Γ_{conv}, such that Eq. (4) now becomes:

$$\kappa_{t_{\text{eff}}} = (\kappa_t + \Gamma_{\kappa\sigma}) = 1 - (\sigma_{an} + \Gamma_{\tau\sigma}) - (\sigma_{ad} + \Gamma_{s\sigma}) - \\ - (\Gamma_{bp} + \Gamma_{dh}) - (\Gamma_{dc} + \Gamma_{d\sigma}) - \Gamma_{\text{cond}} - \Gamma_{\text{conv}} . \quad (5)$$

Conductive and convective errors in target calibration are often not properly addressed and the use of conduction to "cool the target" unwisely advocated [7]. Such approaches highlight elementary errors relative to the understanding of heat transfer. For instance, it is true that conductive paths can be used to heat a target to steady state with all heat being dissipated through radiation. In fact, this was the approach first used to make radiant cavities isothermal [24] in the days which led to Planck's formulation of the blackbody relationship [2, 3]. In this case, conductive paths bring heat into the device which is then forced to escape through radiation. It is quite another matter to permit conductive or convective paths to bring heat out of a target. In the former case, heat leaves the target exclusively through radiation. In the later, it can leave either through radiation or conduction. Accordingly, there is no reason to expect that brightness temperatures in the second setting will be correct.

2.4.1 Max Planck and heat radiation

Relative to this question, Max Planck insists that blackbodies be isolated from the surrounding system. He writes: "*A system of bodies of arbitrary nature, shape, and position which is at rest and is surrounded by a rigid cover impermeable to heat will, no matter what its initial state may be, pass in the course of time into a permanent state, in which the temperature of all bodies of the system is the same. This is the state of thermodynamic equilibrium, in which the entropy of the system has the maximum value compatible with the total energy of the system as fixed by the initial conditions. This state being reached, no further increase in entropy is possible*" [3]. In this treatment, Planck is really making a statement of Prévost's theory of exchanges [25, 26]. However, he is moving beyond Prévost, because he is considering the entropy of the radiation itself. For Planck, the normal spectrum is obtained when the entropy of radiation is maximized [3]. In any case, he continues: "*We shall begin with the simplest case, that of a single medium extending very far in all directions of space, and like all systems we shall here consider, being surrounded by a rigid cover impermeable to heat*" [3]. Finally, Planck makes the point relative to conduction: "*Now the condition of thermodynamic equilibrium requires that the temperature shall be everywhere the same and shall not vary with time. Therefore in any arbitrary time just as much radiant heat must be absorbed as is emitted in each volume-element of the medium. For the heat of the body depends only on the heat radiation, since on account of the uniformity of temperature, no conduction of heat takes place*" [3]. Remember, in this case, that Planck is dealing with a closed system. As such, once thermal equilibrium exists in such a system, there can be no net conduction.

Nonetheless, in open systems, an object can assume a fixed temperature, even if net conduction takes place. Such a situation can be devastating to the production of thermal photons as seen in section 2.4.2.

2.4.2 An example from the remote sensing of soil moisture

Soil moisture can be evaluated through emission profiles in the microwave region [27]. It is well known that the brightness temperature of soil drops dramatically with moisture content [27]. Given the presence of water, the soil can dissipate its heat through conduction, directly into the water, or through convection, as the liquid evaporates. In response, brightness temperatures drop [27]. When soil moisture is removed, brightness temperatures recover, for the simple reason that thermal emission now becomes the primary means of dissipating heat. Placing a body in direct contact with conductive or convective paths, allows heat to escape using non-radiative means, resulting in the lowering of brightness temperatures. In such a scenario, the brightness temperature recorded will be unrelated to the actual temperature of the object of interest. This is precisely what has been done in the case of the LFI reference targets on the Planck satellite [7,28].

2.5 Type-10 errors

In addition to all of the issues discussed so far, a Type-10 error can exist when standing waves are able to form inside the metal casing, enclosing the absorber (see Figure 3B). Thus, since the casing is made of metal, often possessing a backing along with small walls [7], it introduces the possibility of forming a pseudo-cavity in front of the horn wherein standing waves can build [4]. This leads to a Type-10 error. Such waves would trap energy into the target, making it unavailable to return-loss measurements. Nonetheless, absorption has not occurred. Standing waves simply confine the microwaves [4] and the return-loss measurements suggest an emissivity which is superior to that actually present.

As a result, a complete expression for the determination of absorptivity is as follows:

$$\kappa_{t_{\text{eff}}} = (\kappa_t + \Gamma_{\kappa\sigma}) = 1 - (\sigma_{an} + \Gamma_{\tau\sigma}) - (\sigma_{ad} + \Gamma_{s\sigma}) - \\ - (\Gamma_{bp} + \Gamma_{dh}) - (\Gamma_{dc} + \Gamma_{d\sigma}) - \Gamma_{\text{cond}} - \Gamma_{\text{conv}} - \Gamma_{sw} , \quad (6)$$

where Γ_{sw} accounts for the presence of standing waves. Once again, this term is important in addressing the reference targets on the Planck satellite [28].

3 Conclusions

Much can be gained by carefully considering all thermal components in a heat transfer problem. A complete analysis of error leads to the realization that progress must be made in the fabrication and testing of microwave reference loads and targets. At the same time, these considerations also impact the design of test facilities and anechoic chambers. Ideally, by lining room surfaces with temperature controlled metallic pyramids covered with Eccosorb, it should be possible to simultaneously create tremendous effective absorptivity by the walls and bring their effective emissivity down to very low levels. Such conditions would be ideal in many test scenarios involving anechoic chambers.

At the same time, the measurement of emissivity from microwave targets is a complex problem, wherein up to 10 or more, error types can be identified. Most of these errors are familiar to the geosciences and astrophysics communities. Some may have escaped analysis. Often though, calibration errors have been inappropriately dismissed as insignificant [7]. This is true for Type-10 errors, as the presence of standing waves in the metal casing is almost always ignored [7]. Nonetheless, a greater concern rests in the Type-7 errors which alter the effective radiative balance of the target due to geometrical arguments. Such errors can also be present in calibration blackbodies for use in the infrared [18, 19]. Targets are not enclosures [4] and are never blackbodies. Hence, they become subject to geometrical considerations. In addition, Type-8 errors can easily occur raising the possibility that conduction itself, by allowing heat to flow out of the target, is creating an imbalance between effective target emission and absorption. If heat can be funneled out of a target through conduction, its emissivity will fall. This can constitute an important limitation in building calibration targets.

As a result, though attempts have been made to quantify error sources in microwave calibration targets [13–15], it appears that many of the devices used as emissivity references on satellites and in the laboratory (e.g. [4–15] are inaccurate. They are simply unable to provide the emissivity believed to exist using return-loss measurements. This is a significant scientific oversight which affects the monitoring of global climate change (e.g. [8]) and the microwave background [5, 7]. Perhaps it is for this reason that geoscientists are now turning to Earth surfaces as potential calibration sources [29]. Nonetheless, this solution is not available to satellites such as Planck [7, 28] which must rely on their internal reference targets. The proper functioning of spacecraft internal reference targets can have the most profound consequences on scientific advancement, as will be discussed in the accompanying work [28].

Acknowledgements

The author would like to thank Luc and Christophe Robitaille for figure preparation and computer assistance, respectively.

Dedication

This work is dedicated to Barbara Anne Helgeson.

Submitted on February 15, 2010 / Accepted on February 19, 2010
Published online on February 22, 2010

References

1. Kirchhoff G. Über das Verhältnis zwischen dem Emissionsvermogen und dem Absorptionsvermögen der Körper für Wärme und Licht. *Poggendorfs Annalen der Physik und Chemie*, 1860, v. 109, 275–301 (English translation by F. Guthrie: Kirchhoff G. On the relation between the radiating and the absorbing powers of different bodies for light and heat. *Phil. Mag.*, 1860, ser. 4, v. 20, 1–21).
2. Planck M. Über das Gesetz der Energieverteilung im Normalspektrum. *Annalen der Physik*, 1901, v. 4, 553–563 (English translation by ter Haar D.: Planck M. On the theory of the energy distribution law in the normal spectrum. The old quantum theory. Pergamon Press, 1967, 82–90; also Planck's December 14, 1900 lecture "Zur Theorie des Gesetzes der Energieverteilung in Normalspectrum", which stems from this paper, can be found in either German, or English, in: Kangro H. Classic papers in physics: Planck's original papers in quantum physics. Taylor & Francis, London, 1972, 6–14 or 38–45).
3. Planck M. The theory of heat radiation. Philadelphia, PA., P. Blakiston's Son, 1914, 22–23.
4. Robitaille P.M. Kirchhoff's law of thermal emission: 150 Years. *Progr. Phys.*, 2009, v. 4, 3–13.
5. COBE website, http://lambda.gsfc.nasa.gov/product/cobe
6. Robitaille P.M. COBE: A radiological analysis. *Progr. Phys.*, 2009, v. 4, 17–42.
7. Valenziano L., Cuttaia F., De Rosa A., Terenzi L., Brighenti A., Cazzola G.P., Garbesi A., Mariotti S., Orsi G., Pagan L., Cavaliere F., Biggi M., Lapini R., Panagin E., Battaglia P., Butler R.C., Bersanelli M., D'Arcangelo O., Levin S., Mandolesi N., Mennella A., Morgante G., Morigi G., Sandri M., Simonetto A., Tomasi M., Villa F., Frailis M., Galeotta S., Gregorio A., Leonardi R., Lowe S.R., Maris M., Meinhold P., Mendes L., Stringhetti L., Zonca A. and Zacchei A. Planck-LFI: design and performance of the 4 Kelvin Reference Load Unit. *JINST*, 2009, v. 4, T12006.
8. Lambrigtsen B.H. Calibration of the AIRS microwave instruments. *IEEE Trans. Geosc. Rem. Sens.*, 2003, v. 41, 369–378.
9. Cox A.E. and Janezic M.D. Preliminary studies of electromagnetic properties of microwave absorbing materials used in calibration targets. *IGARSS*, 2006, 3467–3469.
10. Cox A.E., O'Connell J.J., and Rice J.P. Initial results from the infrared calibration and infrared imaging of a microwave calibration target. *IGARSS*, 2006, 3463–3465.
11. Randa J., Cox A.E, Francis M., Guerrieri J. and MacReynolds K. Standard radiometers and targets for microwave remote sensing. *IGARSS*, 2004, v. 1, 698.
12. Feng N. and Wei W. The optimization design for microwave wide band blackbody calibration targets. *International Conference on Microwave and Millimeter Wave Technology* (ICMMT), 2008, v. 4, 1695–1698.
13. Randa J., Walker D.K., Cox A.E., and Billinger R.L. Errors resulting from the reflectivity of calibration targets. *IEEE Trans. Geosc. Rem. Sens.*, 2005, v. 43, 50–58.
14. Li Z., Peng Y., Miao J., Wang Z. Evaluation of disturbance in the antenna calibration of the microwave radiometer. *International Conference on Microwave and Millimeter Wave Technology* (ICMMT), 2008, v. 4, 810–813.
15. Cheng C.Y., Li F., Yang Y.J. and Chen Y.M. Emissivity measurement study on wide aperture microwave radiometer. *International Conference on Microwave and Millimeter Wave Technology* (ICMMT), 2008, v. 4, 914–917.

16. Dietlein C., Popović Z., and Grossman E.N., Aqueous blackbody calibration source for millimeter-wave/terahertz metrology. *Appl. Opt.*, 2008, v. 47, 5604–5615.

17. Robitaille P.M. Blackbody radiation and the carbon particle. *Prog. Phys.*, 2008, v. 1, 36–55.

18. Fowler J.B. A third generation water bath based blackbody source. *J. Res. Nat. Inst. Stand. Technol.*, 1995, v. 100, 591–599.

19. Fowler J.B. An oil-bath-based 293 K to 473 K blackbody source. *J. Res. Natl. Inst. Stand. Technol.*, 1996, v. 101, 629–637.

20. Murphy A.V., Tsai B.K., Saunders R.D. Transfer calibration validation tests on a heat flux sensor in the 51 mm high temperature blackbody. *J. Res. Nat. Inst. Stand. Technol.*, 2001, v. 106, 823–831.

21. Emerson and Cuming Microwave Products. Technical Reference: ECCOSORB CR Two-Part Castable Load Absorber Series. http://www.eccosorb.com/file/958/cr.pdf

22. Stewart B. An account of some experiments on radiant heat, involving an extension of Prévost's theory of exchanges. *Trans. Royal Soc. Edinburgh*, 1858, v. 2(1), 1–20 (also found in Harper's Scientific Memoirs, edited by J. S. Ames: *The laws of radiation and absorption: memoirs of Prévost, Stewart, Kirchhoff, and Kirchhoff and Bunsen*, translated and edited by D. B. Brace, American Book Company, New York, 1901, 21–50).

23. Robitaille P.M. A critical analysis of universality and Kirchhoff's law: a return to Stewart's law of thermal emission. *Prog. in Phys.*, 2008, v. 3, 30–35; arXiv: 0805.1625.

24. Hoffmann D. On the experimental context of Planck's foundation of quantum theory. *Centaurus*, 2001, v. 43(3–4), 240–259.

25. Prévost P. Mémoire sur l'équilibre du feu. Journal de Physique, 1791, v. 38, 314–322 (translated in Harper's Scientific Memoirs (J. S. Ames, Ed.) — *The laws of radiation and absorption: memoirs of Prévost, Stewart, Kirchhoff, and Kirchhoff and Bunsen*, translated and edited by D. B. Brace, American Book Company, New York, 1901, 1–13).

26. Prévost P. Du calorique rayonnant. J. J. Paschoud, Geneva & Paris, 1809 (Sections are translated in Harper's Scientific Memoirs (J. S. Ames, Ed.) — *The laws of radiation and absorption: memoirs of Prévost, Stewart, Kirchhoff, and Kirchhoff and Bunsen*, translated and edited by D. B. Brace, American Book Company, New York, 1901, 15–20).

27. Ulaby F.T., Moore R.K., Fung A.K. Microwave remote sensing active and passive — Volume 2: Radar remote sensing and surface scattering and emission theory. London, Addison-Wesley Publishing Company, 1982, p.884–887.

28. Robitaille P.M. The Planck Satellite LFI and the microwave background: Importance of the 4 K references targets. *Prog. Phys.*, 2010, v. 2, 11–18.

29. Rüdiger C., Walker J.P., Allahmoradi M., Barrett D., Costelloe J., Gurney R., Hacker J., Kerr Y.H., Kim E., Le Marshall J., Lieff W., Marks A., Peisch S., Ryu D., and Ye N. Identification of spaceborne microwave radiometer calibration sites for satellite missions. *Proc. Intern. Congr. Modelling and Simulation* (MODSIM), Cairns, Australia, 2009, 3740–3746.

The Planck Satellite LFI and the Microwave Background: Importance of the 4 K Reference Targets

Pierre-Marie Robitaille

Department of Radiology, The Ohio State University, 395 W. 12th Ave, Suite 302, Columbus, Ohio 43210, USA
E-mail: robitaille.1@osu.edu

Armed with ∼4 K reference targets, the Planck satellite low frequency instrument (LFI) is intended to map the microwave anisotropies of the sky from the second Lagrange point, L2. Recently, the complete design and pre-flight testing of these ∼4 K targets has been published (Valenziano L. et al., JINST 4, 2009, T12006). The receiver chain of the LFI is based on a pseudo-correlation architecture. Consequently, the presence of a ∼3 K microwave background signal at L2 can be established, if the ∼4 K reference targets function as intended. Conversely, demonstration that the targets are unable to provide the desired emission implies that the ∼3 K signal cannot exist, at this location. Careful study reveals that only the second scenario can be valid. This analysis thereby provides firm evidence that the monopole of the microwave background, as initially detected by Penzias and Wilson, is being produced by the Earth itself.

1 Introduction

Over the years, I have expressed growing concern [1] about the origin of the microwave background [2]. My evaluation has focused on three fronts. First, I have highlighted that errors exist in the derivation of Kirchhoff's law of thermal emission (e.g. [3, 4] and references therein) which renders its use inappropriate in physics. The universality of blackbody radiation is invalid on both theoretical and experimental grounds [3, 4], making it impossible to assign an absolute temperature to the Penzias and Wilson [2] signal. At the same time, I have emphasized that the law of equivalence between emission and absorption, under conditions of thermal equilibrium, remains valid [4]. This is properly referred to as Stewart's law [5]. Second, I have questioned the assignment of the microwave background to the cosmos [6], invoking (see [1] and references therein), along with Borissova and Rabounski [7], that the Earth's oceans are responsible for this signal. It is the presence of the hydrogen bond within water which gives cause for reconsideration [8]. The emission of this bond has not yet been assigned for the Earth's spectrum, despite the reality that our planet is 70% water. Finally, I have outlined shortcomings in the measurements of the microwave background, especially relative to the COBE [9] and WMAP [10] satellites. Concern, relative to the results of these satellites, has also been voiced by a number of other groups [11–18]. Now, the Planck mission [19] is drawing the attention of the scientific community. But early reports [20] and system evaluations [21] should provoke uneasiness. This can only be appreciated when the function of the low frequency instrument (LFI) is understood [22–26]. It is through the analysis of the LFI's performance that the origin of the microwave background can be established [27].

On July 30, 2009 the ESA Planck team wrote: "*In the case of LFI, the results show even better than expected performances due to benign space environment and an improved tuning process*" [20]. On first consideration, it would seem that the monopole of the microwave background was present at L2, as expected by the astrophysics community. Unfortunately, upon careful review, this statement directly implies that the opposite situation has taken place. There can be no 3 K signal at this location. The arguments center on the functioning of the ∼4 K targets, whose full description only recently became available [21]. When the performance of these references is considered, in combination with the function of the pseudo-correlation receivers [22–26], solid evidence emerges that there can be no ∼3 K signal permeating space.

2 The performance of the Planck LFI

The proper characterization of the ∼4 K reference loads [21] and LFI [22–26] on the Planck satellite is critical to understanding whether the monopole of the 2.7 K microwave background is present at L2 [27]. This situation occurs, since the presence of a monopole cannot be ascertained with the high frequency instrument, HFI [28]. Relative to the HFI, the Planck team writes: "*Plank cannot measure accurately the monopole (uniform part of the emission) because many sources contribute (telescope, horns, filters,...)*" [29]. Thus, the HFI bolometers, though operating in absolute mode, can receive thermal photons from the spacecraft itself much of which is in a 50 K environment. As Planck's mirrors are exposed to 300 K at L2, photons of instrumental origin can enter the bolometers, making it difficult for the HFI to extract the ∼3 K background signal from instrumental foregrounds. It is anticipated that such effects are less important at the frequencies of the LFI. Consequently, it seems that only the LFI [22–26] can properly address the existence of a monopole at L2. The issue is critical since, in the absence of the monopole, any anisotropy measurements by this satellite would have little or no scientific value.

Expected performance of the PLANCK LFI receivers		
	Sky Temperature ~3 K	Sky Temperature ~0 K
Reference ~4 K	As expected	Poor
Reference ~0 K	Poor	Better than expected

Table 1: Summary of the scenarios which impact the expected performance of the pseudo-correlation receivers on the Planck satellite. Four possibilities exist depending on the actual brightness temperatures of the sky and the reference targets. It is assumed that the sky can be either at ~3 K (the Penzias and Wilson temperature [2]) or at ~0 K [1]. Similarly, the reference targets can be either operating as intended near 4 K [21], or are unable to generate a meaningful blackbody spectrum, ~0 K (as proposed herein).

As discussed in considerable detail [22–26], the low frequency instrument (LFI) functions as a pseudo-correlation receiver, wherein the sky signal is constantly being compared against a ~4 K reference signal. In this configuration, the receiver displays optimal performance only when the two input signals display approximately the same amplitude. Under these conditions, the input offsets are nearly identically zero, the knee frequency of the receiver is minimized and so is the $1/f$ noise [22–27]. The LFI team states, "*to minimize the 1/f noise of the radiometers, the reference blackbody temperature should be as close as possible to the sky temperatures (~3K)*" [21]. This represents an ideal situation, wherein the mechanical configurations of both receiver chains are identical. In practice, this cannot be achieved, as the reference horns are much smaller than the sky horns. Thus, a gain modulation factor is utilized to partially account for such effects [21–27]. In any case, the radiometric temperature difference between the signals captured by the sky and the reference horns constitutes a critical element in receiver performance. In order for the LFI to function properly, the sky signal must balance the reference signal.

There are four scenarios which need to be considered relative to the performance of the LFI receiver chains. These scenarios are summarized in Table 1 and are described as follows:

2.1 Sky at ~3 K, reference loads at ~4 K

The cosmology community is expecting a 2.7 K monopole signal at L2 [2]. In addition, some thermal photons might be expected from the galactic foreground and the spacecraft itself. As a result, the receiver would have optimal performance, if the sky signal was being compared with a reference signal at 2.7 K. However, the LFI group mentions that "*there is no convenient spacecraft source of 2.7 K with sufficient cooling power*" [21], and chose to passively cool the reference loads to ~4 K by mounting them on the 4 K thermal shield of the HFI. At first glance, this appears to be an elegant solution. But in actuality, as will be seen in section 3, this placement demonstrates suboptimal conditions relative to the principles of heat transfer. In any event, should the sky be at 2.7 K and the ~4 K load properly constructed, the receiver performance would be as expected from pre-flight modeling. Being approximately balanced, the sky and reference signals would generate a receiver performance matching the pre-flight technical specifications [22–26].

2.2 Sky at ~0 K, reference loads at ~4 K

Alternatively, if the monopole signal does not exist at L2 and *if the reference loads are truly acting as ~4 K blackbody sources*, a tremendous input offset would be generated in the receiver. The knee frequencies would rise, as would the $1/f$ noise. The result would be significant stripes in the maps generated by the satellite. These concerns were previously outlined in detail [27], *on the assumption that the ~4 K reference loads would be properly designed and able to provide the needed emission*.

2.3 Sky at ~3 K, reference loads acting as ~0 K sources

An interesting case can also manifest itself if the microwave sky is indeed at 2.7 K, but the reference loads, due to improper fabrication, do not produce an emission corresponding to a ~4 K blackbody source. In the extreme, the reference loads might be considered as producing no valuable emission signal. This would produce an emission from the loads indistinguishable from a ~0 K source, despite their ~4 K actual temperature. Under such a scenario, a tremendous imbalance would once again be produced in the receivers, the knee frequencies would rise, and $1/f$ noise would be manifested in the resultant maps.

2.4 Sky at ~0 K, reference loads acting as ~0 K sources

Finally, there is the possibility that the microwave sky is at ~0 K and that improperly manufactured reference loads produce a signal much inferior to the expected ~4 K source. Once again, in the extreme, the reference loads might be considered as producing no valuable emission signal, thereby behaving as ~0 K sources. Interestingly, in the case, the performance of the spacecraft would be better than expected. Only relatively small microwave emissions from the sky would be observed, and their lack of power would be complemented by the lack of power coming from the reference loads.

Of these four scenarios, only the first and last can be valid, given what we now know [20] about the performance of the LFI [22–26]. In fact, assuming that the ~4 K references were properly constructed, the performance of the LFI receivers,

by themselves, would prove that there is indeed a monopole signal at L2 [27]. Everything hinges on the quality of the ∼4 K reference blackbodies [21]. But given that "*even better than expected performances*" [20] were obtained, there is concern that the ∼4 K reference loads are not functioning as they should and that the last scenario (Sky at ∼0 K, reference loads ∼0 K) is the one which will prevail. Unfortunately, a detailed description of the ∼4 K loads was not available to the general public until December 29, 2009 [21]. The materials contained in this work provide enough information to resolve the question.

3 The ∼4 K Reference Loads on the PLANCK LFI

A schematic representation of a ∼4 K reference load system for the LFI is displayed in Figure 1. Each reference load system is comprised of a small horn, separated from a target by a 1.5 mm gap in order to preserve thermal isolation between the 20 K shield which houses the LFI and the ∼4 K shield housing the HFI [21]. The Planck team states: "*One of the main requirements of the 4KRL design was to minimize the heat load on the HFI to a value lower than 1 mW. Safety considerations (a thermal short between the two instruments will prevent the HFI to work) lead to mechanically decouple the loads, mounted on the HFI external shield, from the LFI radiometers, at 20 K*" [21]. They continue: "*This solution implies the presence of a gap in the radiometer reference arm, through which external spurious signals can leak in the radiometers*" [21]. They attempt to address this issue, by introducing grooves on the edge of the horn, in order to limit spillover. In addition, they state: "*Targets also need to be small and placed in the very near field of the reference horns to reduce the leak from the gap*" [21]. The LFI group notes that: "*the conceptual design is therefore based on small absorbing targets, mounted inside a metal enclosure ("case") to confine the radiation...*" [21].

The satellite team relays that: "*Each target is basically a rectangular Eccosorb™ CR block, shaped for optimal matching with the incoming field. The back part is made of highly absorbing CR117, while the front sector, made from CR 110, reduces the mismatch*" [21]. The absorbing material for each target is then enclosed on 5 sides, within an aluminum casing. These targets are mounted on the 4 K shield of the HFI using "*stainless steel (AISI304) thermal washers*" which are "*interposed between the loads and the interface points to the HFI*" [21]. The LFI group explains that: "*These are small cylinders (typically 5 mm long, 1 mm wall thickness) whose dimensions are optimized to dump temperature fluctuations in order to meet requirements*" [21]. Apparently, the ∼4 K reference loads are then attached directly through the washers onto the HFI 4 K shield with "*screws (mounted on the HFI)*" [21].

The designers opt to conduct heat out of the ∼4 K reference loads into the 4 K shield of the HFI in order to achieve a stable temperature. They enclose the Eccosorb material in an aluminum casing to help ensure that conductive paths are open which can suppress any thermal fluctuations within the loads. In so doing, they have introduced Type-8 errors into their system [30]. In fact, the LFI group, during the testing stage, observes that they must work to better suppress thermal fluctuations. Therefore, they attempt to increase thermal fluctuation damping. They write: "*the RF and thermal test results were used to further refine the design (i.e. thermal dumping was increased, mounting structure was slightly modified to facilitate integration)*" [21] and "*The optimization of the thermal washers allowed to increase the damping factor...*" [21]. Thus, they are trying to adopt a delicate balance between the necessity to cool the references on the 4 K shield and the need to efficiently address heat fluctuations: "*Cases, supported by an Al structure, are mounted on the HFI using Stainless Steel thermal decouplers (washers), which allows to carefully control the thermal behavior*" [21]. In reality, while the presence of the washers and their construction primarily impacts the time constants for damping heat fluctuations, they still provide a very efficient conductive heat path out of the targets. After all, the references remain cooled by conductive mechanisms which rely on thermal contact with the 4 K HFI shield. Herein is found the central design flaw of the Planck LFI.

3.1 Conductive paths and Type-8 errors

The Planck reference loads are cooled by conduction, not self-radiation. As a consequence, there is no reason to expect that the reference loads can output any photons at ∼4 K. Being cooled by conduction, the references do not need to invoke thermal radiation in achieving steady state. Indeed, the Planck team writes: "*Thermal interface is dominated by conduction through thermal washers*" [21]. They continue: "*Metal parts are assembled using Stainless Steel screws at high torque, to make thermal contact as close as possible to an ideal value*" [21]. Relative to thermal modeling they write: "*the 70 GHz loads are assumed to be perfect thermal conductors, due to their small thickness and mass*" [21]. Hence, the LFI group members, by introducing conduction directly into their loads, have rendered them ineffective as ∼4 K blackbody sources.

Certainly, in order for an object to act as a true blackbody, it must be devoid of all outgoing conductive paths of heat transfer. Reference targets must be spatially isolated from their surroundings, such that only radiation can dominate [30]. Yet, the ∼4 K targets on the Planck satellite are configured such that net conduction of heat out of the target is allowed to take place. The targets are mounted onto the 4 K shield of the HFI, and heat can flow continuously using conduction into that heat sink. Since the targets are continually exposed to a 20 K environment, their temperature is being ensured by conduction, not heat radiation. In this manner, thermodynamic steady state and a stable temperature is maintained, but through conduction, not heat radia-

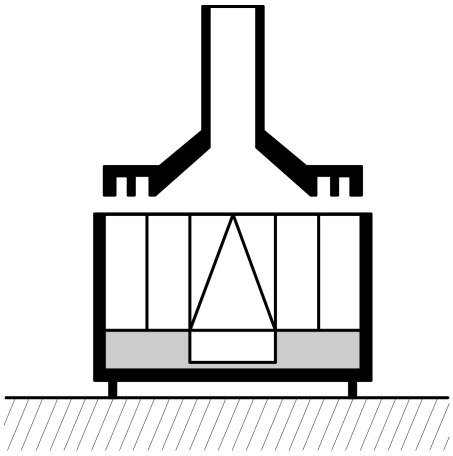

Fig. 1: Schematic representation of a Planck LFI reference load. Each load is comprised of a horn (upper section) and a target (middle section) separated by a 1.5 mm gap. The targets are constructed from molded Eccosorb (CR-110 or 117) absorber surrounded by an aluminum casing which acts to preserve thermodynamic steady state within each unit, using conduction. Heat is allowed to flow out of the target casing through a conductive path into the 4 K shield of the HFI (represented by the cross hatched area in the lower section). This path is provided by stainless steel cylindrical washers (see text and [21] for more detail). By providing a conductive path out of the target, the Planck LFI team has created a situation wherein a Type-8 error is introduced [30]. By itself, such a design ensures that these targets cannot operate as ∼4 K loads as intended (see text).

tion. The Planck LFI ∼4 K targets are directly linked, which good thermal contact, through stainless steel washers, onto a 4 K shield. Such a scenario will not only reduce the brightness temperature, relative to the real temperature, it is likely to completely inhibit the emission of photons [30]. In this respect, the presence of conductive paths in the Planck LFI ∼4 K targets provides a much worse scenario for achieving the expected brightness temperature, then when water permeates soil [30].

Rather than using conductive washers, stainless steel screws, and an aluminum casing, it would have been preferable to encase the Eccosorb in a strong insulator suspended in air with thin non-conducting support rods. Such a load could then be enclosed in a perfectly reflective shield at 4 K. It is only through this kind of geometry that a ∼4 K load can suitably act as a reference.

By itself, the Type-8 error indicates that no 3K signal exists at L2. The loads do not need to cool by radiation. Accordingly, they do not need to emit a single photon. They are unable to act as blackbodies in the intended capacity. Still, beyond the Type-8 error, there are sufficient concerns with the ∼4 K reference loads, that their lack of functionality can be established. In order to properly follow these issues, it is important to consider all of the potential errors related to measuring emissivity using return-loss methods on microwave targets [30].

3.2 Type-3, -4, -5, -6, and -7 errors

First, the ∼4 K reference loads are subject to a Type-3 error [30]. Radiation from the horn during testing can be diffracted on the edge of the target casing through the 1.5 mm thermal gap into the surroundings. This is because, unlike the horns, the casing contains no edge structure which can minimize diffraction. Secondly, the ∼4 K reference systems are subject to a Type-4 error, wherein incident radiation from the horn, experiences diffuse reflection on the surface of the Eccosorb, and is lost through the gap into space [30]. Similarly, Type-5 errors can occur. Incident radiation, in this case, enters the Eccosorb, is reflected on the casing, and then, after reentry into the absorber, becomes scattered into space through the gap. In the same way, a Type-6 error can occur [30]. That is, incident radiation which traverses the Eccosorb layer can be reflected by the casing, and on re-entry into the absorber, is diffracted upon striking the edge of the casing. Once more, such radiation could exit the system through the 1.5 mm thermal gap which separates the horn and the target (see Figure 1). In addition, Type-7 errors exist as previously discussed in detail [30]. These are errors which depend on the geometry of the target. They occur when a transmissive absorber is mounted on a reflective metallic casing and their characteristics have been addressed [30].

3.2.1 Planck test data, calculations, and Type-10 errors

There is also the possibility of a Type-10 error [30]. Namely, because the Planck team chose to use so little material in their casings, they have enclosed only weak absorbers. In so doing, they introduce the likelihood of generating standing waves within the casings during testing. This would represent a Type-10 error [30].

A careful study of Planck LFI return-loss traces provides strong evidence that such standing waves do exist. For instance, the Planck team presents Figure 26 [21], wherein the return-loss is measured. A single such tracing, obtained from a 30 GHz horn-target assembly, is extracted from this Figure to generate Figure 2 herein. Note that the network analyzer tracing has pronounced resonances extending as low as −50 dB at some frequencies. These resonances should not be present if the target is black [3]. In fact, the presence of such resonances, by itself, provides ample evidence that the 30 GHz targets are far from being black.

As a result, it is clear that the return-loss measurements published by the Planck team [21] far overstate the actual performance of the reference targets, if these values are directly utilized to calculate emissivity. In fact, this is evident by examining data provided by the Planck team. Consider, for instance, Figure 10 in [21] which is reproduced herein as Figure 3. This represents a computational analysis of field distributions that takes place both inside and around the targets, during testing with microwave radiation. It is evident, from this figure, that the targets are unable to localize microwave

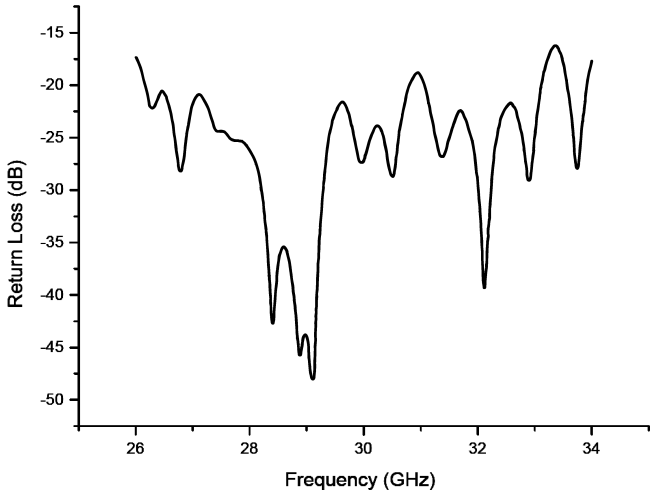

Fig. 2: Schematic representation of a network analyzer tracing for a 30 GHz reference target system, as provided by the Planck LFI team [21]. This particular tracing was extracted from Figure 26 in [21] in order to better visualize its features. Note the presence of significant resonances on this tracing, indicating the existence of standing waves within the horn-target system. It is well known, based on elementary considerations in electromagnetics [3], that cavities, waveguides, and enclosures, at microwave frequencies, can sustain standing waves in a manner depending on their size and geometry (see [3] and references therein). This problem is particularly important when the dimensions of the target approach the wavelengths of interest. In this case, 30 GHz corresponds to a wavelength of ∼1 cm in vacuum. The target casings are $3.3 \times 3.3 \times (\sim 2)$ cm (see Table 1 and Figure 12 in [21]). The presence of such resonances in the ∼4 K reference loads, demonstrates unambiguously that the targets are not black. In fact, the targets are still acting as resonant devices [3]. For a blackbody to exist, all such resonances must be suppressed (i.e. as ideally seen by a constant −50 dB tracing across the spectral range). In this case however, and when combined with the data in Figure 3, it appears that approximately −15 to −20 dB of return loss can be accounted for by leakage from the 1.5 mm gap. Then, between −20 to −25 dB of return loss can be attributed, at certain frequencies, to the existence of resonance features. Note that 29 GHz gives a wavelength of ∼1.03 cm in vacuum, and perhaps a little more in Eccosorb (see [30] and references therein). As such, the resonances at 28.5–29.2 GHz correspond almost exactly to 3 wavelengths in a square 3.3 cm enclosure. Reproduced from [21] with permission of the IOP and L.Valenziano on behalf of the authors and the Planck LFI consortium.

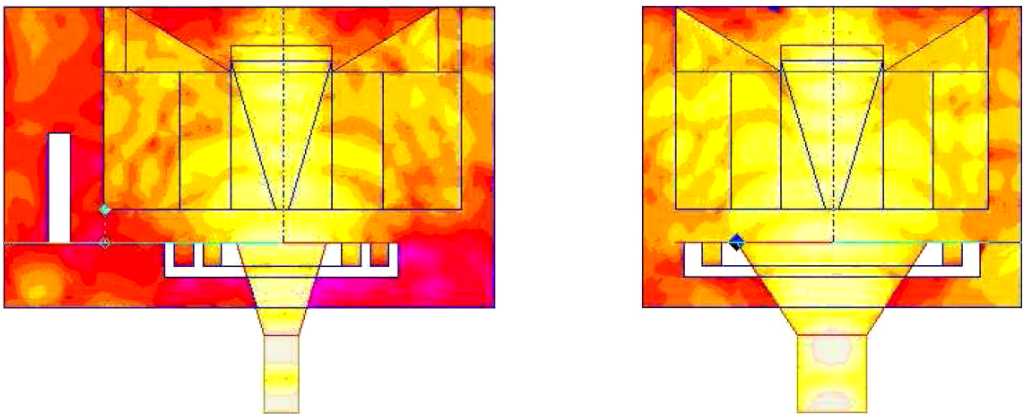

Fig. 3: Computational determination of the E-field distribution at 70 GHz for a horn-target assembly as reproduced from Figure 10 in [21]. White areas represent perfect conductors, whereas regions of increased brightness depict more intense fields [21]. The left panel corresponds to PHI = 90 while the right panel to PHI = 0. Further details are available in [21]. Note how the target is unable to localize microwave energy. Leakage of radiation beyond the 1.5 mm gap separating the horn and the target is evident, especially in the right panel. If leakage appears to be less intense in the left panel (examine the left edge of the casing), it is because the horn dimension in this cut is substantially smaller than the target. Nonetheless, some restriction of radiation is visible on the left edge of the casing in the left panel. This acts to confirm that none of the other edges are able to confine the radiation. Note also that the section of CR-117 absorber below the pyramid is actually acting to reflect rather than absorb the radiation. This is especially evident in the left panel (note red area beneath the central pyramid (see [21] for more detail). From these calculations, it is apparent that the Planck LFI targets at 70 GHz are not black, enabling dissipation of energy well beyond the horn-target assembly. Unfortunately, the Planck team does not display corresponding results at 30 and 44 GHz. Reproduced from [21] with permission of the IOP and L.Valenziano on behalf of the authors and the Planck LFI consortium.

energy within the casing. In fact, especially in the PHI = 0 cut (see Figure 3, right side), microwave power is flowing freely throughout the space in front and around the target. No localization of energy is evident. This provides solid evidence that the return-loss measurements far overstate the performance of these devices when attempting to evaluate emissivity.

4 Discussion

Consequently, the Planck LFI group has not properly measured the emission of their reference loads. "*Indeed, Valenziano et al. [21] do not even provide the estimated emissivity of their targets. By itself, this constitutes an implicit indication that these values cannot be properly determined, with such methods, as I previously stated*" [9].

Faced with Type-3, -4, -5, -6, -7 and -10 errors, the target is unable to absorb the microwave energy from the horn and the latter is able to leak out of the gap into the surrounding space. This occurs even though the horn has edge structure to prevent leakage into the gap as such a configuration neglects the chaotic propagation of microwave energy which can occur within the target. Nonetheless, the Planck team assumes that, in making their return-loss measurements, no leakage into the gap takes place, even though such phenomena is evident in their own calculations (see Figure 3). They further assume that their casing cannot support any standing waves (see Figure 2).

As such, relative to the Planck satellite LFI, the published return-loss values, do not properly represent the emissive power of their reference targets. The latter is much less than expected, both due to gap leaks, as mentioned above, and because return-loss methods overestimate the true emission in the presence of metal casings (Type-7 errors). The presence of the aluminum casings provides ample opportunities to set up standing waves in front of the horn (Type-10 errors). Such waves are present in the traces displayed by the Planck team (see Figure 2 herein and Figure 26 in [21]). This further illustrates that these reference blackbodies are not black. Ultimately, the most serious concern is the presence of a Type-8 error [30]. Conduction has been allowed as the key means of establishing thermodynamic steady state. Subsequently, it can be said that reference blackbodies do not even exist on the Planck satellite.

Given this information, the members of the scientific community, independent of the Planck team, can now either confirm or refute the existence of a monopole at L2. They may do so by concurring with this analysis and establishing the emissivity of the ∼4 K reference loads on the LFI. If the loads truly act as ∼4 K references, then the monopole signal must be present at L2. Conversely, as suggested by this work, if the ∼4 K references are unable to emit properly as ∼4 K blackbodies, then the excellent performance of the LFI implies that there is no monopole at L2 and that this signal does indeed arise from the Earth itself [1].

Unfortunately, it is rather difficult to establish the extent to which a reference target is black in the microwave. However, the following approaches might be considered. At the onset, the measurements must not occur inside an anechoic chamber. Such chambers suppress leaked signals and thereby overstate the emissivity of the target obtained with return-loss measurements. Therefore, such a setting should be avoided. Relative to a small target, like those on the Planck satellite [21], it might be possible to ascertain that they are very poor emitters in the following way. First, a duplicate horn must be placed inside a perfectly reflecting enclosure. The return-loss perfomance in such a case will be poor. This is because virtually all the energy emitted by the horn becomes trapped by the enclosure. This energy would then be able to return to the network analyzer, provided that it is not involved in the formation of standing waves either in the enclosure or within the horn [3].

Once this has been accomplished, the experiment must be repeated, but this time, the target must be placed in front of the horn with a 1.5 mm spacing, as noted by the Planck team. The entire assembly must be once again positioned inside a perfectly reflecting enclosure, wherein the horn and target geometry are preserved. A single drive mechanism must enter the enclosure. As for the target, two cases should be considered: one where a conductive path to the enclosure exists and one where it is suppressed. Once again, the network analyzer would be connected. But this time, any power incident on the target which is not absorbed will be reflected by the walls. Indeed, standing waves will be set up inside either the aluminum casing itself, or the enclosure [3], both of which are acting now as microwave cavities. These standing waves will create oscillations on the network analyzer tracing. By constructing a box whose dimensions can be gradually modified, it should be possible to alter the pattern of standing waves in the cavity. A target will be considered black only when all modifications of the enclosure dimensions, or that of the casings, can yield no changes on the return-loss signal proving that no standing waves exist. Ideally, in this case, the return-loss tracing will display a constant value across the spectral range with no trace of resonance. This can solely occur if all radiation, incident on the target, is absorbed. In this fashion, the blackness of a radiator can be established. Interestingly, this test, so critical to the proper scientific evaluation of the Planck mission, is readily accessible, and at low cost, by most of the electromagnetic laboratories of the world.

However, given our current knowledge of the LFI reference loads [21–27], it is already evident that the Planck targets within this test setting will display strong resonances. Indeed, from the analysis provided above, the references cannot be operating as blackbodies relative to the frequencies of interest. The Planck team has permitted conduction in their system. As a result, the reference targets are envisioned to have constant uniformity of temperature. In fact, this is assured by dumping heat through conduction into the 4 K shield

at all times during flight, in violation of Planck's requirement that conduction not transpire. Max Planck writes: "*For the heat of the body depends only on heat radiation, since, on account of the uniformity in temperature, no conduction of heat takes place*" [31]. To complicate matters, the Planck team ignores the reality that good conductors make poor emitters (see [3] and references therein). This fact has been known for more than 100 years. Yet, the LFI consortium unknowingly has created a situation where they believe that their reference loads can be treated as perfect conductors. They write that: "*the 70 GHz loads are assumed to be perfect thermal conductors, due to their small thickness and mass*" [21]. They have created these "perfect conductors" by enclosing a small amount of absorber within a metallic enclosure. This issue is discussed in greater detail in [30], but nonetheless, the design of the Planck LFI reference targets reflects a sidestep of elementary thermodynamic principles.

In closing, for nearly 50 years, the microwave signal first detected by Penzias and Wilson [2], has fascinated scientists. Yet, all too quickly, its cosmological nature was embraced [6]. In fact, the publication of the interpretation [6] preceded the discovery itself [2]. Now, with the aid of the Planck satellite, the electromagnetics laboratories of the world should be able to confirm or refute the existence of a ∼3 K cosmic signal. The key to this puzzle rests in the understanding of the LFI and reference targets [21–27]. Soon, scientists should reach the definitive answer. In the end, in this age of concern for the global climate, mankind cannot long afford to maintain that a signal of Earthly origin [1] is, in fact, cosmic [6]. Enough evidence is already beginning to build [1, 3, 4, 7–18] indicating that physics, astrophysics, and geophysics stand on the verge of a significant reformulation. In any event, the definitive proof that the monopole of microwave background belongs to the Earth has now been provided.

Acknowledgements

The author would like to thank Luc and Christophe Robitaille for figure preparation and computer assistance, respectively.

Dedication

This work is dedicated to Thomas Kerner Helgeson.

Submitted on February 15, 2010 / Accepted on February 19, 2010
Published online on February 22, 2010

References

1. Robitaille P.-M. A radically different point of view on the CMB. In: *Questions of Modern Cosmology — Galileo's Legacy*, ed. by M. D'Onofrio and C. Burigana, Springer, New York, N.Y., 2009.
2. Penzias A.A. and Wilson R.W. A measurement of excess antenna temperature at 4080 Mc/s. *Astrophys. J.*, 1965, v. 1, 419–421.
3. Robitaille P.M. Kirchhoff's law of thermal emission: 150 years. *Progr. Phys.*, 2009, v. 4, 3–13.
4. Robitaille P.M. A critical analysis of universality and Kirchhoff's law: a return to Stewart's law of thermal emission. *Prog. Phys.*, 2008, v. 3, 30–35; arXiv: 0805.1625.
5. Stewart B. An account of some experiments on radiant heat, involving an extension of Prévost's theory of exchanges. *Trans. Royal Soc. Edinburgh*, 1858, v. 22(1), 1–20 (also found in Harper's Scientific Memoirs, edited by J. S. Ames: *The laws of radiation and absorption: memoirs of Prévost, Stewart, Kirchhoff, and Kirchhoff and Bunsen*, translated and edited by D. B. Brace, American Book Company, New York, 1901, 21–50).
6. Dicke R.H., Peebles P.J.E., Roll P.G., and Wilkinson D.T. Cosmic black-body radiation. *Astrophys. J.*, 1965, v. 1, 414–419.
7. Borissova L. and Rabounski D. PLANCK, the satellite: a new experimental test of General Relativity. *Progr. Phys.*, 2008, v. 2, 3–14.
8. Robitaille P.M. Water, hydrogen bonding, and the microwave background. *Progr. Phys.*, 2009, v. 2, L5–L8.
9. Robitaille P.M. COBE: A radiological analysis. *Progr. Phys.*, 2009, v. 4, 17–42.
10. Robitaille P.M. WMAP: A radiological analysis. *Progr. Phys.*, 2007, v. 1, 3–18.
11. García-García A. Finite-size corrections to the blackbody radiation laws. *Phys. Rev. A*, 2008, v. 78(2), 023806.
12. Verschuur G.L. High Galactic latitude interstellar neutral hydrogen structure and associated (WMAP) high-frequency continuum emission. *Astrophys. J.*, 2009, v. 671, 447–457.
13. Cover K.S. Sky maps without anisotropies in the cosmic microwave background are a better fit to WMAP's uncalibrated time-ordered data than the official sky maps. *Europhys. Lett.*, 2009, v. 87, 69003.
14. Copi C.J., Huterer D., Schwarz D.J. and Starkman G.D. On the large-angle anomalies of the microwave sky. *Mon. Not. R. Astron. Soc.*, 2006, v. 367, 79–102.
15. Schwarz D.J., Starkman G.D., Huterer D. and Copi C.J. Is the low-ℓ microwave background cosmic? *Phys. Rev. Lett.*, 2004, v. 93, 221301.
16. Lieu R., Mittaz J.P.D. and Zhang S.N. The Sunyaev-Zel'dovich effect in a sample of 31 clusters: a comparison between the X-ray predicted and WMAP observed Cosmic Microwave Background temperature decrement. *Astrophys. J.*, 2006, v. 648, 176–199.
17. Jiang B.Z., Lieu R., Zhang S.N. and Wakker B. Significant foreground unrelated non-acoustic anisotropy on the 1 degree scale in Wilkinson Microwave Anisotropy Probe 5-year observations. *Astrophys. J.*, 2010, v. 708, 375–380.
18. Sawangwit U. and Shanks T. Beam profile sensitivity of the WMAP CMB power spectrum. 2009, arXiv:0912.0524.
19. Planck website: http://www.rssd.esa.int/index.php?project=Planck
20. http://twitter.com/Planck/status/2936389049
21. Valenziano L., Cuttaia F., De Rosa A., Terenzi L., Brighenti A., Cazzola G.P., Garbesi A., Mariotti S., Orsi G., Pagan L., Cavaliere F., Biggi M., Lapini R., Panagin E., Battaglia P., Butler R.C., Bersanelli M., D'Arcangelo O., Levin S., Mandolesi N., Mennella A., Morgante G., Morigi G., Sandri M., Simonetto A., Tomasi M., Villa F., Frailis M., Galeotta S., Gregorio A., Leonardi R., Lowe S.R., Maris M., Meinhold P., Mendes L., Stringhetti L., Zonca A. and Zacchei A. Planck-LFI: design and performance of the 4 Kelvin Reference Load Unit. *JINST*, 2009, v. 4, T12006.
22. Cuttaia F., A. Mennella A., Stringhetti L., Maris M., Terenzi L., Tomasi M., Villa F., Bersanelli M., Butler R.C., Cappellini B., Cuevas L.P., D'Arcangelo O., Davis R., Frailis M., Franceschet C., Franceschi E., Gregorio A., Hoyland R., Leonardi R., Lowe S., Mandolesi N., Meinhold P., Mendes L., Roddis N., Sandri M., Valenziano L., Wilkinson A., Zacchei A., Zonca A., Battaglia P., De Nardo S., Grassi S., Lapolla M., Leutenegger P., Miccolis M. and Silvestri R.. Planck-LFI radiometers tuning. *JINST*, 2009, v. 4, T12013.
23. Maino D., Burigana C., Maltoni M., Wandelt D.B., Gorski K.M., Malaspina M., Bersanelli M., Mandolesi N., Banday, A.J., and Hivon E. The Planck-LFI instrument: analysis of the $1/f$ noise and implications for the scanning strategy. *Astrophys. J. Suppl. Series*, 1999, v. 140, 383–391.

24. Sieffert M., Mennella A., Burigana C., Mandolesi N. Bersanelli M., Meinhold P., and Lubin P. $1/f$ noise and other systematic effects in the PLANCK-LFI radiometers. *Astron. Astrophys.*, 2002, v. 391, 1185–1197.

25. Bersanelli M., Aja B., Artal E., Balasini M., Baldan G., Battaglia P., Bernardino T., Bhandari P., Blackhurst E., Boschini L., Bowman R., Burigana C., Butler R.C., Cappellini B., Cavaliere F., Colombo F., Cuttaia F., Davis R., Dupac X., Edgeley J., D'Arcangelo O., De La Fuente L., De Rosa A., Ferrari F., Figini L., Fogliani S., Franceschet C., Franceschi E., Jukkala P., Gaier T., Galtress A., Garavaglia S., Guzzi P., Herreros J.M., Hoyland R., Huges N., Kettle D., Kilpelä V.H., Laaninen M., Lapolla P.M., Lawrence C.R., Lawson D., Leonardi F., Leutenegger P., Levin S., Lilje P.B., Lubin P.M., Maino D., Malaspina M., Mandolesi M., Mari G., Maris M., Martinez-Gonzalez E., Mediavilla A., Meinhold P., Mennella A., Miccolis M., Morgante G., NashA., Nesti R., Pagan L., Paine C., Pascual J.P., Pasian F., Pecora M., Pezzati S., Pospieszalski M., Platania P., Prina M., Rebolo R., Roddis N., Sabatini N., Sandri M., Salmon M.J., Seiffert M., Silvestri R., Simonetto A., Smoot G.F., Sozzi C., Stringhetti L., Terenzi L., Tomasi M., Tuovinen J., Valenziano L., Varis J., Villa F.,Wade L., Wilkinson A., Winder F., and Zacchei A. PLANCK-LFI: instrument design and ground calibration strategy. *Proc. Eur. Microwave Assoc.*, 2005, v. 1, 189–195.

26. Mennella A., Bersanelli M., Seiffert M., Kettle D., Roddis N., Wilkinson A., and Meinhold P. O set balancing in pseudocorrelation radiometers for CMB measurements. *Astro. Astrophys.*, 2003, v. 410, 1089–1100.

27. Robitaille P.M., On the Nature of the Microwave Background at the Lagrange 2 Point. Part I. *Progr. Phys.*, 2007, v. 4, 74-83.

28. Lamarre J.M., Puget J.L., Bouchet F., Ade P.A.R., Benoit A., Bernard J.P., Bock J., De Bernardis P., Charra J., Couchot F., Delabrouille J., Efstathiou G., Giard M., Guyot G., Lange A., Maffei B., Murphy A., Pajot F., Piat M., Ristorcelli I., Santos D., Sudiwala R., Sygnet J.F., Torre J.P., Yurchenko V., Yvon D., The Planck High Frequency Instrument, a third generation CMB experiment, and a full sky submillimeter survey. *New Astronomy Rev.*, 2003, v. 47, 1017–1024.

29. http://herschel.esac.esa.int/Hcal/documents/Lamarre.pdf (accessed January 24th, 2010).

30. Robitaille P.M. Calibration of microwave reference blackbodies and targets for use in satellite observations: An analysis of errors in theoretical outlooks and testing procedures. *Prog. Phys.*, 2010, v. 3, 3–10.

31. Planck M. The theory of heat radiation. Philadelphia, PA., P. Blakiston's Son, 1914, 23.

A Numerical Experiment with the Double Slit Geometry

Riadh H. Al Rabeh
Department of Mechanical Engineering, University of Basra, Iraq
Present address: Lydgate Close, Manningtree, Essex, UK
E-mail: alrabeh_rh@yahoo.com

Young's double slit experiment performed in 1801 was a milestone in the history of physics. The passing of light through two narrow slits creates interference patterns that sums up the diffraction patterns from each slit when separately uncovered. The experiment was later repeated by others using single photons, single electrons, atoms and even molecules producing similar effects. The present interpretation of the results is that photons and all other particles behave like waves and particles at the same time (the wave-particle duality principle). Further explanations were also given, including notions like particles can exist in more than one position at the same time and interfere with itself, and that the classical laws of physics are not applicable in an atomic scale. In this work we perform a numerical experiment in which a single charged particle is fired at a wall of (fixed) charged particles containing gaps to mimic slits, and collect the results over many events in time. Assuming only a classical inverse square relation to hold between the particles- including those of the wall, the results show clear diffraction and interference patterns indicating that the wave behaviour of the bullet particles arises simply from such interactions- hence providing a pure classical interpretation to the problem. That is; particles follow classical laws and produce waves only when interacting with each others. An analytical treatment of this subject is further required to remove the effects of a finite time step inherent in a numerical solution.

1 Introduction

The double slit experiment is considered an important milestone in the history of physics. It was first conducted by Thomas Young in 1801. In Young's experiment, light was made to pass through two narrow slits in an opaque barrier (wall) and collect on a photographic plate behind the barrier. The picture obtained with any one slit open, was that of diffraction in the form of one bright line in the middle of fading alternating dark and bright lines. When two slits are open, the picture changes into an interference pattern that can be explained by the addition of two diffraction patterns from the two slits separately. The double slit experiment was originally performed to settle the argument at the time of whether light- seen to travel along straight lines and reflect like being composed of particles (or corpuscles), and as suggested by Newton, or as waves like Huygens was advocating in his new theory for waves. The interference obtained were taken to favour the wave theory- since the effects of having particles should be producing only positive additions and no annihilation- as the slit experiment seemed to be suggesting [1].

As evidence from experiments in different fields and theoretical work started to accumulate in favour of the particle nature of light, there was a return to the slit experiment to be conducted this time using particles like electrons, neutrons, atoms and molecules [2, 3]. This is to establish if all particles do exhibit a wave-like behaviour as that of the photon particle. The results were again all positive prompting a new explanation to the results, namely that: particles have a dual particle-wave nature. Further tests were subsequently conducted using single photons, electrons and other particles fired one at a time. The interference pattern persisted in all these cases as well- prompting the conclusion that atomic scale particles do not obey the laws of classical mechanics [3–5]. In all these explanations however, the interaction between the barrier particles and those of the bullets are only taken to be of the go no-go relation with no regard to the possibility of some inverse square type forces being involved. Random scatter at the edges of the slits might have also been considered but thought not being capable of producing such consistent wave behaviour. The main thinking instead was concentrated on the interference pattern as being the result of an interaction between the bullet particles alone.

In this article we shall assume that the barrier particles do interact with the bullet particles through a simple inverse square relation. To do this we shoot a charged bullet particle at a wall composed of fixed and similarly or oppositely charged particles (with gaps to mimic the presence of slits). The path of the bullet particle is to be predicted by numerically integrating the equation of motion for a single path at a time and collect the paths over time. An interaction between the barrier particles and the bullet is a must of course, since otherwise there is no meaning to the word slit at all. The type of interaction however, is what is new in the present work. The results seem to show that an inverse square interaction is capable of producing the wave behaviour required to explain the results using pure classical laws and interpretations. A major drawback of the present numerical solution however, is that it is discrete and hence can be affected by the size of the time step. Further analytical treatment of the subject (in the

light of the present results) will be needed before a concrete conclusion can be made on this matter. Such work is not expected to contradict the vivid wave and interference patterns observed in the numerical results.

To be able to cover two slits and to produce different wave patterns, the axial velocity of the bullet was changed in a systemic manner in the experiment and the vertical (transverse) component of the bullet velocity was changed randomly by a very small amount around zero. This allows the accumulating beam to cover both slits over time.

2 Theory

For Coulomb forces, the expression for the acceleration is given by;

$$a = \frac{d^2r}{dt^2} = \frac{k}{r^2}\,, \tag{1}$$

where $a = a(t)$, $r = r(t)$ are the acceleration and separation distances between any isolated pair of particles as a function of time t, and k is the coupling constant (negative for attractive, and positive for repulsive forces) and in which the masses and charges of all particles are unity. The magnitude of k is dependent on the type of interaction. For example, in the case of a repulsive Coulomb forces $k = 1/4\pi\varepsilon_0$, where ε_0 is the permittivity of empty space. In the case the number of interacting particles is small; the Coulomb forces by far dominate other forces as assumed here. As the interacting masses are points, there is no need to consider angular velocity, spin, angular momentum or any form of moments of forces on the particle. For a group of interacting particles, the net acceleration of particle j is given by;

$$\mathbf{a}_j = \frac{d\mathbf{v}_j}{dt} = \sum_i \frac{k_{ij}\mathbf{r}_{ij}}{r_{ij}^3}\,;\;\; r_{ij} = |\mathbf{r}_{ij}|,\;\; i, j = 1, 2, \cdots N\,, \tag{2}$$

where $\mathbf{a}_j$ is the resultant acceleration, $\mathbf{v}$ is velocity, k_{ij} is the total coupling constant between particles i and j, and $\mathbf{r}_{ij} = \mathbf{r}_j - \mathbf{r}_i$ is the vector from i to j positions and N is the total number of particles. Equation (2) is a set of simultaneous ode's that must be integrated once in order to find $\mathbf{v}_j(t)$ and again to find the position $\mathbf{r}_j(t)$ giving;

$$\mathbf{r}_j = \mathbf{r}_{j0} + (dt)\mathbf{v}_{j0} + (dt)^2 \sum_i \frac{\mathbf{r}_j - \mathbf{r}_i}{|\mathbf{r}_j - \mathbf{r}_i|^3}\,;\;\; j = 1 : N;\;\; i \neq j. \tag{3}$$

If we know the initial position $\mathbf{r}_{j0}$, the initial velocity $\mathbf{v}_{j0}$, and the time step dt, we can find the new position of the bullet $\mathbf{r}_j$. This is to be repeated for different initial velocities and the resulting trajectories are collected over time and plotted. The values chosen for the various parameters do not necessarily correspond to particular physical values, but rather chosen to accentuate the resulting picture and make it clearer. The actual values used are given. A simple one step method is chosen for the integration as in equation (3) to avoid any erroneous contributions from any extra terms contained in a more refined integration procedure.

If we hope to produce results showing a wave behaviour using only inverse square relations, we should be able to show that this is possible in theory. In fact [6] states that the potential equation of motion becomes a spring like relation in the case of small displacements together with a large number of interacting particles. In the present case, we assume the wall particles are fixed in space, which is equivalent to a presence of a large number of particles in a small space making the group massive and well connected to resist the effects of the bullet particle approaching the barrier. We further confirm this in Fig. 1, where a spring type relation results from fixing two particles and allowing a third to experience a small displacement in the middle under an inverse square force. The algorithm needed to implement equation (3) is fairly straight forward as shown below;

```
Algorithm to compute the trajectory of a charged
particle fired at a wall containing slits and composed
of similarly (or oppositely) charged fixed particles.
Total number of particles nb=10 at position r(x,y),
velocity (vx,vy), acc.  (ax,ay)
and force (fx,fy)=acc.
For a fixed wall, x,y are calculated only
for the 1st particle.

ee=1e-100;X=[];Y=[];dt0=.01; v01=3.2; nb=12;
nbv=1:nb;x(nbv)=0;x=x';y=x;vx=x;
vy=x;kb(1:nb)=2e-3;kb(5:9)=0;
for ii=1:250;
y(1)=0; vy(1)=0.08*(rand-0.5); x(1)=-1;
vx(1)=v01;x(2:nb)=-0.25;
y(2:end)=0.002*((2:nb)-nb/2 -1);
for kk=1:100; for jj=1:nb; xj=x(jj); yj=y(jj);
vxj=vx(jj);vyj=vy(jj); xb=xj-x;yb=yj-y;
rb2=ee+xb.^ 2+yb.^ 2; rb=sqrt(rb2);
fb=kb'./rb2; fxb=fb.*xb./rb; fyb=fb.*yb./rb;
fx=sum(fxb);fy=sum(fyb);
ax=fx;ay=fy; dt=dt0;
if jj > 1;dt=0;end;
vxj=vxj+dt*ax; vyj=vyj+dt*ay; xj=xj+dt*vxj;
yj=yj+dt*vyj;x(jj)=xj; y(jj)=yj;
vx(jj)=vxj; vy(jj)=vyj;
end;
if abs(x(1)) > 1.5 | abs(y(1)) > 1;break;end;
X=[ X;x'];Y=[Y;y'];end;end;
figure(1);plot(X,Y);
```

The inner loop jj adds the forces over all the particles, then we advance in time in the kk loop to give one path (trajectory). The ii loop repeats this many times to arrive at the final picture. The rest of the algorithm is self explanatory.

3 Results

The values of the coupling constant k, (units m^3/s^2 as in (1)), the horizontal and vertical velocity components, the distances between slits and between the particles making the wall, the time step and other constants are clearly referenced in the al-

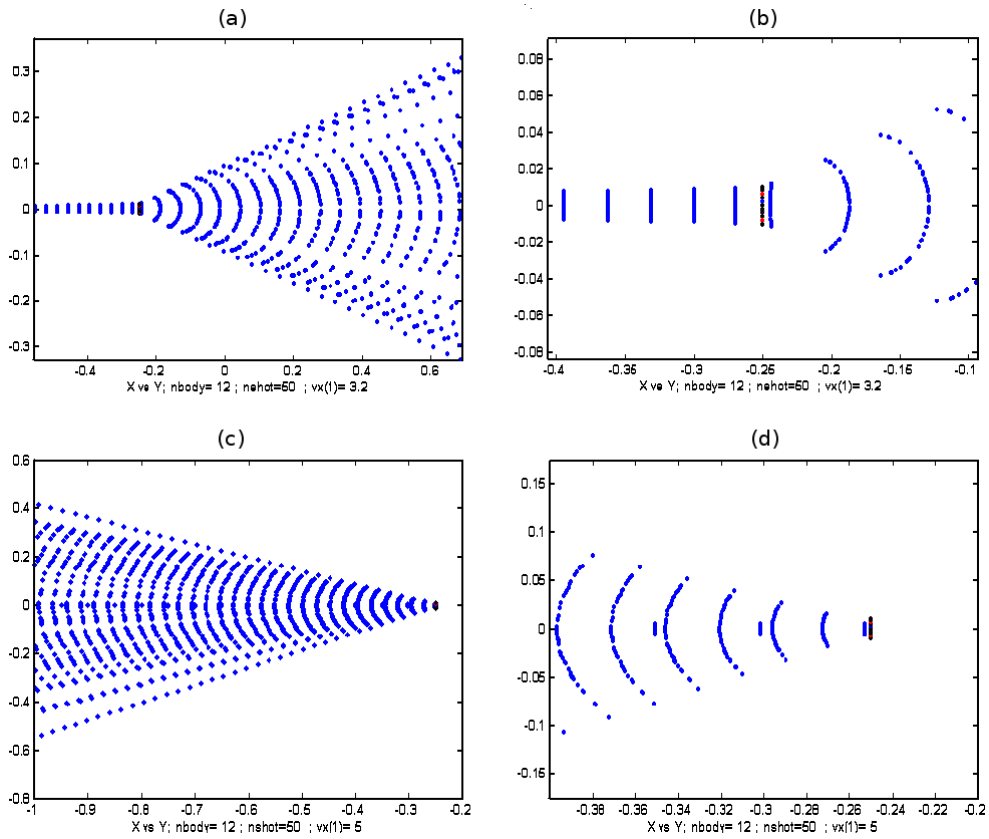

Fig. 2: Time collection of an electron fired (from left) against a fixed column barrier of loose electrons with a random small vel. component in the vertical direction. Total of 50 events are collected. Wave–front plane in (a), (b) changing to circular after the barrier. At another speed, the wave-front is completely reflected (b), (c) and also changed to circular.

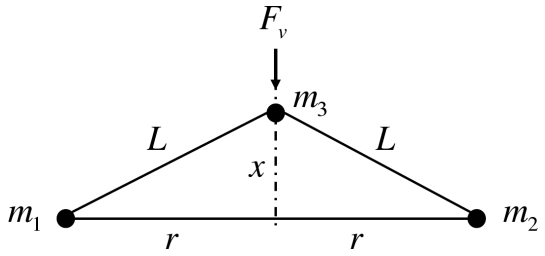

Fig. 1: A spring like force relation capable of producing a wave behavior can result from the interaction of particles under an inverse square relation. $F_{31} = F_{32} = k/r^2$; for small deflection x; $L = r$. $F_v = 2\frac{k}{r^2}\frac{x}{r} = 2\frac{k}{r^3}x = Kx$; k, r, K are constants. Therefore, force on m_3 is a spring type force.

gorithm given above. It is again stressed that the different constants are chosen so as to produce a clear picture rather than correspond to certain physical values. The main goal of this article is to show the wave phenomenon of diffraction and interference happening in a purely inverse square environment and with bullet particles that do not know of each other and hence never have a chance to interact as they exist in different times.

Fig. 2(a) shows a plot collecting 50 events and showing that what was originally a plane wave-front (elements of the front exist at different times) have been changed by the barrier to a circular wave-front as one would expect of a true wave. A magnified scale of the same is shown in the next figure. In Figs. 2(c),(d) the wave front is reflected completely as what could happen with real waves when the wavelength compared to the sparseness of the particle of the wall is of the correct order. In Fig. 3(a) few of the wall particles are assumed to be inert to mimic the presence of a slits. The result as expected is a superposition of two circular waves producing an interference pattern. It is seen that a single bullet collected over time is behaving like a true beam composed of many particles. The presence of the one barrier in all the shooting events is what unifies all the outputs and creates the observed effects.

4 Conclusions

The results shown indicate clearly that the passage of a bullet particle through a slit modifies its path and the wave-front composed of many particles, which need not exist at the same time, can change from plane to circular if the force between the barrier and the bullet particles is that of an inverse square type. In [6] and in Fig. 1 in this article, it is shown how a change from an inverse square to a spring relation can result

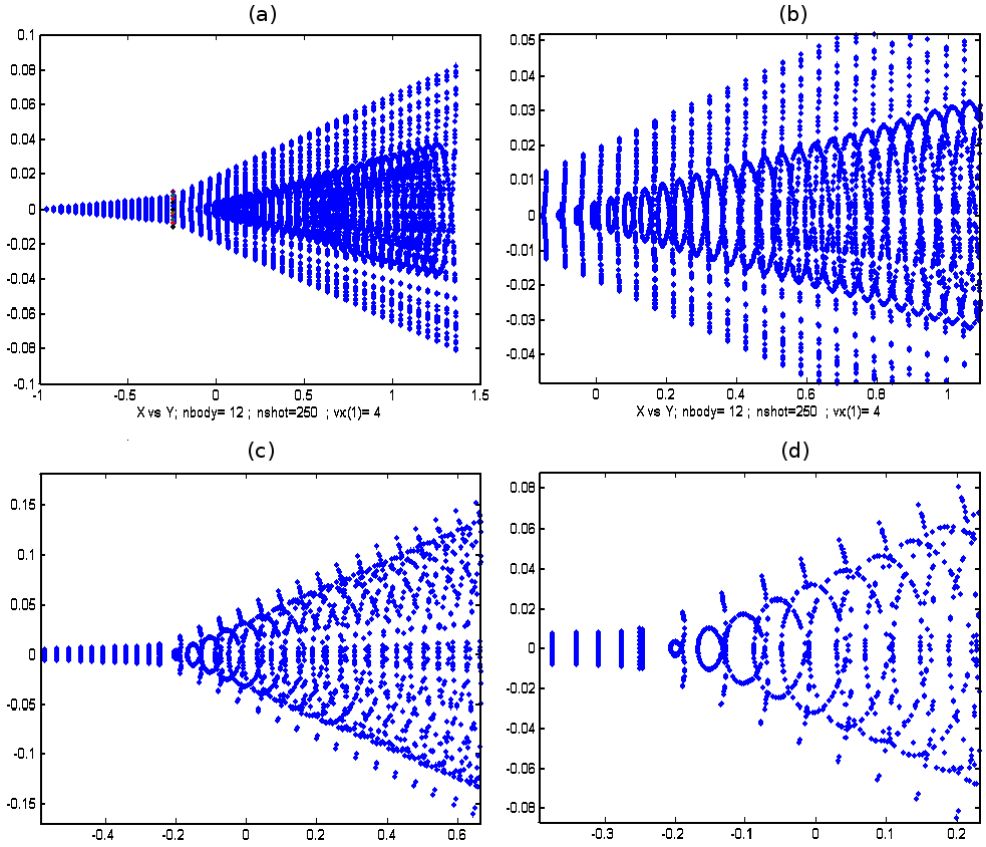

Fig. 3: Wall particles 5:9 (out of 11) are made neutral to mimic a slit. This causes two diffraction patterns interfering with each other. The last two (c), (d), are plotted using the algorithm given in this article with bullet horizontal speed $v_x = 3.2$.

in the case of large interacting particles as those of the barrier (and mimicked here by having fixed particles). This picture is equivalent to what happens in field theory in which a potential equation (resulting from inverse square relation) acquires wave solutions due to the presence of a boundary. This effect occurs in the case of waves in fluids and solids which are composed essentially of particles interacting under an inverse square environment.

The present results upholds the fact that particles behave like waves and particles, but differs in giving a more natural explanation that agrees with common logic and classical laws. It is difficult to believe at the end that classical laws that apply to planets composed of trillions of particles fail when considering few of them. The particle picture is simple to comprehend and can also afford to explain many of the relativistic and quantum findings in physics (see [7, 8] by this author for more on this).

For deeper understanding of the present results, it is useful to do a complementary theoretical analysis to overcome the finite time step effects inherent in any numerical solution. Further understanding of the problem may be achieved by using more elaborate particles where spin and moments are to be taken into consideration.

Submitted on February 09, 2010 / Accepted on February 16, 2010

References

1. Feynman, Richard P. The Feynman lectures on physics. *Addison-Wesley*, 1965, v. 3.
2. Jönsson C. Electron diffraction at multiple slits. *American Journal of Physics*, 1974, v. 4.
3. Nairz O., Arndt M., and Zeilinger A. Quantum interference experiments with large molecules. *American Journal of Physics*, 2003, v. 71.
4. Summhammer J., Rauch H., Tuppinger D. *Phys. Rev. A*, 1987, v. 36.
5. Greene B. The fabric of the cosmos: space, time, and the texture of reality. Vintage, 2000.
6. Landau L. D., Lifshitz E. M. Mechanics. Pergamon press, 1960.
7. Al Rabeh R. H. Primes, geometry and condensed matter. *Progress in Physics*, 2009, v. 3.
8. Al Rabeh R. H. New ideas for the extra dimensions and for deriving the basic laws of physics. *Progress in Physics*, 2010, v. 1.

Some Unsolved Problems, Questions, and Applications of the Brightsen Nucleon Cluster Model

Florentin Smarandache

Department of Mathematics, University of New Mexico, Gallup, NM 87301, USA. E-mail: smarand@unm.edu

Brightsen Model is opposite to the Standard Model, and it was build on John Weeler's Resonating Group Structure Model and on Linus Pauling's Close-Packed Spheron Model. Among Brightsen Model's predictions and applications we cite the fact that it derives the average number of prompt neutrons per fission event, it provides a theoretical way for understanding the low temperature / low energy reactions and for approaching the artificially induced fission, it predicts that forces within nucleon clusters are stronger than forces between such clusters within isotopes; it predicts the unmatter entities inside nuclei that result from stable and neutral union of matter and antimatter, and so on. But these predictions have to be tested in the future at the new CERN laboratory.

According to the Brightsen Nucleon Cluster Model [1] all nuclides of beta stable isotopes can be described by three fundamental nucleon clusters (NPN, PNP, NP), with halo clusters (NN, PP, NNN) now experimentally observed. The Brightsen model builds on the early cluster models of the Resonating Group Structure of John Wheeler [2] and the Linus Pauling Close-Packed Spheron Model [3], which predict mathematically that the wave function of a composite nucleus can be viewed quantum mechanically as a combination of partial wave functions that correspond to the multiple ways nucleons (protons, neutrons) can be distributed into close-packed clusters, thus rejecting the standard model Hartree-Fock formalism of average field interactions between independent nucleons in nuclear shells. Presented in this section are a number of unsolved problems, questions, and future experimental pathways based on the Brightsen Nucleon Cluster Model formalism–many additional applications can be gleamed from careful study of the literature cited in the references provided:

1. The Brightsen Model derives the average number of prompt neutrons per fission event for many radioactive isotopes of human importance (U-235, U-233, Pu-239, Pu-241) as well as emission of light charged particles, suggesting that all modes of fission derive from a four step process [4]. Further study of these claims are warranted given the importance of understanding the fission of radioactive isotopes for energy production.

2. The Brightsen Model provides a theoretical pathway for experimentalists to understand the numerous laboratory results of low temperature transformation/low energy reactions, such as the well studied ^{104}Pd (p, alpha) ^{101}Rh reaction [5]. Application of the Brightsen Model to low energy fusion reactions as a possible result of interactions between nucleon clusters is of fundamental importance to human energy demands.

3. The Brightsen Model predicts the existence of "unmatter entities" inside nuclei [6], which result from stable and neutral union of matter and antimatter nucleon clusters. As a result, the Brightsen Model predicts that antimatter has corresponding antigravity effects [7]. This prediction can be tested in the future at CERN beginning 2008 using antihydrogen. Once accurate measurements can be made of the gravitational acceleration of antihydrogen, and the results compared with matter hydrogen, if the two forms have opposite acceleration, then a major prediction of the Brightsen Model will be confirmed (e.g., that antimatter has both anti-gravity effect and anti-mass). If experimentally confirmed, then predictive equations will need to be developed using the Brightsen Model formalism of union of matter and antimatter clusters (e.g., the unsolved mathematical formation of unmatter entities inside nuclei). The importance of this aspect of the Brightsen Model links to the current problem in physics of the missing matter of the universe and possible unification of gravity at relativistic (macroscopic) and quantum (microscopic) states.

4. The Brightsen Model offers a theoretical approach for artificially induced fission of dangerous radioactive nuclei to produce relatively stable elements [5]. In theory, if externally produced electromagnetic radiation can be caused to resonate with the exact magnetic moment of a specific sub-nuclear nucleon cluster (e.g., NPN, PNP, NP nucleon clusters), than an individual nucleon cluster can in theory be excited to a energy such that it is expelled from the nucleus, resulting in transmutation of the parent isotope via fission and/or beta or alpha decay to less radioactive daughter structures. The applications of this process for nuclear energy production are clear and worthy of experimental test.

5. The Brightsen Model predicts that one sub-cluster isodyne [5] of the very stable Helium-4 isotope consists of two weakly stable deuteron [NP] clusters, each with their own distinct energy level, spin, magnetic moment, etc. Experimental tests are needed to confirm this fundamental model prediction. If confirmed, new physics mathematical description of shell structure of isotopes would follow.

6. The Brightsen Model predicts that forces "within" nucleon clusters (NPN,PNP,NP) are stronger that forces "between" such clusters within isotopes, a result of different combinations of the spin doublet and triplet clusters. It is predicted that research here would result in new measurable macroscopic properties of atomic nuclei including new fundamental force interactions.

7. The Brightsen Model predicts that the next "magic number" will be found at $N = 172$, $Z = 106$, $A = 278$ (Seaborgium-278). Experimental confirmation of this prediction would require a revised explanation of magic numbers in isotopes based on nucleon clusters as the fundamental building blocks of shell structure in atomic nuclei, as opposed to independent nucleons in an average field.

8. The Brightsen Model predicts that the large cross section of Boron-10 (as opposed to the small cross section of Boron-11) results from the presence of a stable and independent nucleon cluster structure [PNP], which coexists with two [NP] and one [NPN] clusters that maintain very small cross sections. Thus the vast majority of the cross section dynamics of Boron-10 is predicted by the Brightsen Model to derive from a strongly interacting [PNP] cluster. This four cluster formalism for Boron-10 (e.g., 1PNP, 2NP, 1NPN) also correctly derives the $I = 3$ spin experimentally observed.

Submitted on February 18, 2010 / Accepted on February 22, 2010

References

1. Brightsen R. A. Nucleon cluster structures in beta-stable nuclides. *Infinite Energy*, 1995, v. 1, no. 4, 55.
2. Wheeler J. A. On the mathematical description of light nuclei by the method of resonating group structure. *Physical Review*, 1937, v. 52, 1107.
3. Pauling L. The close-packed spheron theory and nuclear fission. *Science*, 1965, v. 150, no. 3694, 297.
4. Brightsen R. A. The nucleon cluster model and thermal neutron fission. *Infinite Energy*, 2000, v. 6, no. 31, 55.
5. Bass R. A. Experimental evidence favoring Brightsen's nucleon cluster model. *Infinite Energy*, 1996, v. 2, no. 11, 78.
6. Smarandache F., Rabounski D. Unmatter entities inside nuclei, predicted by the Brightsen nucleon cluster model. *Progress in Physics*, 2006, v. 1, 14.
7. Nelson W. D. New astronomical data finds support in the nucleon cluster model. *Journal of New Energy*, 1998. v. 3. no. 1, 1.

Cosmophysical Factors in the Fluctuation Amplitude Spectrum of Brownian Motion

Alexander V. Kaminsky* and Simon E. Shnoll†

*Elfi-tech Ltd., Rekhovot, Israel
†Department of Physics, Moscow State University, Moscow 119992, Russia
†Inst. of Theor. and Experim. Biophysics, Russian Acad. of Sci., Pushchino, Moscow Region, 142290, Russia
†Puschino State University, Prospect Nauki 3, Pushchino, Moscow Region, 142290, Russia
E-mail: shnoll@mail.ru

Phenomenon of the regular variability of the fine structure of the fluctuation in the amplitude distributions (shapes of related histograms) for the case of Brownian motion was investigated. We took an advantage of the dynamic light scattering method (DLS) to get a stochastically fluctuated signal determined by Brownian motion. Shape of the histograms is most likely to vary, synchronous, in two proximally located independent cells containing Brownian particles. The synchronism persists in the cells distant at 2 m from each other, and positioned meridionally. With a parallel-wise positioning of the cells, high probability of the synchronous variation in the shape of the histograms by local time has been observed. This result meets the previous conclusion about the dependency of histogram shapes ("fluctuation amplitudes" of the spectra of stochastic processes) upon rotation of the Earth.

1 Introduction

The works surveyed in [1–3] revealed a determinate variation in the spectra of the fluctuation amplitudes (these are the shapes of the related histograms in the characteristics of the various processes under measurement, ranging from the rates of chemical and biochemical reactions to the noises in gravity-gradient antennae and semiconductor circuits, and to radioactive decay). This paper represents data of a similar study of the process of Brownian motion.

2 Subject, materials, and methods

In 2006, we studied variations in the shapes of the histograms obtained from measurements of the fluctuations of the velocity of Brownian motion in an aqueous suspension of ZnO (average particle size: 5 μm). We obtained proofs of the synchronous variations in the histograms plotted according to the measurement data in independent "generators", placed on a lab bench.

In 2009, the same experiments were retried using 450-nm polystyrene microspheres (manufactured by Polysciences Inc.) with applying an improved measurement technique. The known method of dynamic light scattering (DLS) [4] was applied to measure the fluctuations of the velocity of Brownian motion. The method is based on the measurement of the fluctuations in coherent light scattering across an ensemble of the moving particles. In practice, a collimated laser beam was passed through a glass cell containing suspension of Brownian particles.

Electromagnetic waves, diffracted on the suspended particles, give a rise to a stochastically fluctuating intensity at the detector plane and corresponding photocurrent

$$i(t) \sim \langle E(t)\, E(t)\rangle.$$

Here, the angle parentheses denote the average of the rapid optical oscillations. A schematic diagram of the experimental installation is shown in Fig. 1.

We took an advantage of the "backscatter" geometry and a multiple scattering mode in our installation. Two identical optical cells (we refer to these as *Brownian signal generators*) were used. Each cell consisted of a 1-mm-spacing glass cell filled with a suspension, and an optoelectronic unit comprising a laser diode, a photodiode, and a preamplifier. Photo currents $i_1(t)$ and $i_2(t)$ of the detector were converted into voltage by trans-impedance amplifiers, whose conversion factor is $r = 10$ MOhm, then were saved on a PC hard disk following digitization in a 42 KHz 12-digit two-channel analog-to-digital converter. The detectors were differential pin photodiodes by Hamamatsu Co. Ltd. The lasers were single-mode VCSEL structures (wavelength: $\lambda = 850$ nm; emission bandwidth: ~100 MHz; radiant energy: 1 mW) manufactured by RayCan. Special steps were taken to exclude potential synchronous interference: the sensors were placed on a vibroisolated table; both lasers and the power supply circuits of the amplifiers were separated and duly filtered. A high-pass filter with cutoff frequency below 30 Hz was used in the amplification path to minimize vibration-related synchronous interference.

Fig. 2 shows a segment of photocurrent time series $i_1(t)$ in one of the Brownian generators. The signal's shape is typical of persistent signals.

The above autocorrelation function of the signal, for moderately large numerical values of τ, is described by an exponent $C(\tau) = \exp(-q^2 D\tau)$ with die-away time determined by the geometry of the scattering and diffusion coefficient $D = kT/3\pi\eta d$ (Stokes-Einstein formula), where k is Boltzmann's constant, T is temperature, η is viscosity, and d is the

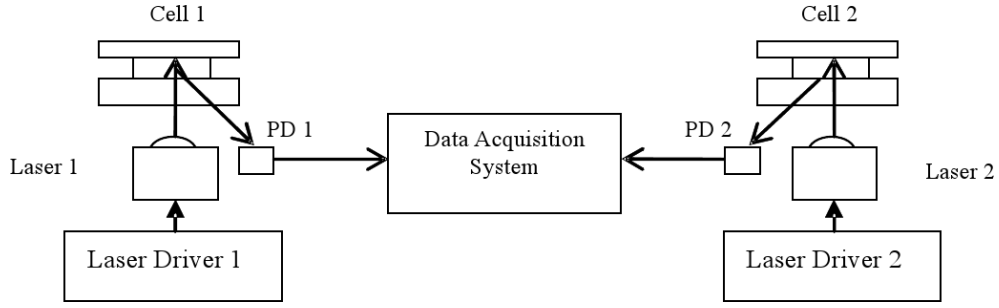

Fig. 1: A schematic diagram of the experimental installation.

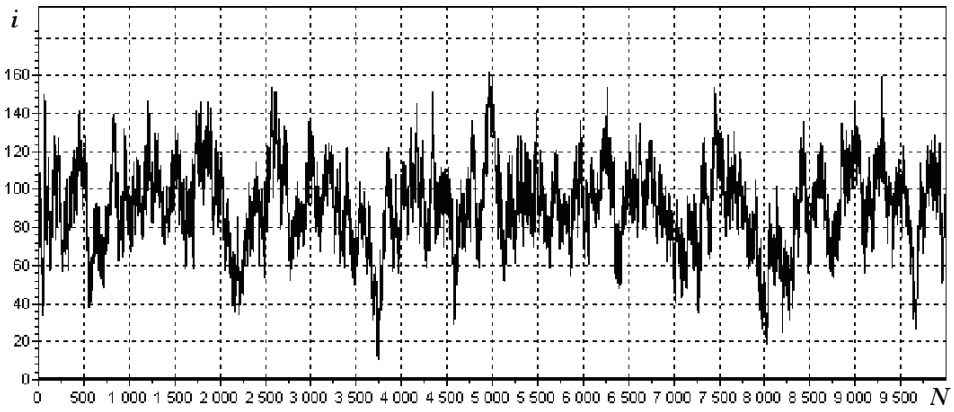

Fig. 2: A segment of time series: a result of DLS signal measurements taken from 1 "generator": 10,000 measurements of $1/8,000 = 1.2 \times 10^{-4}$ duration each.

particle's diameter. The numerical value of q determines the momentum transfer of a photon in scattering on the Brownian particles. The power spectrum is of Lorentzian-like shape is $S(\varpi) \sim \varpi_0/(\varpi_0^2 + \varpi^2)$, where $\varpi_0 = 1/T_0$ is the relaxation frequency. With $\varpi \gg \varpi_0$, the spectrum is approximated by a power-law dependence. Similarly, in the time-domain representation, the correlation function may be approximated by the power-law dependence in the area of $\tau \ll T_0$.

In our case, the DLS signal is described by a fractional Brownian motion model [5]. The signal is self-similar at the high-frequency range of >100 Hz, and an asymptotic behavior of the correlation function under $\tau' = q^2 D\tau \to 0$ is of the power-law nature: $C(\tau) = 1 - |\tau'|^\alpha$. Here α is a scaling parameter related to the fractal dimension $D = 2 - \frac{1}{2}\alpha$. At low frequencies we have $\tau \to \infty$ and $C(\tau) = |\tau'|^{-\beta}$, where β is the scaling parameter related to the Hurst coefficient: $\beta = 2 - 2H$.

The following characteristics of the time series were obtained for the DLS signal of the Brownian generators. They are: $\alpha \approx 0.7$, $D \approx 1.65$, $H = 0.82 \pm 0.1$.

Fig. 3a shows the autocorrelation function of a signal for one of the channels: $g_{11} = \langle i_1(t)\, i_1(t+\tau)\rangle$, while Fig. 3b shows the cross-correlation function between the channels: $g_{12} = \langle i_1(t)\, i_2(t+\tau)\rangle$.

As seen in 3b, there is no significant physical link between the channels. This might lead to a correlation moment different from 0. Insignificant near-zero-line fluctuations of the cross-correlation function g_{12} tend to 0 under bigger statistics figures.

3 Histogram plotting and shape examination

Amplitude distribution of the histograms were plotted using 30 or 60-measurement series segments. For better convenience of visual comparing, the said histograms were made smooth by the moving summation technique. All the procedures of histogram plotting, smoothing, and scaling were carried out using *Histogram Manager* software developed by Edwin Pozharsky (see [1] for detail).

We consider the histograms to be similar if visual similarity of their shapes can be attained by applying admissible expansion and mirror reflection operations. In other words, the "hystogram shape" can be articulated as an invariant of a subgroup of affine transformations in a plane involving operations of scaling, parallel translation, and X-axis reflection.

The histogram plotting and shape examination methods are given with requisite particularization used in the studies published in [1].

Fig. 4 shows a chunk of a computer archives: a sequence of the histograms based on the data obtained from the measurements produced in two independent Brownian generators. The histograms were plotted according to the data of

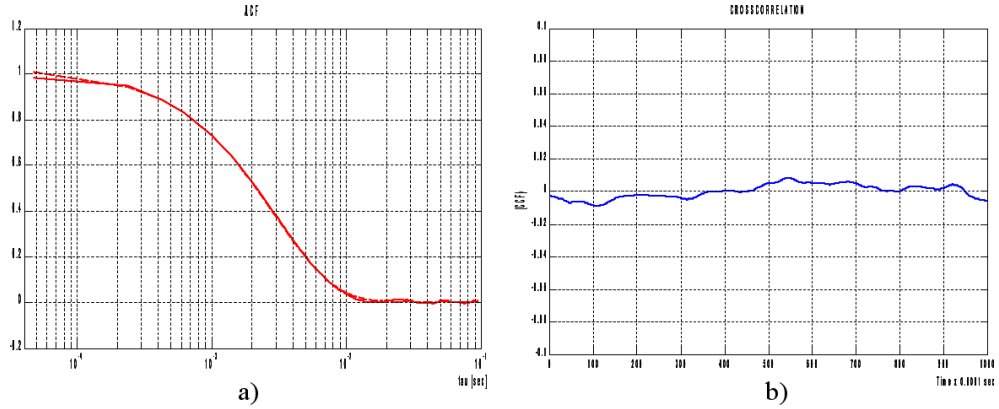

a) b)

Fig. 3: Autocorrelation (a) and cross-correlation (b) functions for the signals of two "Brownian generators" in our experiment.

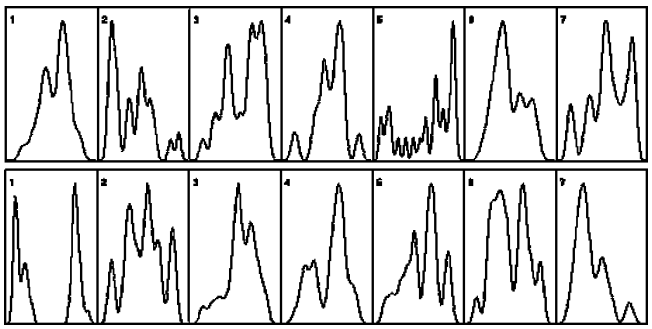

Fig. 4: A chunk of a computer archives: a sequence of the histograms based on the data obtained from the measurements produced in two independent Brownian generators. X-axis in each histogram represents values (in relative units) of the photocurrent in the mesurement of Brownian motion. Y-axis gives the number of similar pairs which correspond to the specific values of the photocurrent. The histograms are given after a 17-fold moving-summation smoothing.

30 measurements, and given a 17-fold smoothing. The upper and lower rows show No. 1 and No. 2 generator's histograms, correspondingly. Numbers of the sequential histograms are shown. The total of the sequential histograms amounted to several thousands.

4 Synchronous variation of the shape of the histograms in the measurements of Brownian motion on the independent "generators" in the same location

Fig. 5 shows a chunk of computer archives representing the pairs of *synchronous* histograms plotted on the basis of the data obtained by independent measurements in two installations found to be similar by experts. Numbers of the histograms in the time series are given. As seen in Fig. 5, the synchronous histograms turn out to be similar in shape.

In plotting a distribution of the number of similar pairs of the histograms, according to the values of the related separating intervals, a particularly large number of the similar pairs corresponds to some intervals. This is in exact a core evidence of a non-random nature of the similarity of the histograms in independent processes.

Nos. of synchronous histograms in two arrays	N_1 (array 1)	$P_1 = \frac{N_1}{720}$	N_2 (array 2)	$P_2 = \frac{N_2}{720}$
8	6	0.008	5	0.007
59	1	0.001	3	0.004
232	4	0.006	6	0.008
294	17	0.024	7	0.010
457	2	0.003	13	0.018
		3×10^{-12}		4×10^{-11}

Table 1: Occurrence frequency of the histograms of the shape under measurements produced in two independent Brownian generators during 24.09.2009 experiment (Fig. 8).

Fig. 6 shows a distribution of the number of similar pairs of the histograms plotted according to the data obtained by the measurements of Brownian motion in two independent generators.

As seen in Fig. 6, the number of the synchronous pairs is definitely above the "background". The height of the central log is equal to 89 pairs with 720 histograms in the rows, that is about 12% of the maximumally possible height. In the other intervals, the height of the logs is about 2.5% of the maximumally possible height. Making the use of majorizing estimation by $\sqrt{N}$ criterion is enough to evaluate the reliability of the inference on the synchronous variation of the histogram shape in independent Brownian generators. The figure shows that the central crest's height differs from the "background" by around $6\sqrt{N}$ which corresponds to a 10^{-11} probability for obtaining such a result at random.

It should be noted that according to Fig. 5 the histograms, forming the central log in Fig. 6 and evidencing the synchronous nature of the shape variation of the histograms in independent processes, do not have an apparent difference from the histograms that would correspond to other intervals. In other words, there is no definite shape specifically corresponding to the synchronous variation of the histogram shape.

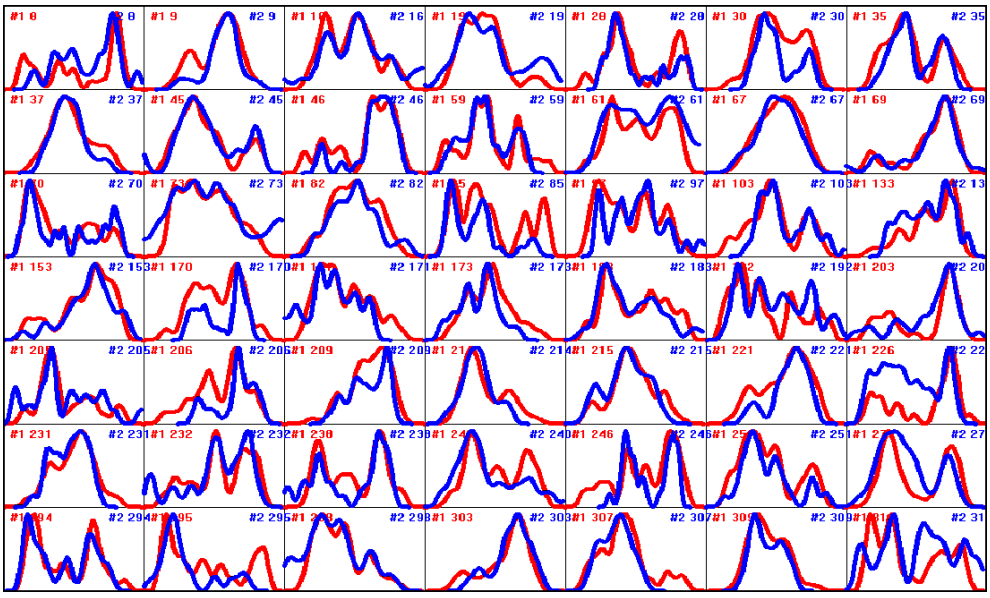

Fig. 5: A log piece: pairs of the histograms plotted on the basis of the data obtained by independent synchronous measurements in two independent Brownian generators found to be similar by an expert evaluation. Numbers of the histograms in the time series are given. Coordinate axes are the same as in Fig. 4.

However, a relatively small number of rare, "exotic" shapes can be found among the histograms that correspond to the central log. The pairs of such histograms can be used for an additional evaluation of the reliability of the core inferences.

At this point, we assume that realization of a complex-shaped histogram is per se an unlikely event to occur. A simultaneous occurrence of rare events in independent measurements is even a less probable event to happen. This evaluation has proven to be very strong. Illustration to this evaluation is given in Fig. 7 and Table 1. Fig. 7 shows 5 pairs of rare-shape histograms obtained synchronously during the 24.09.2009 experiment (there was 89 similar synchronous pairs, all-in-all). We can see, for example, that out of these 720 possible histograms, there was 6 No. 8 histograms in row 1 of the first array, and 5 ones in row 2, thus constituting 0.008 and 0.007 fractions out of the maximal values, respectively.

These fractions do come as an evaluation of the probability of a random occurrence of the given-shape histograms at this particular spot. The general probability of the uncertainty of the inference on a synchronous occurence of similarly-shaped histograms in two independent rows of measurement is equal to the product of these special-case probabilities. For example, given the 5 rare-shape histograms, this general probability constitutes $P_1 = 3{\times}10^{-12}$ for the first array, and $P_2 = 4{\times}10^{-11}$ for the second one, i.e., vanishing small values. It should be noted, however, that the number of the synchronous pairs of the rare-shape histograms is considerably large. Thus, the reliability of the inference on the synchronous occurrence of the similarly-shaped histograms in the independent Brownian generators is proven by these two types of evaluation.

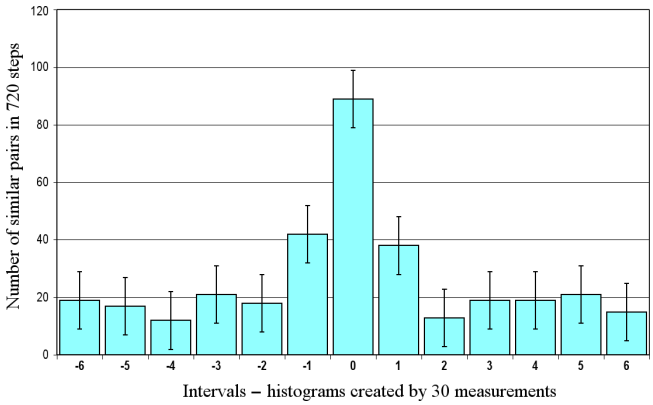

Fig. 6: Shapes of the histograms in the independent Brownian generators vary synchronously. Similar pairs of the histograms are distributed according to the values of the respective separating intervals of time. Date of the experiment: 24.09.2009. Each histogram is plotted according to the data of 30 measurements. X-axis shows values of the time intervals separating similar histograms. One interval is equal to 3.6×10^{-3} seconds.

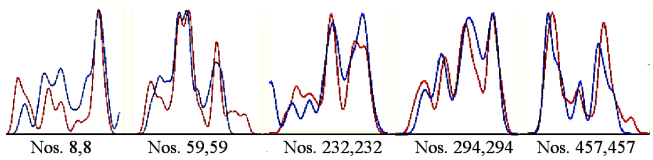

Fig. 7: Examples of the similarity in the rare-shape synchronous histograms according to the occurrence frequency shown in Table 1.

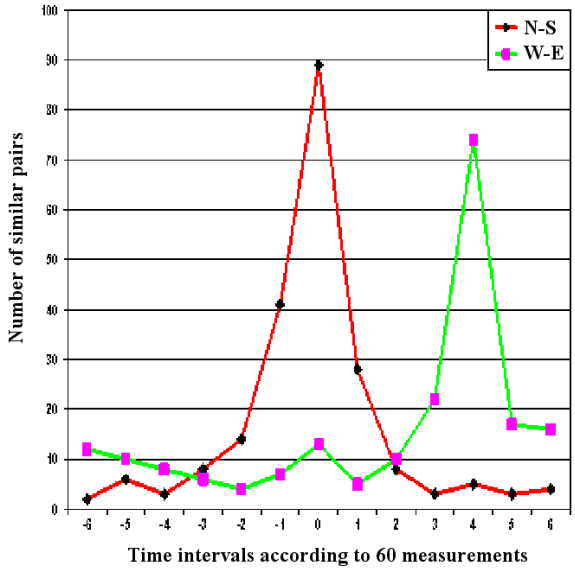

Fig. 8: Interval distribution of the number of similar pairs of the histograms plotted according to the results of 60 measurements produced in two independent Brownian generators which were distant at 200 cm from each other. A) Meridian (from North to South) positioning of the generators; B) Parallel-wise positioning of the generators. In the meridian positioning, the similar histograms occur in the two generators simultaneously. In the parallel-wise positioning, similar histograms of West generator occur 4 interval (11.6 msec) later than they do in the East one.

5 Synchronism in different locations

Similarity of the shape of the histograms obtained during independent measurements taken in *different locations at the same local time* comes as an evidence of the dependency of the histogram shape upon rotation of the Earth. Earlier we obtained this evidence by conducting experiments measuring radioactivity at an extremely near distance between the laboratories: at Pustchino (54°N, 37°E) and in Antarctic (Novolazarevskaya Station, 70°S, 11.5°E), so the distance is about 14,000 km. In the works [6–9], when measuring the noise in semiconductor circuits, a "local time effect" was obtained at a distance of about 1 meter. We carried out similar measurements using the "Brownian generators".

Figs. 8 and 9 show results of the experiments conducted at the town of Rekhovot, Israel (31.89°N, 34.80°E) on October 11, 2009. Two Brownian generators were distant as $\Delta L = 2$ meters from each other, and were first oriented by the Meridian, then by the Parallel. The signals were recorded for 4 minutes. Local time delay for the said latitude with the basic East-West orientation constitutes $\Delta T = \Delta L/V$ sec, where $V \approx 2\pi 6378000 \cos(31.89\pi/180)/86400$ m/sec is the speed of the present point of the Earth's surface bearing the above specified coordinates. With sampling frequency of 42 KHz, this delay value corresponds to 3.6 histograms plotted by 60 points, and to 7.1 histograms plotted by 30 points. As seen in the drawings below, the time intervals, where the maximal

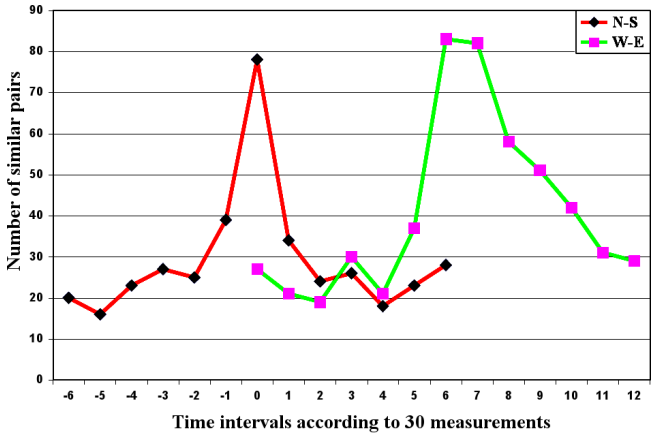

Fig. 9: Interval distribution of the number of similar pairs of the histograms plotted according to the results of 30 measurements produced in two independent Brownian generators at a distance of 200 cm from each other. The local-time synchronism has a more distinct manifestation under the 30-result plotting. In the meridian positioning of the independent generators, similar histograms occur simultaneously. In the parallel-wise positioning, similar histograms of West generator occur in West generator 7–8 intervals later than they do in the East one.

number of the similarly-shaped histograms is found, are close to the estimated values.

6 Discussion

Our study of Brownian motion by means of the dynamic light scattering method showed that the fine structure of the distribution of intensity fluctuations of the light, scattered by Brownian particles (shapes of the corresponding histograms) varies synchronously by local time. In other words, Brownian motion is specific for the same regularities as those found previously during examination of stochastic processes of a different nature, namely — those of chemical reactions, thermal fluctuation in resistors, radioactive decay etc. Thus, the similar regularities in the processes, where the energy changing range varies by many orders, show up the same space-time being the only thing in common. Proceeding from this fact, a conclusion was made according to which the observed regularities were explained by the space-time fluctuations determined by the motion of the Earth in a surrounding inhomogeneous gravitational field [1–3].

Acknowledgements

We are grateful to Prof. P. S. Lande for her valuable discussion and interpretation of the results. Our thanks also come to Head of the Chair of Biophysics of Department of Physics of the Moscow State University Prof. V. A. Tverdislov, and to the workers of the Laboratory of Physical Biochemistry of Institute of Theoretical and Experimental Biophysics of the Russian Academy of Science (Prof. D. P. Kharakoz) for their very valuable discussion. We are tremendously grateful to

Ms. Anna A. Andreyeva for her mission as the second independent expert who compared the histograms in this study.

Submitted on January 21, 2010 / Accepted on February 04, 2010

References

1. Shnoll S. E. Cosmic physical factors in random processes. Svenska fysikarkivet, Stockholm, 2009, 388 pages.
2. Shnoll S.E. and Rubinstein I.A. Regular changes in the fine structure of histograms revealed in the experiments with collimators which isolate beams of alpha-particles flying at certain directions. *Progress in Physics*, 2009, v. 2, 83–95.
3. Shnoll S.E. The "scattering of the results of measurements" of processes of diverse nature is determined by the Earth's motion in the inhomogeneous space-time continuum. The effect of "half-year palindromes". *Progress in Physics*, 2009, v. 1, 3–7.
4. Goldburg W. I. Dynamic light scattering. *Am. J. Phys.*, 1999, v. 67, no. 12.
5. Beran J. Statistics for long-memory processes. Chapman & Hall, New York, 1994.
6. Panchelyuga V.A., KolombetV.A., Pancheluga M.S., and Shnoll S.E. Local-time effect on small space-time scale. In: *Space-Time Structure*, collected papers, Tetru, Moscow, 2006, 344–350.
7. Panchelyuga, Kolombet V.A., Kaminsky A.V., Pancheluga M.S., and Shnoll S.E. Experimental investigation of the existence of a local-time effect on the laboratory scale and the heterogenety of space-time. *Progress in Physics*, 2007, v. 1, 64–69.
8. Kaminsky A.V., Shnoll S.E. The study of synchronous (by local time) changes of the statistical properties of thermal noise and alpha-activity fluctuations of a 239-Pu sample. arXiv: physics/0605056.
9. Panchelyuga V.A., Kolombet V.A., Kaminsky A.V., Pancheluga M.S., and Shnoll S.E. Local-time effect observed in noise processes. *Bull. of Kaluga University*, 2006, no. 2b, 3–8.

Strong Nuclear Gravitational Constant and the Origin of Nuclear Planck Scale

U. V. S. Seshavatharam* and S. Lakshminarayana†

*Spun QA Engineer, Lanco Industries Ltd, Srikalahasti, A.P, 517641, India. E-mail: seshavatharam.uvs@gmail.com

†Department of Nuclear Physics, Andhra University, Visakhapatnam, AP, 530003, India. E-mail: lnsrirama@yahoo.com

Whether it may be real or an equivalent, existence of strong nuclear gravitational constant G_S is assumed. Its value is obtained from Fermi's weak coupling constant as $G_S = 6.9427284\times10^{31}$ m^3/kg sec^2 and thus "nuclear planck scale" is defined. For strong interaction existence of a new integral charged "confined fermion" of mass 105.383 MeV is assumed. Strong coupling constant is the ratio of nuclear planck energy = 11.97 MeV and assumed 105.383 MeV. $\frac{1}{\alpha_s} = X_s$ is defined as the strong interaction mass generator. With 105.383 MeV fermion various nuclear unit radii are fitted. Fermi's weak coupling constant, strong interaction upper limit and Bohr radius are fitted at fundamental level. Considering Fermi's weak coupling constant and nuclear planck length a new number $X_e = 294.8183$ is defined for fitting the electron, muon and tau rest masses. Using X_s, X_e and α 105.32 = 0.769 MeV as the Coulombic energy constant = E_c, energy coefficients of the semi-empirical mass formula are estimated as $E_v = 16.32$ MeV, $E_s = 19.37$ MeV, $E_a = 23.86$ MeV and $E_p = 11.97$ MeV where Coulombic energy term contains $[Z]^2$. Starting from $Z = 2$ nuclear binding energy is fitted with two terms along with only one energy constant = 0.769 MeV. Finally nucleon mass and its excited levels are fitted.

1 Introduction

It can be supposed that elementary particles construction is much more fundamental than the black hole's construction. If one wishes to unify electroweak, strong and gravitational interactions it is a must to implement the classical gravitational constant G in the sub atomic physics. By any reason if one implements the planck scale in elementary particle physics and nuclear physics automatically G comes into subatomic physics. Then a large arbitrary number has to be considered as a proportionality constant. After that its physical significance has to be analyzed. Alternatively its equivalent "strong nuclear gravitational constant G_S can also be assumed. Some attempts have been done in physics history [1–5]. Whether it may be real or an equivalent if it is existing as a "single constant" its physical significance can be understood. "Nuclear size" can be fitted with "nuclear Schwarzschild radius". "Nucleus" can be considered as "strong nuclear black hole". This idea requires a basic nuclear fermion! Nuclear binding energy constants can be generated directly. Proton-neutron stability can be studied. Origin of "strong coupling constant" and "Fermi's weak coupling constant" can be understood. Charged lepton masses can be fitted. Authors feel that these applications can be considered favorable for the proposed assumptions and further analysis can be carried out positively for understanding and developing this proposed "nuclear planck scale"

2 Proposed assumptions

1. Strong nuclear gravitational constant can be given as $G_S = 6.94273\times10^{31}$ m^3/kg sec^2;
2. There exists a strongly interacting "confined" Fermionic mass unit $M_{Sf}c^2 = 105.383$ MeV. With this assumption in particle physics "super symmetry in strong and weak interactions" can be understood very easily [6];
3. Strong interaction mass generator $X_S = 8.8034856$ and Lepton mass generator $X_E = 294.8183$;
4. In the semi-empirical mass formula ratio of "Coulombic energy coefficient" and the proposed 105.383 MeV is equal to α. The Coulombic energy constant E_C = 0.769 MeV.

2.1 Planck scale Coulombic energy and the unified force

Let

$$M_Pc^2 = \text{planck energy} = \sqrt{\frac{\hbar c^5}{G}} = \sqrt{\hbar c\,\frac{c^4}{G}}\,. \qquad (1)$$

Multiplying this energy unit with $\sqrt{\alpha}$, we get

$$\sqrt{\alpha}M_Pc^2 = \sqrt{\frac{e^2}{4\pi\epsilon_0}\frac{c^4}{G}}\,, \qquad (2)$$

where $\sqrt{\alpha}M_Pc^2$ can be termed as "Coulombic energy", $\frac{c^4}{G}$ is having the dimensions of force and can be considered as the classical limit of any force. This classical force limit $\frac{c^4}{G}$ and the classical power limit $\frac{c^5}{G}$ plays a very vital role in black hole formation and planck scale generation [7]. These are two very important observations to be noted here: $\frac{c^5}{G}$ plays a very crucial role in "gravitational radiation"; using $\frac{c^4}{G}$ minimum distance r_{min} between any two charged particles is given as

$$\frac{e^2}{4\pi\epsilon_0 r_{min}^2} \leqslant \frac{c^4}{G}\,, \qquad (3)$$

$$r_{min} \geqslant \sqrt{\frac{e^2}{4\pi\epsilon_0}\frac{G}{c^4}}\,, \qquad (4)$$

planck mass can be generated if it is assumed that

$$\frac{GM_Pc^2}{r_{min}^2} \leqslant \frac{c^4}{G}\,, \tag{5}$$

$$2\pi r_{min} = \lambda_P = \text{planck wave length}, \tag{6}$$

where, M_P= planck mass and r_{min}= minimum distance between two planck particles. With these two conditions, planck mass can be obtained as

$$M_P = \text{planck mass} = \frac{h}{c\lambda_P} = \sqrt{\frac{\hbar c}{G}}\,. \tag{7}$$

Aim of equations (3, 4, 5, 6 and 7) is to show that there exists a fundamental force of the form $k\frac{c^4}{G} \cong 1.21027{\times}10^{44}$ Newton, where k is a proportionality ratio and is close to unity. This can be considered as the "unified force" of "true grand unification". In the foregoing sections authors show how it changes into the "strong nuclear force".

2.2 Strong nuclear gravitational constant G_S and strong nuclear force

Let the classical gravitational constant be represented by G_C and the assumed strong nuclear gravitational constant be represented by G_S. The most important definition is that

$$\frac{c^4}{G_S} = 116.3463 \text{ Newton} \tag{8}$$

can be called as the "nuclear strong force". This is the beginning of this "nuclear planck scale". Authors request the science community to analyze this equation positively. Magnitude of force of attraction or repulsion in between two nucleons when their distance of separation is close to 1.4 Fermi is

$$\frac{e^2}{4\pi\epsilon_0 R_0^2} \cong \frac{c^4}{G_S}\,, \tag{9}$$

$$R_0 \cong \sqrt{\frac{e^2}{4\pi\epsilon_0}\frac{G_S}{c^4}}\,. \tag{10}$$

If a nucleon of mass m_n revolves at a radius of R_0,

$$\text{potential energy} = E_P = -\frac{e^2}{4\pi\epsilon_0 R_0}\,, \tag{11}$$

$$\text{kinetic energy} = E_K = \frac{m_n v^2}{2} = \frac{e^2}{8\pi\epsilon_0 R_0}\,, \tag{12}$$

$$\text{total energy} = E_T = E_P + E_K = \frac{m_n v^2}{2} = -\frac{e^2}{8\pi\epsilon_0 R_0}\,. \tag{13}$$

We know that the characteristic size of nucleus is 1.3 to 1.4 Fermi. For $R_0 = 1.4$ Fermi total energy of revolving nucleon is close to the rest "energy of electron". This is still a mystery. Hence

$$\frac{e^2}{8\pi\epsilon_0 R_0} \cong \frac{1}{2}\sqrt{\frac{e^2}{4\pi\epsilon_0}\frac{c^4}{G_S}} \cong m_e c^2. \tag{14}$$

Here $m_e c^2$ is the rest energy of electron. Half the classical radius of electron can also be considered as the unit size of nucleus. If so with the assumed strong nuclear gravitational constant G_S it is noticed that

$$R_0 \cong \sqrt{\frac{e^2}{4\pi\epsilon_0}\frac{G_S}{c^4}} \cong \frac{e^2}{8\pi\epsilon_0 m_e c^2} \cong \frac{2G_S m_e}{c^2}\,. \tag{15}$$

This equation (15) clearly suggests that nucleus that we are observing or studying is not a simple object. It is a strange object and can be considered as an "electronic black hole" and works at strong nuclear gravitational constant G_S. Experimentally knowing the (exact) characteristic size of nucleus one can easily estimate the value of proposed G_S. Alternatively its value can be estimated form the famous Fermi weak coupling constant F_W. Considering "planck mass" and "electron mass" in view in a unified manner value of G_S can be obtained from the following 3 semi-empirical relations

$$F_W \cong \frac{1}{3}\left[\ln\left(\frac{\hbar c}{G_C m_e^2}\right)\right]^{-2}\left(\frac{e^2}{4\pi\epsilon_0}\right)^2\left(\frac{G_S}{c^4}\right). \tag{16}$$

This can be obtained from eq. (42, 31, 36, 43, 44 and 28)

$$G_S \cong 3\left[\ln\left(\frac{\hbar c}{G_C m_e^2}\right)\right]^2\left(\frac{4\pi\epsilon_0}{e^2}\right)^2 F_W c^4. \tag{17}$$

Its obtained value is $6.9427284{\times}10^{31}$ $\mathrm{m^3/kg\,sec^2}$. This value is considered in this paper

$$F_W \cong \frac{16\alpha^2}{27}\left(\frac{e^2}{4\pi\epsilon_0}\right)^2\left(\frac{G_S}{c^4}\right). \tag{18}$$

This can be obtained from eq. (42, 31, 36, 43, 44, and 10)

$$G_S \cong \left(\frac{27}{16\alpha^2}\right)\left(\frac{4\pi\epsilon_0}{e^2}\right)^2 F_W c^4. \tag{19}$$

Its obtained value is $6.9052{\times}10^{31}$ $\mathrm{m^3/kg\,sec^2}$. This method is independent of the classical gravitational constant G_C. Another interesting idea is

$$\frac{e^2}{4\pi\epsilon_0 G_S m_e^2} \cong 4, \tag{20}$$

$$G_S \cong \frac{1}{4}\left(\frac{e^2}{4\pi\epsilon_0 m_e^2}\right) \cong 6.9506{\times}10^{31}\ \mathrm{m^3/kg\,sec^2}. \tag{21}$$

Here m_e = rest mass of electron. If this is having any physical meaning without considering the classical gravitational constant G_C value of G_S can be calculated from electron mass directly. Not only that in quark physics in our paper [6] it is assumed that

$$\frac{\text{DCT geometric ratio}}{\text{USB geometric ratio}} \cong 4. \tag{22}$$

2.3 "Strong nuclear force" and "nuclear planck scale"

Similar to the planck scale in unified nuclear physics nuclear scale planck energy can be given as

$$M_n c^2 = \sqrt{\frac{\hbar c^5}{G_S}} = \sqrt{\hbar c \frac{c^4}{G_S}} \cong 11.9705568 \text{ MeV}. \quad (23)$$

These 4 energy coefficients of the semi-empirical mass formula lies in between 11.97 MeV and 2×11.97 = 23.94 MeV. Not only that using this expression in particle physics [6] it can be shown that strongly interacting particles follows energy levels as $[n(n+1)]^{\frac{1}{4}}$ and $\left[\frac{n(n+1)}{2}\right]^{\frac{1}{4}}$ where, n =1, 2, 3... We know that

$$\text{planck length} = \sqrt{\frac{\hbar G_C}{c^3}} = 1.616244\times10^{-35} \text{ meter}. \quad (24)$$

Nuclear planck length can be given as

$$L_n = \sqrt{\frac{\hbar G_S}{c^3}} = 1.664844\times10^{-14} \text{ meter}. \quad (25)$$

Nuclear scale Coulombic energy can be given as

$$M_e c^2 = \sqrt{\frac{e^2}{4\pi\epsilon_0}\frac{c^4}{G_S}} \cong 1.02258 \text{ MeV}. \quad (26)$$

These energy units directly can be implemented in nuclear physics for understanding nuclear structure. Nuclear planck energy $M_n c^2$ or nuclear planck length L_n plays an interesting role in understanding the origin of strong coupling constant [8] and energy coefficients of the semi-empirical mass formula. Lepton masses can also be fitted. It is also noticed that

$$M_{Sf} c^2 E_P^2 \cong \left(M_n c^2\right)^2 E_C. \quad (27)$$

where $M_{sf}c^2$ = proposed new strongly interacting 105.383 MeV, E_P = nucleon's potential energy close to 1.4 Fermi = 2×0.511 MeV, $M_n c^2$ = proposed nuclear scale planck energy = 11.97 MeV, E_C = assumed Coulombic energy coefficient of the semi-empirical mass formula $\alpha M_{Sf} c^2 = \alpha 105.383$ = 0.769 MeV.

3 New strongly interacting fermion (105.38 MeV) and Fermi's weak coupling constant (F_W)

It is assumed that 105.383 MeV is a strongly interacting particle. Authors request that this should not be confused with weakly interacting muon. This particle can be called as sion. Its charge is $\pm e$. Just like quarks it is a confined fermion. It plays a crucial part in understanding the nuclear size, nuclear binding energy, magnetic moments of nucleons and weak interaction. Along with the strong coupling constant it plays a heuristic role in understanding "super symmetry" in strong and weak interactions [6]. Considering "planck mass" and "electron mass" in a unified manner it is empirically defined as

$$\ln\left(\frac{M_P c^2}{m_e c^2}\right)^2 \sqrt{\frac{e^2}{4\pi\epsilon_0}\frac{c^4}{G_S}} \cong 105.3826 \text{ MeV}. \quad (28)$$

Here $M_P c^2$ = planck energy and $m_e c^2$ = rest energy of electron. Classical radius of $M_{Sf} c^2$ can be given as

$$\frac{e^2}{4\pi\epsilon_0 M_{Sf} c^2} = 1.3664\times10^{-17} \text{ meter}. \quad (29)$$

Compton length of $M_{Sf} c^2$ can be given as

$$\frac{\hbar}{M_{Sf} c} = 1.87245\times10^{-15} \text{ meter}. \quad (30)$$

This length can be considered as the strong interaction upper limit.

3.1 Various nuclear unit sizes and the mystery of 1.4 Fermi

Let

$$\frac{\hbar}{M_{Sf} c} = 1.87245\times10^{-15} \text{ meter} = a\,, \quad (31)$$

$$\frac{\hbar}{2M_{Sf} c} = 0.93624\times10^{-15} \text{ meter} = b\,. \quad (32)$$

Here a can be considered as the upper limit of strong interaction range and b can be considered as lower limit of strong interaction. Considering these two lengths as the semi-major axis and semi-minor axis of the nucleus it is noticed that

$$\text{arthematic mean of } (a,b) = \left[\frac{a+b}{2}\right] \cong 1.404 \text{ Fermi}, \quad (33)$$

$$\text{geometric mean of } (a,b) = \left[\sqrt{ab}\right] \cong 1.324 \text{ Fermi}, \quad (34)$$

$$\text{harmonic mean of } (a,b) = \left[\frac{2ab}{a+b}\right] \cong 1.248 \text{ Fermi}. \quad (35)$$

These sizes can be compared with the experimental values of various nuclear unit or characteristic sizes. From equation (33) it is noticed that arithmetic mean of semi-major and semi-minor axis of the assumed nuclear size = 1.404 Fermi. From this coincidence "existence of the strongly interacting 105.383 MeV" can be justified

$$R_0 \cong \frac{3}{4}\frac{\hbar}{M_{Sf} c} \cong 1.40436 \text{ Fermi}, \quad (36)$$

$$E_T = \frac{e^2}{8\pi\epsilon_0 R_0} \cong \frac{2}{3}\left(\alpha M_{Sf} c^2\right) \cong 0.512676 \text{ MeV}. \quad (37)$$

This idea suggests that a nucleon revolving at 1.404 Fermi having a total energy of 0.51267 MeV which is close to the electron rest energy 0.511 MeV. This small energy difference 0.51267−0.511= 0.00167 MeV may be related with origin of massive neutrino. It is assumed that

$$\alpha M_{Sf} c^2 = 0.769 \text{ MeV}, \quad (38)$$

$$\frac{E_T}{E_C} \cong \frac{0.511\ \text{MeV}}{0.769\ \text{MeV}} \cong 0.66445 \cong \frac{2}{3}. \tag{39}$$

Considering $E_T = m_e c^2$ and rearranging this equation we get

$$\frac{M_{Sf}c^2}{E_T} \cong \frac{M_{Sf}c^2}{m_e c^2} \cong \frac{3}{2\alpha}, \tag{40}$$

and from literature [9] it is noticed that

$$\frac{\text{muon mass}}{\text{electron mass}} \cong \left(\frac{3}{2\alpha} + 2\right). \tag{41}$$

Authors here suggest that in equation (41) it is not the muon mass but it is the strongly interacting proposed 105.383 MeV particle.

3.2 Fermi's weak coupling constant and estimation of 105.383 MeV

Empirically Fermi's weak coupling constant F_W [10] can be fitted as

$$F_W \cong \left(\frac{\alpha^2}{2}\right)\left(\frac{e^2}{8\pi\epsilon_0 R_0}\right)a^3. \tag{42}$$

Authors request the science community to consider this equation positively. It has interesting applications. Electron's "total energy" in hydrogen atom can be related with the strong interaction range! From equations (31 and 36)

$$F_W \cong \left(\frac{\alpha^3}{3}\right)\left(M_{Sf}c^2\right)a^3 \cong \frac{1}{3}\left(M_{Sf}c^2\right)\left(\frac{e^2}{4\pi\epsilon_0 M_{Sf}c^2}\right)^3. \tag{43}$$

Experimentally $F_W = 1.435841179{\times}10^{-62}$ J×meter^3

$$\therefore M_{Sf}c^2 \cong \left(\frac{e^2}{4\pi\epsilon_0}\right)\left(\frac{e^2}{12\pi\epsilon_0 F_W}\right)^{\frac{1}{2}} \cong 105.38\ \text{MeV}. \tag{44}$$

3.3 Strong interaction mass generator X_S

Based on nuclear planck scale it is assumed that strong interaction mass generator is

$$X_S \cong \frac{M_{Sf}c^2}{M_n c^2} \cong 8.803486 \cong \frac{L_n}{a}, \tag{45}$$

$$X_S \cong \sqrt{\frac{G_S M_{Sf}^2}{\hbar c}} \cong 8.803486, \tag{46}$$

$$\alpha_s(M_Z) \cong \sqrt{\frac{\hbar c}{G_S M_{Sf}^2}} \cong 0.11359. \tag{47}$$

It is noticed that $X_S = 8.803486 = \frac{1}{0.11359}$ seems to be the "inverse" of the strong coupling constant [8] $\alpha_s(M_Z) = 0.1186 \pm 0.0011\,(\text{exper}) \pm 0.0050\,(\text{theor})$. Considering the lower limits of this value we get $0.1186 - 0.0050\,(\text{theor}) = 0.1136$. We know the importance of the "strong coupling constant" in particle physics. If the proposed definition is found to be true and meaningful one has to accept the existence of proposed "nuclear planck scale". In the sense one must accept the existence of "strong nuclear gravitational constant G_S and existence of 105.383 MeV". This number X_S plays a very interesting role in correlating the energy coefficients of the semi-empirical mass formula and proton-neutron stability. This number plays a crucial role in understanding super symmetry in strong and weak interactions [8].

Based on X_S it is noticed that, $X_S M_{Sf}c^2 = 927.737$ MeV. This is roughly close to proton mass. $X_S M_{Sf}c^2 + M_n c^2 = 939.7$ MeV. This is close to the neutron mass = 939.57 MeV. Some how 105.383 MeV and X_S plays a vital role in "weighing" of the nucleon mass. See Section 5 for "nucleon mass fitting" and nucleon's basic excited levels.

3.4 Fermi's weak coupling constant and the Bohr radius

By any reason for the nucleus if

$$\frac{e^2}{8\pi\epsilon_0 R_0} \cong m_e c^2, \tag{48}$$

$$\frac{e^2}{4\pi\epsilon_0 R_0} \cong 2m_e c^2. \tag{49}$$

Equation(42) takes the following interesting form as

$$F_W \cong \left(\frac{\alpha^2}{2}\right)\left(\frac{e^2}{8\pi\epsilon_0 R_0}\right)a^3 \cong \left(\frac{\alpha^2}{2}\right)\left(m_e c^2\right)a^3. \tag{50}$$

At a glance equation (50) suggests that

$$\left(\frac{\alpha^2}{2}\right)\left(m_e c^2\right) \cong \frac{F_W}{a^3} \cong \left(\frac{\alpha^3}{3}\right)M_{Sf}c^2 \cong 13.65\ \text{eV}. \tag{51}$$

In this equation (51) "left hand side" is nothing but the "total energy of electron" in hydrogen atom. This is a very simple and strange relation! Based on the unification of strong and weak interactions "Bohr radius" of hydrogen atom can be given as

$$a_0 \cong \left(\frac{e^2}{8\pi\epsilon_0}\right)\left(\frac{a^3}{F_W}\right) \cong 5.27745{\times}10^{-11}\ \text{meter}. \tag{52}$$

This is matching with $a_0 = 5.29177{\times}10^{-11}$ meter. This idea suggests that existence of the proposed nuclear strong interaction upper limit a=1.8725 Fermi and strongly interacting $M_{Sf}c^2 = 105.383$ MeV seems to be true and can be considered for further analysis. Their direct existence strongly supports the hidden existence of the proposed strong nuclear gravitational constant G_S.

3.5 Lepton mass generator X_E and electron, muon and tau rest mass fitting

A new number (X_E) is empirically defined [1] as

$$X_E \cong \left[\frac{e^2}{8\pi\epsilon_0 R_0}\frac{L_n^3}{F_W}\right]^{\frac{1}{3}} \cong X_S\left[\frac{e^2}{8\pi\epsilon_0 R_0}\frac{a^3}{F_W}\right]^{\frac{1}{3}}. \tag{53}$$

n	Obtained lepton mass, MeV	Exp. lepton mass, MeV
0	0.5127	0.510998922
1	105.86	105.658369
2	1775.506	1776.9
3	42206.19	Not discovered

Table 1: Fitting of charged lepton rest masses.

Its obtained value is 294.8183. Here L_n = proposed nuclear planck length, a = strong interaction upper limit and F_W = Fermi's weak coupling constant.

This number can be called as "lepton mass generator". It has wide applications in nuclear and particle physics. It is noticed that $(\alpha X_E) = 2.1514$ plays a very interesting role in estimating the quark masses [6]. The weak coupling angle can be considered as $(\alpha X_E)^{-1} = \sin(\theta_W) = 0.4648$. It plays a crucial role in estimating the charged lepton rest masses. It plays a very interesting role in fitting energy coefficients of the semi-empirical mass formula. It can be used for fitting the nuclear size with "Compton wavelength of nucleon". It is noticed that ratio of "nuclear volume" and "A nucleons Compton volume" is X_E. It can be called as the nuclear "volume ratio" factor.

Till now no mechanism is established for the generation of the charged lepton rest masses [11]. Considering equation (39) an interesting empirical relation is given for fitting electron, muon and tau particle rest masses as

$$m_l c^2 \cong \frac{2}{3}\left[E_C^3 + \left(n^2 X_E\right)^n E_A^3\right]^{\frac{1}{3}}, \tag{54}$$

where E_C = Coulombic energy coefficient of the semi-empirical mass formula, E_A = asymmetry energy coefficient of the semi-empirical mass formula and X_E = proposed lepton mass generator = 294.8183 and $n = 0, 1, 2$.

If $E_C = 0.769$ MeV and $E_A = 23.86$ MeV obtained charged lepton masses are shown in the following Table 1. It is known that these two coefficients plays a vital role in nuclear stability. It is well known that in weak decay for getting stability neutron in an unstable nuclide emits electron. If our study is focused on why and how a charged lepton is coming out from the nucleus this idea can be adapted. For any model data fitting is the first successful step in its implementation in the actual field.

3.6 Role of X_E in estimating the nuclear size R_0

Compton wave length of nucleon is

$$\frac{\hbar}{m_n c} = 2.1016{\times}10^{-16} \text{ meter}, \tag{55}$$

where m_n is the average mass of nucleon = 938.92 MeV. It is noticed that

$$R_0 \cong (X_E)^{\frac{1}{3}} \frac{\hbar}{m_n c} = 1.399{\times}10^{-15} \text{ meter}. \tag{56}$$

This is very close to the estimated nuclear characteristic size. With reference to Rutherford's alpha scattering experiments size of a nucleus that contains A nucleons can be given as

$$R_A \cong (AX_E)^{\frac{1}{3}} \frac{\hbar}{m_n c}. \tag{57}$$

Hence ratio of "nuclear volume" and "A nucleons Compton volume" = X_E.

4 Relations between energy coefficients of the semi-empirical mass formula

We know that the best energy coefficients of the semi-empirical mass formula [12–14] are, Coulombic energy coefficient $E_C = 0.71$ MeV, volume energy coefficient $E_V = 15.78$ MeV, surface energy coefficient $E_S = 18.34$ MeV, asymmetry energy coefficient $E_A = 23.21$ MeV and pairing energy coefficient $E_{EO} = 12.0$ MeV. The 4 major energy coefficients of the semi-empirical mass formula lies in between 11.97 MeV and $2{\times}11.97 = 23.94$ MeV. Really this is a very interesting case. If one proceeds further for analyzing this strange observation possibly role of "strong coupling constant" or "strong interaction mass generator" can be understood in the "nuclear mass generation". Thus unification of "gravitation" with "nuclear physics" may be possible. Authors proposal may be given a chance. See the following Table 2. In this context it is assumed that

$$\frac{M_{Sf} c^2}{E_C} \cong \frac{1}{\alpha} \quad \text{and} \quad E_C \cong \alpha M_{Sf} c^2 = 0.769 \text{ MeV}. \tag{58}$$

From equations (23, 46, 53 and 58) empirically it is noticed that

$$E_V \cong M_n c^2 + \left(X_E^{\frac{1}{3}} - 1\right) E_C \cong 16.32 \text{ MeV}, \tag{59}$$

$$E_S \cong M_n c^2 + \left(X_E^{\frac{1}{3}} + \sqrt{X_S}\right) E_C \cong 19.37 \text{ MeV}, \tag{60}$$

$$E_A \cong M_n c^2 + \left(X_E^{\frac{1}{3}} + X_S\right) E_C \cong 23.86 \text{ MeV} \cong 2M_n c^2, \tag{61}$$

$$E_A - E_S \cong \left(X_S - \sqrt{X_S}\right) E_C, \tag{62}$$

$$E_{EO} \cong M_n c^2 \cong 11.97 \text{ MeV}. \tag{63}$$

It is also noticed that

$$X_E \cong \frac{E_S}{E_C} \sqrt{\frac{M_{Sf} c^2}{E_C}} \cong \frac{E_S}{E_C} \sqrt{\frac{1}{\alpha}}. \tag{64}$$

This is another interesting guess. This successfully implements the new number X_E. It is observed that proposed E_V-existing $E_V = 16.32 - 15.78 = 0.54$ MeV $\approx E_T = 0.511$ MeV. Proposed E_S — existing $E_S = 19.37 - 18.34 = 1.03$ MeV $\approx 2E_T = 2{\times}0.511$ MeV. Proposed E_A-existing $E_A = 23.86 - 23.21 = 0.65$ MeV $\approx E_T = 0.511$ MeV.

Please note that asymmetry energy coefficient is matching with twice of $M_n c^2 = 23.94$ MeV. This is very interesting. If proposed ideas has no significance here why and how it is happening like this? This data coincidence indicates that proposed scheme of energy coefficients can be applied in the

Z	A	Obtained Be, MeV	Be, MeV [13, 14]
8	16	121.6	118.13, 128.57
20	44	382.7	377.66, 382.78
28	62	543.7	538.85, 544.41
50	118	1003.4	1000.22, 1004.74
82	208	1620.6	1618.41, 1635.36
108	292	2089.6	2082.53, 2089.48

Table 2: Fitting of nuclear binding energy with proposed coefficients.

semi-empirical formula for understanding the significance of proposed 105.383 MeV and $X_S = 8.803486$ in the context of strong interaction. The semi-empirical mass formula is

$$Be = AE_V - A^{\frac{2}{3}}E_S - \frac{Z^2}{A^{\frac{1}{3}}}E_C - \frac{(A-2Z)^2}{A}E_A \pm \sqrt{\frac{1}{A}}E_{EO}. \quad (65)$$

Here $E_V = 16.32$ MeV, $E_S = 19.37$ MeV, $E_C = 0.769$ MeV, $E_A = 23.86$ MeV and $E_{EO} = 11.97$ MeV can be considered as the unified energy coefficients of the semi-empirical formula [13, 14] where Coulombic energy term contains $[Z]^2$.

If one wants to retain $[Z(Z-1)]$ energy coefficients can be fine tuned in the following way

$$E_{EO} \cong M_n c^2 \cong 11.97 \text{ MeV}, \quad (66)$$

$$E_A \cong 2M_n c^2 \cong 23.94 \text{ MeV}, \quad (67)$$

$$\frac{E_A}{E_V} \cong \sqrt{\alpha X_E} \text{ and } E_V \cong 16.322 \text{ MeV}, \quad (68)$$

$$E_V + E_S \cong E_A + E_{EO} \cong 3E_{EO}, \quad (69)$$

$$E_S \cong 3E_{EO} - E_V \cong 35.91 - 16.322 \cong 19.59 \text{ MeV}. \quad (70)$$

Alternatively

$$E_V \cong \left(\frac{3E_{EO}}{2}\right) - (\alpha X_E)E_C \cong 16.30 \text{ MeV}, \quad (71)$$

$$E_S \cong \left(\frac{3E_{EO}}{2}\right) + (\alpha X_E)E_C \cong 19.61 \text{ MeV}, \quad (72)$$

with $E_V = 16.30$ MeV, $E_S = 19.61$ MeV and with $E_V = 16.32$ MeV, $E_S = 19.59$ MeV,

- for $Z = 26$ and $A = 56$, $Be = 489.87$ MeV and 491.40 MeV,
- for $Z = 50$ and $A = 118$, $Be = 1002.88$ MeV and 1005.96 MeV,
- for $Z = 79$ and $A = 197$, $Be = 1547.96$ MeV and 1552.97 MeV,
- for $Z = 92$ and $A = 238$, $Be = 1794.87$ MeV and 1800.87 MeV.

Taking mean values of E_V and E_S, energy coefficients can be given as $E_V = 16.31$ MeV, $E_S = 19.60$ MeV, $E_C = 0.769$ MeV, $E_A = 23.94$ MeV and $E_{EO} = 11.97$ MeV.

4.1 Nuclear binding energy with two terms and one energy constant 0.769 MeV

An empirical method is proposed here for fitting the nuclear binding energy. This method contains two terms. For these two terms, Coulombic energy constant $E_C = 0.769$ MeV is applied. In this method the important point is at first for any Z its stable mass number A_S has to be estimated. Strong interaction mass generator X_S plays a crucial role in this method. For any Z error in binding energy is very small near the stable isotope A_S and increasing above and below A_S. Unifying 5 terms having 5 energy constants into two terms with one energy constant which are related with strong interaction mass generator is not a simple task. Authors proposal can be given a chance.

This method is applicable for light atoms also. For light atoms, when $A = 2Z$, obtained binding energy is very close to the actual value. For $Z = 2$ and $A = 4$ is 28.86 MeV, $Z = 4$, $A = 8$ is 59.57 MeV, $Z = 6$, $A = 12$ is 92.63 MeV $Z = 7$, $A = 14$ is 114.0 MeV, $Z = 8$ $A = 16$ is 127.14 MeV, $Z = 9$, $A = 19$ is 149.72 MeV and $Z = 10$, $A = 20$ is 155.06 MeV. For very light odd elements error is due to estimation of their stable mass numbers

$$T_1 = \left[(A+1)\left(1 + \frac{2Z}{A_S}\right)\right] \ln\left[(A+1)X_S\right] E_C. \quad (73)$$

Stable isotope of any Z can be estimated as

$$A_S \cong 2Z + \frac{Z^2}{S_f} \cong 2Z + \frac{Z^2}{155.72}. \quad (74)$$

Here S_f can be called as the nuclear stability factor. It can be given as

$$S_f \cong \frac{E_A}{E_C}\sqrt{\frac{E_S}{E_C}} \cong 155.72 \cong 2X_S^2 \cong 155.00. \quad (75)$$

After rounding off for even Z values, if obtained A_S is odd consider $A_S + 1$, for odd Z values if obtained A_S is even, consider $A_S - 1$. For very light odd elements this seems to be not fitting.

Term T_1 indicates the factors for increase in binding energy. Another observation is $[(A+1)X_S]$. This factor plays a key role in the saturation of the binding energy. It is observed that for any Z at its stable isotope A_S

$$T_1 \cong [A_S + 2Z + (1 \text{ or } 2)] \ln\left[(A_S + 1)X_S\right] E_C. \quad (76)$$

The basic question is that how to extrapolate from the stable isotope A_S of any Z to above and below its stable and unstable isotopes? Authors are working in this direction also

$$T_2 \cong \left[\frac{A^2 + \left(fZ^2\right)}{X_S^2}\right] E_C, \quad (77)$$

where

$$f \cong 1 + \frac{2Z}{A_S} \cong \text{ a factor} \leqslant 2. \quad (78)$$

Z	A_S	Obtained Be, MeV
2	4	28.9
8	16	127.1
20	44	368.4
26	56	481.6
44	100	856.2
68	166	1347.1
83	209	1623.5
92	238	1775.5

Table 3: Fitting of nuclear binding energy with two terms and one energy constant.

Term T_2 indicates the factors for decrease in binding energy. Both of these terms has to be analyzed at fundamental level. T_1 and T_2 indicates the importance of the number $X_S = 8.8034856$ in strong interaction mass generation

$$Be = T_1 - T_2. \tag{79}$$

Whether this is the total binding energy that includes shell effects or liquid drop energy has to be decided with observations and analysis. This method has to be analyzed and extended for isotopes above and below the stable mass number A_S of any Z value. With reference to A_S and by considering shell effects error in finding the first term can be eliminated. In the second term by selecting a suitable expression for f error can be minimized. The advantage of this method is that number of energy constants can be minimized. See the following Table 3.

5 Rest mass of nucleon

Let m_nc^2 = rest mass of nucleon. Semi-empirically it is observed that

$$m_nc^2 \cong \ln\left(M_nc^2\frac{8\pi\epsilon_0R_0}{e^2}\right)^2\sqrt{\frac{R_S}{a}}\,M_nc^2. \tag{80}$$

Here a is the Compton length of M_{Sf} and R_S is the black hole radius of M_{Sf} and is given by

$$R_S = \frac{2G_SM_{Sf}}{c^2} = 2.9023\times10^{-13}\text{ meter}, \tag{81}$$

$$m_nc^2 \cong \ln\left(\frac{8\pi\epsilon_0R_0M_nc^2}{e^2}\right)^2\sqrt{\frac{2G_SM_{Sf}^2}{\hbar c}}\,M_nc^2. \tag{82}$$

From equation (48)

$$m_nc^2 \cong \ln\left(\frac{M_nc^2}{m_ec^2}\right)^2\sqrt{\frac{2G_SM_{Sf}^2}{\hbar c}}\,M_nc^2. \tag{83}$$

5.1 Nucleon stability relation

If it is assumed that

$$A_S \cong 2Z + \frac{Z^2}{155.00} \cong 2Z + \frac{Z^2}{2X_S^2}, \tag{84}$$

significance of $2X_S^2$ can be given as

$$2X_S^2 \cong \frac{2G_SM_{Sf}^2}{\hbar c} \cong \frac{R_S}{a} \cong 155.00 \tag{85}$$

Hence

$$A_S \cong 2Z + \frac{Z^2}{S_f} \cong 2Z + \left(\frac{a}{R_S}\right)Z^2. \tag{86}$$

For example, if $Z = 47$, $A_S = 108.25$, $Z = 82$, $A_S = 207.38$ and $Z = 92$, $A_S = 238.6$. This clearly indicates the beautiful role of $2X_S^2$ in nuclear stability.

5.2 Excited levels of nucleon

From quantum mechanics quantized angular momentum is given by $\sqrt{n(n+1)}.\hbar$ where $n = 0, 1, 2\ldots$ Some how if $\hbar$ goes under a "square root" like the planck energy, $M_Pc^2 = \sqrt{\frac{\hbar c^5}{G_C}}$ as a ground state energy level in a heuristic way its massive excited levels are given by [6]

$$\left(M_Pc^2\right)_I = [n(n+1)]^{\frac{1}{4}}\sqrt{\frac{\hbar c^5}{G_C}}. \tag{87}$$

Here $n = 0, 1, 2, 3\ldots$ and $I = n(n+1)$. Keeping this idea in view it is assumed that "if m_0c^2 is the rest energy of a particle then its massive excited levels are given by

$$mc^2 = [n(n+1)]^{\frac{1}{4}}\,m_0c^2 \tag{88}$$

and each excited state can be seen as a new massive particle". The surprising observation is that in particle physics excited massive states are following two types of discrete levels. They are

$$[n(n+1)]^{\frac{1}{4}}\,m_0c^2 \text{ and } \left[\frac{n(n+1)}{2}\right]^{\frac{1}{4}}m_0c^2. \tag{89}$$

Presently understood "Regge trajectory" of some of the baryons and mesons are fitted in this way. These levels can be called as Fine rotational levels. If the proposed idea is correct nucleon must show excited levels as

$$\left(m_nc^2\right)_I = [I]^{\frac{1}{4}}\,939 \text{ and } \left(m_nc^2\right)_{\frac{I}{2}} = \left[\frac{I}{2}\right]^{\frac{1}{4}}939, \tag{90}$$

where $I = n(n+1)$ and n =1, 2, 3, ...

At $I = 2$, 1117 MeV, $\frac{I}{2} = 3$, 1236 MeV, at $I = \frac{I}{2} = 6$, 1470 MeV, at $\frac{I}{2} = 10$, 1670 MeV, $I = 12$, 1748 MeV levels are obtained. This is a great coincidence and is a true reflection of the correctness of the proposed assumptions. Hence the proposed ideas can be given a chance in "final grand unified physics".

Conclusions

Nucleus has strong nuclear gravitational mechanism. Some how electron plays a crucial role in its structural formation. Just like quark masses $M_{Sf}c^2$ can be considered as a strongly

interacting "confined" fermion. Whether G_S is really existing or an equivalent value it plays a heuristic role in understanding the experimental things and can be considered for further analysis. Based on the proposed data fitting results existence of the proposed strong interaction fermion $M_{Sf}c^2$ and the strong interaction mass generator $X_S = 8.8034856$ can be confirmed. 0.769 MeV can be considered as the unified Coulombic energy coefficient.

Two most important and interesting observations are as follows

$$\alpha X_E \cong \sqrt{\ln \sqrt{\frac{4\pi\epsilon_0 G_S M_{Sf}^2}{e^2}}} \cong 2.153. \qquad (91)$$

This expression clearly demonstrates the hidden existence of $M_{Sf}c^2$ and G_S in nuclear and particle physics. In our paper [6] it is assumed that there exists a strongly interacting fermion 11450 MeV which plays a crucial role in estimating quark-gluon masses. Empirically it is noticed that

$$(11450)^{\frac{14}{30}}\,(105.38)^{\frac{16}{30}} \cong 939.54 \text{ MeV}. \qquad (92)$$

This is very close to the neutron mass. Since both are integral charged particles and giving importance to the charged proton mass it can be written as

$$\left(\frac{11450}{105.38}\right)^{\frac{14}{30}}(105.38) \cong 939.54 \text{ MeV}, \qquad (93)$$

where

$$\left(\frac{11450}{105.38}\right)^{\frac{14}{30}} \cong 8.9157 \cong X_S\,. \qquad (94)$$

This number is very close to the proposed strong interaction mass generator X_S. It is noticed that $\frac{14}{30} \cong 0.4666$ and $\frac{16}{30} \cong 0.5333$. Comparing $\left(\frac{14}{30}\right)$ with $\left(\frac{1}{\alpha X_E}\right)$ one can see the significance of (αX_E) in deciding the mass of proton.

Even though this is an unconventional paper number of inputs are only two and they are assumed $M_{Sf}c^2$ and strong nuclear gravitational constant G_S. The main advantage of this paper is that there is no need to go beyond 4 dimensions. Authors humbly request the world science community to kindly look into these new and heuristic ideas for further analysis and development.

Acknowledgements

The first author is very much thankful to Prof. S. Lakshminarayana, Department of Nuclear Physics, Andhra University, Visakhapatnam, India, Dr. P. K. Panigrahi, PRL, India and Mr. N. Phani Raju, principal, SSN PG college, Ongole, AP, India for their kind, immense and precious encouragement and guidance at all times. The same author is very much thankful to Dr. Rukmini Mohanta, UoH, India and the organising committee for considering this for poster presentation in DAE-BRNS 2008 HEP Physics symposium, Banaras, India. Finally the first author is very much thankful to his loving brother B. Vamsi Krishna (Software professional) and boyhood friend T. Anand Kumar (software professional) for encouraging, providing technical and financial support.

Submitted on January 26, 2009 / Accepted on February 20, 2010

References

1. Stone R. A. Jr. Quark confinement and force unification. *Progress in Physics*, 2010, v. 2, 19–22.
2. Oldershaw R. L. Hadrons as Kerr-Newman black holes. arXiv: astro-ph/0701006.
3. Raut U. and Sinha K. P. Strong gravity and the Yukawa field. *International Journal of Theoretical Physics*, 1981, v 20, no. 1, 69–77.
4. Perng J. J. Strong gravitation and elementary particles. *Nuovo Cimento Lettere*, Serie 2, 1978, v. 23, 552–554.
5. Salam A. and Sivaram C. Strong gravity approach to QCD and confinement. *Mod. Phys. Lett. A*, 1993, v.8, no. 4, 321–326.
6. Seshavatharam U. V. S. and Lakshminarayana S. Super symmetry in strong and weak interactions. *IJMPE*, 2010, v. 19, no. 2, 263–280.
7. Seshavatharam U. V. S. Physics of rotating and expanding black hole universe. *Progress in Physics*, 2010, v. 2, 7–14.
8. Glasman C. Precision measurements of alphas at HERA. arXiv: hep-ex/0506035.
9. Nambu Y. *Prog. Theor. Phys.*, 1952, v. 7, 595.
10. Quigg C. The electroweak theory. arXiv: hep-ph/0204104.
11. Koschmieder E. L. The mass and spin of the mesons, baryons and leptons. arXiv: physics/0408070.
12. Roy Chowdhury P. et al. Modified Bethe-Weizsacker mass formula with isotonic shift and new driplines. arXiv: nucl-th/0405080.
13. Myers W. D. et al. Table of nuclear masses according to the 1994 Thomas-Fermi model. http://nsdssd.lbl.gov
14. Audi G. and Wapstra A. H. The 1995 update to the atomic mass evaluation. *Nuclear Physics A*, 1995, v. 595, no. 4, 409–480; arXiv: 0903.5141.

SPECIAL REPORT

Relativity in Combinatorial Gravitational Fields

Linfan Mao
Chinese Academy of Mathematics and System Science,
Beijing 100080, P. R. China
E-mail: maolinfan@163.com

A combinatorial spacetime $(\mathscr{C}_G|\bar{t})$ is a smoothly combinatorial manifold $\mathscr{C}$ underlying a graph G evolving on a time vector $\bar{t}$. As we known, Einstein's general relativity is suitable for use only in one spacetime. *What is its disguise in a combinatorial spacetime*? Applying combinatorial Riemannian geometry enables us to present a combinatorial spacetime model for the Universe and suggest a generalized Einstein gravitational equation in such model. For finding its solutions, a generalized relativity principle, called *projective principle* is proposed, i.e., *a physics law in a combinatorial spacetime is invariant under a projection on its a subspace* and then a spherically symmetric multi-solutions of generalized Einstein gravitational equations in vacuum or charged body are found. We also consider the geometrical structure in such solutions with physical formations, and conclude that an ultimate theory for the Universe maybe established if all such spacetimes in $\mathbf{R}^3$. Otherwise, our theory is only an approximate theory and endless forever.

1 Combinatorial spacetimes

The multi-laterality of our Universe implies the best spacetime model should be a combinatorial one. However, classical spacetimes are all in solitude. For example, the Newton spacetime $(\mathbf{R}^3|t)$ is a geometrical space $(x_1, x_2, x_3) \in \mathbf{R}^3$ with an absolute time $t \in \mathbf{R}^+$. With his deep insight in physical laws, Einstein was aware of that all reference frames were established by human beings, which made him realized that *a physics law is invariant in any reference frame*. Whence, the Einstein spacetime is $(\mathbf{R}^3|t) \cong \mathbf{R}^4$ with $t \in \mathbf{R}^+$, i.e., a warped spacetime generating gravitation. In this kind of spacetime, its line element is

$$ds^2 = \sum_{0\leqslant\mu,\nu\leqslant 3} g_{\mu\nu}(\overline{x})dx_\mu dx_\nu\,,$$

where $g_{\mu\nu}$, $0 \leqslant \mu, \nu \leqslant 3$ are Riemannian metrics with local flat, i.e., the Minkowskian spacetime

$$ds^2 = -c^2dt^2 + dx_1^2 + dx_2^2 + dx_3^2\,,$$

where c is the light speed. *Wether the spacetime of Universe is isolated*? In fact, there are no justifications for Newton's or Einstein's choice but only dependent on mankind's perception with the geometry of visible, i.e., the spherical geometry(see [1–4] for details).

Certainly, different standpoints had unilaterally brought about particular behaviors of the Universe such as those of electricity, magnetism, thermal, optics... in physics and their combinations, for example, the thermodynamics, electromagnetism, ..., etc. But the true colours of the Universe should be hybrid, not homogeneous or unilateral. They should be a union or a combination of all these features underlying a combinatorial structure. That is the origin of combinatorial spacetime established on smoothly combinatorial manifolds following ([5–9]), a particular case of Smarandache multi-space ([10–11]) underlying a connected graph.

Definition 1.1 *Let $n_i, 1 \leqslant i \leqslant m$ be positive integers. A combinatorial Euclidean space is a combinatorial system $\mathscr{C}_G$ of Euclidean spaces $\mathbf{R}^{n_1}$, $\mathbf{R}^{n_2}$, $\cdots$, $\mathbf{R}^{n_m}$ underlying a connected graph G defined by*

$$V(G) = \{\mathbf{R}^{n_1}, \mathbf{R}^{n_2}, \cdots, \mathbf{R}^{n_m}\}\,,$$

$$E(G) = \{\,(\mathbf{R}^{n_i}, \mathbf{R}^{n_j}) \mid \mathbf{R}^{n_i} \bigcap \mathbf{R}^{n_j} \neq \emptyset, 1 \leqslant i, j \leqslant m\}\,,$$

denoted by $\mathscr{E}_G(n_1, \cdots, n_m)$ and abbreviated to $\mathscr{E}_G(r)$ if $n_1 = \cdots = n_m = r$.

A *combinatorial fan-space* $\widetilde{\mathbf{R}}(n_1, \cdots, n_m)$ is a combinatorial Euclidean space $\mathscr{E}_{K_m}(n_1, \cdots, n_m)$ of $\mathbf{R}^{n_1}$, $\mathbf{R}^{n_2}$, $\cdots$, $\mathbf{R}^{n_m}$ such that for any integers i, j, $1 \leqslant i \neq j \leqslant m$, $\mathbf{R}^{n_i} \bigcap \mathbf{R}^{n_j} = \bigcap_{k=1}^{m} \mathbf{R}^{n_k}$, which is in fact a *p-brane* with $p = \dim \bigcap_{k=1}^{m} \mathbf{R}^{n_k}$ in *string theory* ([12]), seeing Fig. 1.1 for details.

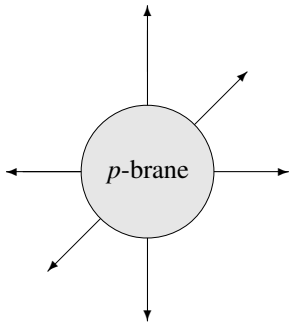

Fig. 1.1

For $\forall p \in \widetilde{\mathbf{R}}(n_1, \cdots, n_m)$ we can present it by an $m \times n_m$

coordinate matrix $[\overline{x}]$ following with $x_{il} = \dfrac{x_l}{m}$ for $1 \leqslant i \leqslant m, 1 \leqslant l \leqslant \widehat{m}$,

$$[\overline{x}] = \begin{bmatrix} x_{11} & \cdots & x_{1\widehat{m}} & \cdots & x_{1n_1} & \cdots & 0 \\ x_{21} & \cdots & x_{2\widehat{m}} & \cdots & x_{2n_2} & \cdots & 0 \\ \cdots & \cdots & \cdots & \cdots & \cdots & \cdots & \cdots \\ x_{m1} & \cdots & x_{m\widehat{m}} & \cdots & \cdots & \cdots & x_{mn_m} \end{bmatrix}.$$

A topological combinatorial manifold $\widetilde{M}$ is defined in the next.

Definition 1.2 *For a given integer sequence $0 < n_1 < n_2 < \cdots < n_m$, $m \geqslant 1$, a topological combinatorial manifold $\widetilde{M}$ is a Hausdorff space such that for any point $p \in \widetilde{M}$, there is a local chart (U_p, φ_p) of p, i.e., an open neighborhood U_p of p in $\widetilde{M}$ and a homeomorphism $\varphi_p : U_p \to \widetilde{\mathbf{R}}(n_1(p), \cdots, n_{s(p)}(p))$ with*

$$\{n_1(p), \cdots, n_{s(p)}(p)\} \subseteq \{n_1, \cdots, n_m\},$$
$$\bigcup_{p\in\widetilde{M}} \{n_1(p), \cdots, n_{s(p)}(p)\} = \{n_1, \cdots, n_m\},$$

denoted by $\widetilde{M}(n_1, n_2, \cdots, n_m)$ or $\widetilde{M}$ on the context and

$$\widetilde{\mathcal{A}} = \{(U_p, \varphi_p) | p \in \widetilde{M}(n_1, n_2, \cdots, n_m))\}$$

an atlas on $\widetilde{M}(n_1, n_2, \cdots, n_m)$.

A topological combinatorial manifold $\widetilde{M}$ is finite if it is just combined by finite manifolds without one manifold contained in the union of others.

For a finite combinatorial manifold $\widetilde{M}$ consisting of manifolds M_i, $1 \leqslant i \leqslant m$, we can construct a vertex-edge labeled graph $G^L[\widetilde{M}]$ defined by

$$V(G^L[\widetilde{M}]) = \{M_1, M_2, \cdots, M_m\},$$
$$E(G^L[\widetilde{M}) = \{ (M_i, M_j) \mid M_i \bigcap M_j \neq \emptyset, 1 \leqslant i, j \leqslant n\}$$

with a labeling mapping

$$\Theta : V(G^L[\widetilde{M}]) \bigcup E(G^L[\widetilde{M}]) \to \mathbf{Z}^+$$

determined by

$$\Theta(M_i) = \dim M_i, \quad \Theta(M_i, M_j) = \dim M_i \bigcap M_j$$

for integers $1 \leqslant i, j \leqslant m$, which is inherent structure of combinatorial manifolds. A differentiable combinatorial manifold is defined by endowing differential structure on a topological combinatorial manifold following.

Definition 1.3 *For a given integer sequence $1 \leqslant n_1 < n_2 < \cdots < n_m$, a combinatorial C^h-differential manifold $(\widetilde{M}(n_1, n_2 \cdots, n_m); \widetilde{\mathcal{A}})$ is a finite combinatorial manifold $\widetilde{M}(n_1, \cdots, n_m)$, $\widetilde{M}(n_1, \cdots, n_m) = \bigcup_{i\in I} U_i$, endowed with an atlas $\widetilde{\mathcal{A}} = \{(U_\alpha; \varphi_\alpha) | \alpha \in I\}$ on $\widetilde{M}(n_1, \cdots, n_m)$ for an integer $h, h \geqslant 1$ with conditions following hold.*

(1) *$\{U_\alpha; \alpha \in I\}$ is an open covering of $\widetilde{M}(n_1, n_2, \cdots, n_m)$.*

(2) *For $\forall \alpha, \beta \in I$, local charts $(U_\alpha; \varphi_\alpha)$ and $(U_\beta; \varphi_\beta)$ are equivalent, i.e., $U_\alpha \bigcap U_\beta = \emptyset$ or $U_\alpha \bigcap U_\beta \neq \emptyset$ but the overlap maps*

$$\varphi_\alpha\varphi_\beta^{-1} : \varphi_\beta(U_\alpha \bigcap U_\beta) \to \varphi_\beta(U_\beta),$$
$$\varphi_\beta\varphi_\alpha^{-1} : \varphi_\alpha(U_\alpha \bigcap U_\beta) \to \varphi_\alpha(U_\alpha)$$

both are C^h-mappings, such as those shown in Fig. 1.2 following.

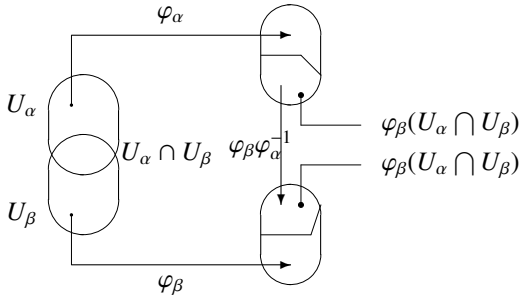

Fig. 1.2

(3) *$\widetilde{\mathcal{A}}$ is maximal, i.e., if $(U; \varphi)$ is a local chart of $\widetilde{M}(n_1, \cdots, n_m)$ equivalent with one of local charts in $\widetilde{\mathcal{A}}$, then $(U; \varphi) \in \widetilde{\mathcal{A}}$.*

A finite combinatorial manifold $\widetilde{M}(n_1, \cdots, n_m)$ is *smooth* if it is endowed with a C^∞-differential structure. Now we are in the place introducing combinatorial spacetime.

Definition 1.4 *A combinatorial spacetime $(\mathscr{C}_G|\bar{t})$ is a smooth combinatorial manifold $\mathscr{C}$ underlying a graph G evolving on a time vector $\bar{t}$, i.e., a geometrical space $\mathscr{C}$ with a time system $\bar{t}$ such that $(\overline{x}|\bar{t})$ is a particle's position at a time $\bar{t}$ for $\overline{x} \in \mathscr{C}$.*

The existence of combinatorial spacetime in the Universe is a wide-ranging, even if in the society science. By the explaining in the reference [13], there are four-level hierarchy of parallel universes analyzed by knowledge of mankind already known, such as those of *Hubble volumes, chaotic inflation, wavefunction* and *mathematical equations*, etc. Each level is allowed progressively greater diversity.

Question 1.5 *How to deal behaviors of these different combinatorial spacetimes definitely with mathematics, not only qualitatively?*

Recently, many researchers work for brane-world cosmology, particular for the case of dimensional $\leqslant 6$, such as those researches in references [14–18] and [3] etc. This brane-world model was also applied in [19] for explaining a black hole model for the Universe by combination. Notice

that the underlying combinatorial structure of brane-world cosmological model is essentially a tree for simplicity.

Now we have established a differential geometry on combinatorial manifolds in references [5–9], which provides us with a mathematical tool for determining the behavior of combinatorial spacetimes. The main purpose of this paper is to apply it to combinatorial gravitational fields combining with spacetime's characters, present a generalized relativity in combinatorial fields and use this principle to solve the gravitational field equations. We also discuss the consistency of this combinatorial model for the Universe with some observing data such as the cosmic microwave background (CMB) radiation by WMAP in 2003.

2 Curvature tensor on combinatorial manifolds

Applying combinatorial spacetimes to that of gravitational field needs us to introduce curvature tensor for measuring the warping of combinatorial manifolds. In this section, we explain conceptions with results appeared in references [5–8], which are applied in this paper.

First, the structure of tangent and cotangent spaces $T_p\widetilde{M}$, $T_p^*\widetilde{M}$ at any point $p \in \widetilde{M}$ in a smoothly combinatorial manifold $\widetilde{M}$ is similar to that of differentiable manifold. It has been shown in [5] that $\dim T_p\widetilde{M}(n_1, \cdots, n_m) = \widehat{s}(p) + \sum\limits_{i=1}^{s(p)} (n_i - \widehat{s}(p))$ and $\dim T_p^*\widetilde{M}(n_1, n_2, \cdots, n_m) = \widehat{s}(p) + \sum\limits_{i=1}^{s(p)} (n_i - \widehat{s}(p))$ with a basis

$$\left\{\frac{\partial}{\partial x^{i_0 j}}|_p | 1 \leqslant j \leqslant \widehat{s}(p)\right\} \bigcup \left(\bigcup_{i=1}^{s(p)} \left\{\frac{\partial}{\partial x^{ij}}|_p \mid \widehat{s}(p)+1 \leqslant j \leqslant n_i\right\}\right),$$

$$\{dx^{i_0 j}|_p | 1 \leqslant j \leqslant \widehat{s}(p)\} \bigcup \left(\bigcup_{i=1}^{s(p)} \{dx^{ij}|_p \mid \widehat{s}(p)+1 \leqslant j \leqslant n_i\}\right)$$

for any integer $i_0, 1 \leqslant i_0 \leqslant s(p)$, respectively. These mathematical structures enable us to construct tensors, connections on tensors and curvature tensors on smoothly combinatorial manifolds.

Definition 2.1 *Let $\widetilde{M}$ be a smoothly combinatorial manifold, $p \in \widetilde{M}$. A tensor of type (r, s) at the point p on $\widetilde{M}$ is an $(r+s)$-multilinear function τ,*

$$\tau : \underbrace{T_p^*\widetilde{M} \times \cdots \times T_p^*\widetilde{M}}_{r} \times \underbrace{T_p\widetilde{M} \times \cdots \times T_p\widetilde{M}}_{s} \to \mathbf{R}.$$

Let $\widetilde{M}(n_1, \cdots, n_m)$ be a smoothly combinatorial manifold. Denoted by $T_s^r(p, \widetilde{M})$ all tensors of type (r, s) at a point p of $\widetilde{M}(n_1, \cdots, n_m)$. Then for $\forall p \in \widetilde{M}(n_1, \cdots, n_m)$, we have known that

$$T_s^r(p, \widetilde{M}) = \underbrace{T_p\widetilde{M} \otimes \cdots \otimes T_p\widetilde{M}}_{r} \otimes \underbrace{T_p^*\widetilde{M} \otimes \cdots \otimes T_p^*\widetilde{M}}_{s},$$

where

$$T_p\widetilde{M} = T_p\widetilde{M}(n_1, \cdots, n_m),$$
$$T_p^*\widetilde{M} = T_p^*\widetilde{M}(n_1, \cdots, n_m),$$

particularly,

$$\dim T_s^r(p, \widetilde{M}) = \left(\widehat{s}(p) + \sum_{i=1}^{s(p)} (n_i - \widehat{s}(p))\right)^{r+s}$$

by argumentation in [5–7].

A connection on tensors of a smooth combinatorial manifold is defined by

Definition 2.2 *Let $\widetilde{M}$ be a smooth combinatorial manifold. A connection on tensors of $\widetilde{M}$ is a mapping $\widetilde{D} : \mathscr{X}(\widetilde{M}) \times T_s^r\widetilde{M} \to T_s^r\widetilde{M}$ with $\widetilde{D}_X\tau = \widetilde{D}(X, \tau)$ such that for $\forall X, Y \in \mathscr{X}\widetilde{M}$, $\tau, \pi \in T_s^r(\widetilde{M}), \lambda \in \mathbf{R}$ and $f \in C^\infty(\widetilde{M})$,*

(1) $\widetilde{D}_{X+fY}\tau = \widetilde{D}_X\tau + f\widetilde{D}_Y\tau$ and $\widetilde{D}_X(\tau + \lambda\pi) = \widetilde{D}_X\tau + \lambda\widetilde{D}_X\pi$;

(2) $\widetilde{D}_X(\tau \otimes \pi) = \widetilde{D}_X\tau \otimes \pi + \sigma \otimes \widetilde{D}_X\pi$;

(3) *for any contraction C on $T_s^r(\widetilde{M})$,*

$$\widetilde{D}_X(C(\tau)) = C(\widetilde{D}_X\tau).$$

For a smooth combinatorial manifold $\widetilde{M}$, we have shown in [5] that there always exists a connection $\widetilde{D}$ on $\widetilde{M}$ with coefficients $\Gamma^{\kappa\lambda}_{(\sigma\varsigma)(\mu\nu)}$ determined by

$$\widetilde{D}_{\frac{\partial}{\partial x^{\mu\nu}}} \frac{\partial}{\partial x^{\sigma\varsigma}} = \Gamma^{\kappa\lambda}_{(\sigma\varsigma)(\mu\nu)} \frac{\partial}{\partial x^{\sigma\varsigma}}.$$

A combinatorially connection space $(\widetilde{M}, \widetilde{D})$ is a smooth combinatorial manifold $\widetilde{M}$ with a connection $\widetilde{D}$.

Definition 2.3 *Let $\widetilde{M}$ be a smoothly combinatorial manifold and $g \in A^2(\widetilde{M}) = \bigcup\limits_{p \in \widetilde{M}} T_2^0(p, \widetilde{M})$. If g is symmetrical and positive, then $\widetilde{M}$ is called a combinatorially Riemannian manifold, denoted by $(\widetilde{M}, g)$. In this case, if there is also a connection $\widetilde{D}$ on $(\widetilde{M}, g)$ with equality following hold*

$$Z(g(X, Y)) = g(\widetilde{D}_Z, Y) + g(X, \widetilde{D}_Z Y),$$

then $\widetilde{M}$ is called a combinatorially Riemannian geometry, denoted by $(\widetilde{M}, g, \widetilde{D})$.

It has been proved in [5] and [7] that there exists a unique connection $\widetilde{D}$ on $(\widetilde{M}, g)$ such that $(\widetilde{M}, g, \widetilde{D})$ is a combinatorially Riemannian geometry.

Definition 2.4 *Let $(\widetilde{M}, \widetilde{D})$ be a combinatorially connection space. For $\forall X, Y \in \mathscr{X}(\widetilde{M})$, a combinatorially curvature operator $\widetilde{\mathcal{R}}(X, Y) : \mathscr{X}(\widetilde{M}) \to \mathscr{X}(\widetilde{M})$ is defined by*

$$\widetilde{\mathcal{R}}(X, Y)Z = \widetilde{D}_X\widetilde{D}_Y Z - \widetilde{D}_Y\widetilde{D}_X Z - \widetilde{D}_{[X,Y]}Z$$

for $\forall Z \in \mathscr{X}(\widetilde{M})$.

Definition 2.5 *Let $(\widetilde{M}, \widetilde{D})$ be a combinatorially connection space. For $\forall X, Y, Z \in \mathscr{X}(\widetilde{M})$, a linear multi-mapping $\widetilde{\mathcal{R}} : \mathscr{X}(\widetilde{M}) \times \mathscr{X}(\widetilde{M}) \times \mathscr{X}(\widetilde{M}) \to \mathscr{X}(\widetilde{M})$ determined by*

$$\widetilde{\mathcal{R}}(Z, X, Y) = \widetilde{\mathcal{R}}(X, Y)Z$$

is said a curvature tensor of type $(1, 3)$ *on* $(\widetilde{M}, \widetilde{D})$.

Calculation in [7] shows that for $\forall p \in \widetilde{M}$ with a local chart $(U_p; [\varphi_p])$,

$$\widetilde{\mathcal{R}} = \widetilde{\mathcal{R}}^{\eta\theta}_{(\sigma\varsigma)(\mu\nu)(\kappa\lambda)} dx^{\sigma\varsigma} \otimes \frac{\partial}{\partial x^{\eta\theta}} \otimes dx^{\mu\nu} \otimes dx^{\kappa\lambda}$$

with

$$\widetilde{\mathcal{R}}^{\eta\theta}_{(\sigma\varsigma)(\mu\nu)(\kappa\lambda)} = \left(\frac{\partial \Gamma^{\eta\theta}_{(\sigma\varsigma)(\kappa\lambda)}}{\partial x^{\mu\nu}} - \frac{\partial \Gamma^{\eta\theta}_{(\sigma\varsigma)(\mu\nu)}}{\partial x^{\kappa\lambda}} + \right.$$
$$\left. + \Gamma^{\vartheta\iota}_{(\sigma\varsigma)(\kappa\lambda)} \Gamma^{\eta\theta}_{(\vartheta\iota)(\mu\nu)} - \Gamma^{\vartheta\iota}_{(\sigma\varsigma)(\mu\nu)} \Gamma^{\eta\theta}_{(\vartheta\iota)(\kappa\lambda)} \right) \frac{\partial}{\partial x^{\vartheta\iota}} ,$$

where $\Gamma^{\sigma\varsigma}_{(\mu\nu)(\kappa\lambda)} \in C^\infty(U_p)$ is determined by

$$\widetilde{D}_{\frac{\partial}{\partial x^{\mu\nu}}} \frac{\partial}{\partial x^{\kappa\lambda}} = \Gamma^{\sigma\varsigma}_{(\kappa\lambda)(\mu\nu)} \frac{\partial}{\partial x^{\sigma\varsigma}} .$$

Particularly, if $(\widetilde{M}, g, \widetilde{D})$ is a combinatorially Riemannian geometry, we know the combinatorially Riemannian curvature tensor in the following.

Definition 2.6 *Let $(\widetilde{M}, g, \widetilde{D})$ be a combinatorially Riemannian manifold. A combinatorially Riemannian curvature tensor $\widetilde{R} : \mathscr{X}(\widetilde{M}) \times \mathscr{X}(\widetilde{M}) \times \mathscr{X}(\widetilde{M}) \times \mathscr{X}(\widetilde{M}) \to C^\infty(\widetilde{M})$ of type* $(0, 4)$ *is defined by*

$$\widetilde{R}(X, Y, Z, W) = g(\widetilde{R}(Z, W)X, Y)$$

for $\forall X, Y, Z, W \in \mathscr{X}(\widetilde{M})$.

Now let $(\widetilde{M}, g, \widetilde{D})$ be a combinatorially Riemannian manifold. For $\forall p \in \widetilde{M}$ with a local chart $(U_p; [\varphi_p])$, we have known that ([8])

$$\widetilde{R} = \widetilde{R}_{(\sigma\varsigma)(\eta\theta)(\mu\nu)(\kappa\lambda)} dx^{\sigma\varsigma} \otimes dx^{\eta\theta} \otimes dx^{\mu\nu} \otimes dx^{\kappa\lambda}$$

with

$$\widetilde{R}_{(\sigma\varsigma)(\eta\theta)(\mu\nu)(\kappa\lambda)} = \frac{1}{2} \left(\frac{\partial^2 g_{(\mu\nu)(\sigma\varsigma)}}{\partial x^{\kappa\lambda} \partial x^{\eta\theta}} + \frac{\partial^2 g_{(\kappa\lambda)(\eta\theta)}}{\partial x^{\mu\nu\nu} \partial x^{\sigma\varsigma}} - \right.$$
$$\left. - \frac{\partial^2 g_{(\mu\nu)(\eta\theta)}}{\partial x^{\kappa\lambda} \partial x^{\sigma\varsigma}} - \frac{\partial^2 g_{(\kappa\lambda)(\sigma\varsigma)}}{\partial x^{\mu\nu} \partial x^{\eta\theta}} \right) + \Gamma^{\vartheta\iota}_{(\mu\nu)(\sigma\varsigma)} \Gamma^{\xi o}_{(\kappa\lambda)(\eta\theta)} g_{(\xi o)(\vartheta\iota)} -$$
$$- \Gamma^{\xi o}_{(\mu\nu)(\eta\theta)} \Gamma_{(\kappa\lambda)(\sigma\varsigma)^{\vartheta\iota}} g_{(\xi o)(\vartheta\iota)} ,$$

where $g_{(\mu\nu)(\kappa\lambda)} = g\left(\frac{\partial}{\partial x^{\mu\nu}}, \frac{\partial}{\partial x^{\kappa\lambda}} \right)$.

Application of these mechanisms in Definitions 2.1–2.6 with results obtained in references [5–9], [20–23] enables us to find physical laws in combinatorial spacetimes by mathematical equations, and then find their multi-solutions in following sections.

3 Combinatorial gravitational fields

3.1 Gravitational equations

The essence in Einstein's notion on the gravitational field is known in two principles following.

Principle 3.1 *These gravitational forces and inertial forces acting on a particle in a gravitational field are equivalent and indistinguishable from each other.*

Principle 3.2 *An equation describing a law of physics should have the same form in all reference frame.*

By Principle 3.1, one can introduce inertial coordinate system in Einstein's spacetime which enables it flat locally, i.e., transfer these Riemannian metrics to Minkowskian ones and eliminate the gravitational forces locally. Principle 3.2 means that a physical equation should be a tensor equation. But *how about the combinatorial gravitational field*? We assume Principles 3.1 and 3.2 hold in this case, i.e., a physical law is characterized by a tensor equation. This assumption enables us to deduce the gravitational field equation following.

Let $\mathscr{L}_{G^L[\widetilde{M}]}$ be the Lagrange density of a combinatorial spacetime $(\mathscr{C}_G|\bar{t})$. Then we know equations of the combinatorial gravitational field $(\mathscr{C}_G|\bar{t})$ to be

$$\partial_\mu \frac{\partial \mathscr{L}_{G^L[\widetilde{M}]}}{\partial \partial_\mu \phi_{\widetilde{M}}} - \frac{\partial \mathscr{L}_{G^L[\widetilde{M}]}}{\partial \phi_{\widetilde{M}}} = 0 , \qquad (3.1)$$

by the Euler-Lagrange equation, where $\phi_{\widetilde{M}}$ is the wave function of $(\mathscr{C}_G|\bar{t})$. Choose its Lagrange density $\mathscr{L}_{G^L[\widetilde{M}]}$ to be

$$\mathscr{L}_{G^L[\widetilde{M}]} = \widetilde{R} - 2\kappa \mathscr{L}_F ,$$

where $\kappa = -8\pi G$ and $\mathscr{L}_F$ the Lagrange density for all other fields with

$$\widetilde{R} = g^{(\mu\nu)(\kappa\lambda)} \widetilde{R}_{(\mu\nu)(\kappa\lambda)}, \quad \widetilde{R}_{(\mu\nu)(\kappa\lambda)} = \widetilde{R}^{\sigma\varsigma}_{(\mu\nu)(\sigma\varsigma)(\kappa\lambda)} .$$

Applying the Euler-Lagrange equation we get the equation of combinatorial gravitational field following

$$\widetilde{\mathcal{R}}_{(\mu\nu)(\kappa\lambda)} - \frac{1}{2} \widetilde{R}\, g_{(\mu\nu)(\kappa\lambda)} = \kappa \mathscr{E}_{(\mu\nu)(\kappa\lambda)} , \qquad (3.2)$$

where $\mathscr{E}_{(\mu\nu)(\kappa\lambda)}$ is the energy-momentum tensor.

The situation for combinatorial gravitational field is a little different from classical field by its combinatorial character with that one can only determines unilateral or part behaviors of the field. We generalize the Einstein notion to combinatorial gravitational field by the following projective principle, which is coordinated with one's observation.

Principle 3.3 *A physics law in a combinatorial field is invariant under a projection on its a field.*

By Principles 3.1 and 3.2 with combinatorial differential geometry shown in Section 2, Principle 3.3 can be rephrased as follows.

Projective principle *Let $(\widetilde{M}, g, \widetilde{D})$ be a combinatorial Riemannian manifold and $\mathscr{F} \in T^r_s(\widetilde{M})$ with a local form*

$$\mathscr{F}^{(\kappa_1\lambda_1)\cdots(\kappa_r\lambda_r)}_{(\mu_1\nu_1)\cdots(\mu_s\nu_s)} e_{\kappa_1\lambda_1} \otimes \cdots \otimes e_{\kappa_r\lambda_r} \omega^{\mu_1\nu_1} \otimes \cdots \otimes \omega^{\mu_s\nu_s}$$

in $(U_p, [\varphi_p])$. If

$$\mathscr{F}^{(\kappa_1\lambda_1)\cdots(\kappa_r\lambda_r)}_{(\mu_1\nu_1)\cdots(\mu_s\nu_s)} = 0$$

for integers $1 \leqslant \mu_i \leqslant s(p), 1 \leqslant \nu_i \leqslant n_{\mu_i}$ with $1 \leqslant i \leqslant s$ and $1 \leqslant \kappa_j \leqslant s(p), 1 \leqslant \lambda_j \leqslant n_{\kappa_j}$ with $1 \leqslant j \leqslant r$, then for any integer $\mu, 1 \leqslant \mu \leqslant s(p)$, there must be

$$\mathscr{F}^{(\mu\lambda_1)\cdots(\mu\lambda_r)}_{(\mu\nu_1)\cdots(\mu\nu_s)} = 0$$

for integers ν_i, $1 \leqslant \nu_i \leqslant n_\mu$ with $1 \leqslant i \leqslant s$.

Certainly, we can only determine the behavior of space which we live. Then *what is about these other spaces in* $(\mathscr{C}_G|\bar{t})$? Applying the projective principle, we can simulate each of them by that of our living space. In other words, combining geometrical structures already known to a combinatorial one $(\mathscr{C}_G|\bar{t})$ and then find its solution for equation (3.2).

3.2 Combinatorial metric

Let $\widetilde{\mathcal{A}}$ be an atlas on $(\widetilde{M}, g, \widetilde{D})$. Choose a local chart $(U; \varpi)$ in $\widetilde{\mathcal{A}}$. By definition, if $\varphi_p : U_p \to \bigcup_{i=1}^{s(p)} B^{n_i(p)}$ and $\widehat{s}(p) = \dim(\bigcap_{i=1}^{s(p)} B^{n_i(p)})$, then $[\varphi_p]$ is an $s(p) \times n_{s(p)}$ matrix. A *combinatorial metric* is defined by

$$ds^2 = g_{(\mu\nu)(\kappa\lambda)} dx^{\mu\nu} dx^{\kappa\lambda}, \tag{3.3}$$

where $g_{(\mu\nu)(\kappa\lambda)}$ is the Riemannian metric in the combinatorially Riemannian manifold $(\widetilde{M}, g, \widetilde{D})$. Generally, we choose a orthogonal basis

$$\{\overline{e}_{11}, \cdots, \overline{e}_{1n_1}, \cdots, \overline{e}_{s(p)n_{s(p)}}\}$$

for $\varphi_p[U]$, $p \in \widetilde{M}(t)$, i.e., $\left\langle \overline{e}_{\mu\nu}, \overline{e}_{\kappa\lambda} \right\rangle = \delta^{(\kappa\lambda)}_{(\mu\nu)}$. Then the formula (3.3) turns to

$$\begin{aligned} ds^2 &= g_{(\mu\nu)(\mu\nu)}(dx^{\mu\nu})^2 \\ &= \sum_{\mu=1}^{s(p)} \sum_{\nu=1}^{\widehat{s}(p)} g_{(\mu\nu)(\mu\nu)} (dx^{\mu\nu})^2 + \\ &\quad + \sum_{\mu=1}^{s(p)} \sum_{\nu=1}^{\widehat{s}(p)+1} g_{(\mu\nu)(\mu\nu)} (dx^{\mu\nu})^2 \\ &= \frac{1}{s^2(p)} \sum_{\nu=1}^{\widehat{s}(p)} \left(\sum_{\mu=1}^{s(p)} g_{(\mu\nu)(\mu\nu)} \right) dx^\nu + \\ &\quad + \sum_{\mu=1}^{s(p)} \sum_{\nu=1}^{\widehat{s}(p)+1} g_{(\mu\nu)(\mu\nu)} (dx^{\mu\nu})^2 . \end{aligned}$$

We therefore find an important relation of combinatorial metric with that of its projections following.

Theorem 3.1 *Let ${}_\mu ds^2$ be the metric in a manifold $\phi_p^{-1}(B^{n_\mu(p)})$ for integers $1 \leqslant \mu \leqslant s(p)$. Then*

$$ds^2 = {}_1ds^2 + {}_2ds^2 + \cdots + {}_{s(p)}ds^2 .$$

Proof Applying the projective principle, we immediately know that

$${}_\mu ds^2 = ds^2|_{\phi_p^{-1}(B^{n_\mu(p)})}, \qquad 1 \leqslant \mu \leqslant s(p) .$$

Whence, we find that

$$\begin{aligned} ds^2 &= g_{(\mu\nu)(\mu\nu)} (dx^{\mu\nu})^2 \\ &= \sum_{\mu=1}^{s(p)} \sum_{\nu=1}^{n_i(p)} g_{(\mu\nu)(\mu\nu)} (dx^{\mu\nu})^2 \\ &= \sum_{\mu=1}^{s(p)} ds^2|_{\phi_p^{-1}(B^{n_\mu(p)})} = \sum_{\mu=1}^{s(p)} {}_\mu ds^2 . \end{aligned}$$

□

This relation enables us to find the line element of combinatorial gravitational field $(\mathscr{C}_G|\bar{t})$ by applying that of gravitational fields.

3.3 Combinatorial Schwarzschild metric

Let $(\mathscr{C}_G|\bar{t})$ be a gravitational field. We know its Schwarzschild metric, i.e., a spherically symmetric solution of Einstein's gravitational equations in vacuum is

$$\begin{aligned} ds^2 &= \left(1 - \frac{r_s}{r}\right) dt^2 - \frac{dr^2}{1 - \frac{r_s}{r}} - \\ &\quad - r^2 d\theta^2 - r^2 \sin^2\theta d\phi^2 , \end{aligned} \tag{3.4}$$

where $r_s = 2Gm/c^2$. Now we generalize it to combinatorial gravitational fields to find the solutions of equations

$$R_{(\mu\nu)(\sigma\tau)} - \frac{1}{2} g_{(\mu\nu)(\sigma\tau)} R = -8\pi G \mathscr{E}_{(\mu\nu)(\sigma\tau)}$$

in vacuum, i.e., $\mathscr{E}_{(\mu\nu)(\sigma\tau)} = 0$. Notice that the underlying graph of combinatorial field consisting of m gravitational fields is a complete graph K_m. For such a objective, we only consider the homogeneous combinatorial Euclidean spaces $\widetilde{M} = \bigcup_{i=1}^m \mathbf{R}^{n_i}$, i.e., for any point $p \in \widetilde{M}$,

$$[\varphi_p] = \begin{bmatrix} x^{11} & \cdots & x^{1n_1} & \cdots & 0 \\ x^{21} & \cdots & x^{2n_2} & \cdots & 0 \\ \cdots & \cdots & \cdots & \cdots & \cdots \\ x^{m1} & \cdots & \cdots & \cdots & x^{mn_m} \end{bmatrix}$$

with $\widehat{m} = \dim(\bigcap_{i=1}^m \mathbf{R}^{n_i})$ a constant for $\forall p \in \bigcap_{i=1}^m \mathbf{R}^{n_i}$ and $x^{il} = \frac{x^l}{m}$ for $1 \leqslant i \leqslant m, 1 \leq l \leqslant \widehat{m}$.

Let $(\mathscr{C}_G|\bar{t})$ be a combinatorial field of gravitational fields $M_1, \cdots, M_m$ with masses $m_1, \cdots, m_m$ respectively. For usually undergoing, we consider the case of $n_\mu = 4$ for $1 \leqslant \mu \leqslant m$ since line elements have been found concretely in classical gravitational field in these cases. Now establish m spherical coordinate subframe $(t_\mu; r_\mu, \theta_\mu, \phi_\mu)$ with its originality at the center of such a mass space. Then we have known its a spherically symmetric solution by (3.4) to be

$$\begin{aligned} ds_\mu^2 &= \left(1-\frac{r_{\mu s}}{r_\mu}\right)dt_\mu^2 - \left(1-\frac{r_{\mu s}}{r_\mu}\right)^{-1} dr_\mu^2 - \\ &\quad - r_\mu^2(d\theta_\mu^2 + \sin^2\theta_\mu d\phi_\mu^2) \end{aligned}$$

for $1 \leqslant \mu \leqslant m$ with $r_{\mu s} = 2Gm_\mu/c^2$. By Theorem 3.1, we know that

$$ds^2 = {}_1ds^2 + {}_2ds^2 + \cdots + {}_mds^2\,,$$

where ${}_\mu ds^2 = ds_\mu^2$ by the projective principle on combinatorial fields. Notice that $1 \leqslant \widehat{m} \leqslant 4$. We therefore get the geometrical of $(\mathscr{C}_G|\bar{t})$ dependent on $\widehat{m}$ following.

Case 1. *$\widehat{m} = 1$, i.e., $t_\mu = t$ for $1 \leqslant \mu \leqslant m$.*

In this case, the combinatorial metric ds is

$$\begin{aligned} ds^2 &= \sum_{\mu=1}^m \left(1-\frac{2Gm_\mu}{c^2 r_\mu}\right)dt^2 - \\ &\quad - \sum_{\mu=1}^m \left(1-\frac{2Gm_\mu}{c^2 r_\mu}\right)^{-1} dr_\mu^2 - \\ &\quad - \sum_{\mu=1}^m r_\mu^2\left(d\theta_\mu^2 + \sin^2\theta_\mu d\phi_\mu^2\right). \end{aligned}$$

Case 2. *$\widehat{m} = 2$, i.e., $t_\mu = t$ and $r_\mu = r$, or $t_\mu = t$ and $\theta_\mu = \theta$, or $t_\mu = t$ and $\phi_\mu = \phi$ for $1 \leqslant \mu \leqslant m$.*

We consider the following subcases.

Subcase 2.1. *$t_\mu = t$, $r_\mu = r$.*

In this subcase, the combinatorial metric is

$$\begin{aligned} ds^2 &= \sum_{\mu=1}^m \left(1-\frac{2Gm_\mu}{c^2 r}\right)dt^2 - \\ &\quad - \left(\sum_{\mu=1}^m \left(1-\frac{2Gm_\mu}{c^2 r}\right)^{-1}\right)dr^2 - \\ &\quad - \sum_{\mu=1}^m r^2\left(d\theta_\mu^2 + \sin^2\theta_\mu d\phi_\mu^2\right), \end{aligned}$$

which can only happens if these m fields are at a same point O in a space. Particularly, if $m_\mu = M$ for $1 \leqslant \mu \leqslant m$, the masses of $M_1, M_2, \cdots, M_m$ are the same, then $r_{\mu g} = 2GM$ is a constant, which enables us knowing that

$$\begin{aligned} ds^2 &= \left(1-\frac{2GM}{c^2 r}\right)mdt^2 - \\ &\quad - \left(1-\frac{2GM}{c^2 r}\right)^{-1} mdr^2 - \\ &\quad - \sum_{\mu=1}^m r^2\left(d\theta_\mu^2 + \sin^2\theta_\mu d\phi_\mu^2\right). \end{aligned}$$

Subcase 2.2. *$t_\mu = t$, $\theta_\mu = \theta$.*

In this subcase, the combinatorial metric is

$$\begin{aligned} ds^2 &= \sum_{\mu=1}^m \left(1-\frac{2Gm_\mu}{c^2 r_\mu}\right)dt^2 - \\ &\quad - \sum_{\mu=1}^m \left(1-\frac{2Gm_\mu}{c^2 r_\mu}\right)^{-1} dr_\mu^2 - \\ &\quad - \sum_{\mu=1}^m r_\mu^2\left(d\theta^2 + \sin^2\theta d\phi_\mu^2\right). \end{aligned}$$

Subcase 2.3. *$t_\mu = t$, $\phi_\mu = \phi$.*

In this subcase, the combinatorial metric is

$$\begin{aligned} ds^2 &= \sum_{\mu=1}^m \left(1-\frac{2Gm_\mu}{c^2 r_\mu}\right)dt^2 - \\ &\quad - \left(\sum_{\mu=1}^m \left(1-\frac{2Gm_\mu}{c^2 r_\mu}\right)^{-1}\right)dr_\mu^2 - \\ &\quad - \sum_{\mu=1}^m r_\mu^2\left(d\theta_\mu^2 + \sin^2\theta_\mu d\phi^2\right). \end{aligned}$$

Case 3. *$\widehat{m} = 3$, i.e., $t_\mu = t$, $r_\mu = r$ and $\theta_\mu = \theta$, or $t_\mu = t$, $r_\mu = r$ and $\phi_\mu = \phi$, or $t_\mu = t$, $\theta_\mu = \theta$ and $\phi_\mu = \phi$ for $1 \leqslant \mu \leqslant m$.*

We consider three subcases following.

Subcase 3.1. *$t_\mu = t$, $r_\mu = r$ and $\theta_\mu = \theta$.*

In this subcase, the combinatorial metric is

$$\begin{aligned} ds^2 &= \sum_{\mu=1}^m \left(1-\frac{2Gm_\mu}{c^2 r}\right)dt^2 - \\ &\quad - \sum_{\mu=1}^m \left(1-\frac{2Gm_\mu}{c^2 r}\right)^{-1} dr^2 - \\ &\quad - mr^2 d\theta^2 - r^2\sin^2\theta\sum_{\mu=1}^m d\phi_\mu^2\,. \end{aligned}$$

Subcase 3.2. *$t_\mu = t$, $r_\mu = r$ and $\phi_\mu = \phi$.*

In this subcase, the combinatorial metric is

$$\begin{aligned} ds^2 &= \sum_{\mu=1}^{m}\left(1-\frac{2Gm_\mu}{c^2r}\right)dt^2 - \\ &\quad -\sum_{\mu=1}^{m}\left(1-\frac{2Gm_\mu}{c^2r}\right)^{-1}dr^2 - \\ &\quad -r^2\sum_{\mu=1}^{m}\left(d\theta_\mu^2+\sin^2\theta_\mu d\phi^2\right). \end{aligned}$$

There subcases 3.1 and 3.2 can be only happen if the centers of these m fields are at a same point O in a space.

Subcase 3.3. *$t_\mu = t$, $\theta_\mu = \theta$ and $\phi_\mu = \phi$.*

In this subcase, the combinatorial metric is

$$\begin{aligned} ds^2 &= \sum_{\mu=1}^{m}\left(1-\frac{2Gm_\mu}{c^2r_\mu}\right)dt^2 - \\ &\quad -\sum_{\mu=1}^{m}\left(1-\frac{2Gm_\mu}{c^2r_\mu}\right)^{-1}dr_\mu^2 - \\ &\quad -\sum_{\mu=1}^{m}r_\mu\left(d\theta^2+\sin^2\theta d\phi^2\right). \end{aligned}$$

Case 4. *$\widehat{m} = 4$, i.e., $t_\mu = t$, $r_\mu = r$, $\theta_\mu = \theta$ and $\phi_\mu = \phi$ for $1 \leqslant \mu \leqslant m$.*

In this subcase, the combinatorial metric is

$$\begin{aligned} ds^2 &= \sum_{\mu=1}^{m}\left(1-\frac{2Gm_\mu}{c^2r}\right)dt^2 - \\ &\quad -\sum_{\mu=1}^{m}\left(1-\frac{2Gm_\mu}{c^2r}\right)^{-1}dr^2 - \\ &\quad -mr^2\left(d\theta^2+\sin^2\theta d\phi^2\right). \end{aligned}$$

Particularly, if $m_\mu = M$ for $1 \leqslant \mu \leqslant m$, we get that

$$\begin{aligned} ds^2 &= \left(1-\frac{2GM}{c^2r}\right)mdt^2 - \\ &\quad -\left(1-\frac{2GM}{c^2r}\right)^{-1}mdr^2 - \\ &\quad -mr^2\left(d\theta^2+\sin^2\theta d\phi^2\right). \end{aligned}$$

Define a coordinate transformation

$$(t, r, \theta, \phi) \to ({}_st,\ {}_sr,\ {}_s\theta,\ {}_s\phi) = (t\sqrt{m}, r\sqrt{m}, \theta, \phi).$$

Then the previous formula turns to

$$\begin{aligned} ds^2 &= \left(1-\frac{2GM}{c^2r}\right)d_st^2 - \frac{d_sr^2}{1-\frac{2GM}{c^2r}} - \\ &\quad -{}_sr^2\left(d_s\theta^2+\sin^2\ {}_s\theta d_s\phi^2\right) \end{aligned}$$

in this new coordinate system $({}_st,\ {}_sr,\ {}_s\theta,\ {}_s\phi)$, whose geometrical behavior likes that of the gravitational field.

3.4 Combinatorial Reissner-Nordström metric

The Schwarzschild metric is a spherically symmetric solution of the Einstein gravitational equations in conditions $\mathscr{E}_{(\mu\nu)(\sigma\tau)} = 0$. In some special cases, we can also find their solutions for the case $\mathscr{E}_{(\mu\nu)(\sigma\tau)} \neq 0$. The *Reissner-Nordström metric* is such a case with

$$\mathscr{E}_{(\mu\nu)(\sigma\tau)} = \frac{1}{4\pi}\left(\frac{1}{4}\,g_{\mu\nu}F_{\alpha\beta}F^{\alpha\beta} - F_{\mu\alpha}F^{\alpha}_{\nu}\right)$$

in the Maxwell field with total mass m and total charge e, where $F_{\alpha\beta}$ and $F^{\alpha\beta}$ are given in Subsection 7.3.4. Its metrics takes the following form:

$$g_{\mu\nu} = \begin{bmatrix} x_{11} & 0 & 0 & 0 \\ 0 & x_{22} & 0 & 0 \\ 0 & 0 & -r^2 & 0 \\ 0 & 0 & 0 & -r^2\sin^2\theta \end{bmatrix},$$

where $r_s = 2Gm/c^2$, $r_e^2 = 4G\pi e^2/c^4$, $x_{11} = 1 - \dfrac{r_s}{r} + \dfrac{r_e^2}{r^2}$ and $x_{22} = -\left(1 - \dfrac{r_s}{r} + \dfrac{r_e^2}{r^2}\right)^{-1}$. In this case, its line element ds is given by

$$\begin{aligned} ds^2 &= \left(1-\frac{r_s}{r}+\frac{r_e^2}{r^2}\right)dt^2 - \\ &\quad -\left(1-\frac{r_s}{r}+\frac{r_e^2}{r^2}\right)^{-1}dr^2 - \\ &\quad -r^2\left(d\theta^2+\sin^2\theta d\phi^2\right). \end{aligned} \tag{3.5}$$

Obviously, if $e = 0$, i.e., there are no charges in the gravitational field, then the equations (3.5) turns to that of the Schwarzschild metric (3.4).

Now let $(\mathscr{C}_G|\bar{t})$ be a combinatorial field of charged gravitational fields $M_1, M_2, \cdots, M_m$ with masses $m_1, m_2, \cdots, m_m$ and charges $e_1, e_2, \cdots, e_m$, respectively. Similar to the case of Schwarzschild metric, we consider the case of $n_\mu = 4$ for $1 \leqslant \mu \leqslant m$. We establish m spherical coordinate subframe $(t_\mu; r_\mu, \theta_\mu, \phi_\mu)$ with its originality at the center of such a mass space. Then we know its a spherically symmetric solution by (3.5) to be

$$\begin{aligned} ds_\mu^2 &= \left(1-\frac{r_{\mu s}}{r_\mu}+\frac{r_{\mu e}^2}{r_\mu^2}\right)dt_\mu^2 - \\ &\quad -\left(1-\frac{r_{\mu s}}{r_\mu}+\frac{r_{\mu e}^2}{r_\mu^2}\right)^{-1}dr_\mu^2 - \\ &\quad -r_\mu^2\left(d\theta_\mu^2+\sin^2\theta_\mu d\phi_\mu^2\right). \end{aligned}$$

Likewise the case of Schwarzschild metric, we consider combinatorial fields of charged gravitational fields dependent on the intersection dimension $\widehat{m}$ following.

Case 1. $\widehat{m}=1$, *i.e.,* $t_\mu=t$ *for* $1\leqslant\mu\leqslant m$.

In this case, by applying Theorem 3.1 we get the combinatorial metric

$$\begin{aligned} ds^2 &= \sum_{\mu=1}^{m}\left(1-\frac{r_{\mu s}}{r_\mu}+\frac{r_{\mu e}^2}{r_\mu^2}\right)dt^2- \\ &\quad -\sum_{\mu=1}^{m}\left(1-\frac{r_{\mu s}}{r_\mu}+\frac{r_{\mu e}^2}{r_\mu^2}\right)^{-1}dr_\mu^2- \\ &\quad -\sum_{\mu=1}^{m}r_\mu^2\left(d\theta_\mu^2+\sin^2\theta_\mu d\phi_\mu^2\right). \end{aligned}$$

Case 2. $\widehat{m}=2$, *i.e.,* $t_\mu=t$ *and* $r_\mu=r$, *or* $t_\mu=t$ *and* $\theta_\mu=\theta$, *or* $t_\mu=t$ *and* $\phi_\mu=\phi$ *for* $1\leqslant\mu\leqslant m$.

Consider the following three subcases.

Subcase 2.1. $t_\mu=t$, $r_\mu=r$.

In this subcase, the combinatorial metric is

$$\begin{aligned} ds^2 &= \sum_{\mu=1}^{m}\left(1-\frac{r_{\mu s}}{r}+\frac{r_{\mu e}^2}{r^2}\right)dt^2- \\ &\quad -\sum_{\mu=1}^{m}\left(1-\frac{r_{\mu s}}{r}+\frac{r_{\mu e}^2}{r^2}\right)^{-1}dr^2- \\ &\quad -\sum_{\mu=1}^{m}r^2\left(d\theta_\mu^2+\sin^2\theta_\mu d\phi_\mu^2\right), \end{aligned}$$

which can only happens if these m fields are at a same point O in a space. Particularly, if $m_\mu=M$ and $e_\mu=e$ for $1\leqslant\mu\leqslant m$, we find that

$$\begin{aligned} ds^2 &= \left(1-\frac{2GM}{c^2r}+\frac{4\pi Ge^4}{c^4r^2}\right)mdt^2- \\ &\quad -\frac{mdr^2}{1-\frac{2GM}{c^2r}+\frac{4\pi Ge^4}{c^4r^2}}- \\ &\quad -\sum_{\mu=1}^{m}r^2\left(d\theta_\mu^2+\sin^2\theta_\mu d\phi_\mu^2\right). \end{aligned}$$

Subcase 2.2. $t_\mu=t$, $\theta_\mu=\theta$.

In this subcase, by applying Theorem 3.1 we know that the combinatorial metric is

$$\begin{aligned} ds^2 &= \sum_{\mu=1}^{m}\left(1-\frac{r_{\mu s}}{r_\mu}+\frac{r_{\mu e}^2}{r_\mu^2}\right)dt^2- \\ &\quad -\sum_{\mu=1}^{m}\left(1-\frac{r_{\mu s}}{r_\mu}+\frac{r_{\mu e}^2}{r_\mu^2}\right)^{-1}dr_\mu^2- \\ &\quad -\sum_{\mu=1}^{m}r_\mu^2\left(d\theta^2+\sin^2\theta d\phi_\mu^2\right). \end{aligned}$$

Subcase 2.3. $t_\mu=t$, $\phi_\mu=\phi$.

In this subcase, we know that the combinatorial metric is

$$\begin{aligned} ds^2 &= \sum_{\mu=1}^{m}\left(1-\frac{r_{\mu s}}{r_\mu}+\frac{r_{\mu e}^2}{r_\mu^2}\right)dt^2- \\ &\quad -\sum_{\mu=1}^{m}\left(1-\frac{r_{\mu s}}{r_\mu}+\frac{r_{\mu e}^2}{r_\mu^2}\right)^{-1}dr_\mu^2- \\ &\quad -\sum_{\mu=1}^{m}r_\mu^2\left(d\theta_\mu^2+\sin^2\theta_\mu d\phi^2\right). \end{aligned}$$

Case 3. $\widehat{m}=3$, *i.e.,* $t_\mu=t$, $r_\mu=r$ *and* $\theta_\mu=\theta$, *or* $t_\mu=t$, $r_\mu=r$ *and* $\phi_\mu=\phi$, *or or* $t_\mu=t$, $\theta_\mu=\theta$ *and* $\phi_\mu=\phi$ *for* $1\leqslant\mu\leqslant m$.

We consider three subcases following.

Subcase 3.1. $t_\mu=t$, $r_\mu=r$ *and* $\theta_\mu=\theta$.

In this subcase, by applying Theorem 3.1 we obtain that the combinatorial metric is

$$\begin{aligned} ds^2 &= \sum_{\mu=1}^{m}\left(1-\frac{r_{\mu s}}{r}+\frac{r_{\mu e}^2}{r^2}\right)dt^2- \\ &\quad -\sum_{\mu=1}^{m}\left(1-\frac{r_{\mu s}}{r}+\frac{r_{\mu e}^2}{r^2}\right)^{-1}dr^2- \\ &\quad -\sum_{\mu=1}^{m}r^2\left(d\theta^2+\sin^2\theta d\phi_\mu^2\right). \end{aligned}$$

Particularly, if $m_\mu=M$ and $e_\mu=e$ for $1\leqslant\mu\leqslant m$, then we get that

$$\begin{aligned} ds^2 &= \left(1-\frac{2GM}{c^2r}+\frac{4\pi Ge^4}{c^4r^2}\right)mdt^2- \\ &\quad -\frac{mdr^2}{1-\frac{2GM}{c^2r}+\frac{4\pi Ge^4}{c^4r^2}}- \\ &\quad -\sum_{\mu=1}^{m}r^2\left(d\theta^2+\sin^2\theta d\phi_\mu^2\right). \end{aligned}$$

Subcase 3.2. $t_\mu=t$, $r_\mu=r$ *and* $\phi_\mu=\phi$.

In this subcase, the combinatorial metric is

$$\begin{aligned} ds^2 &= \sum_{\mu=1}^{m}\left(1-\frac{r_{\mu s}}{r}+\frac{r_{\mu e}^2}{r^2}\right)dt^2- \\ &\quad -\sum_{\mu=1}^{m}\left(1-\frac{r_{\mu s}}{r}+\frac{r_{\mu e}^2}{r^2}\right)^{-1}dr^2- \\ &\quad -\sum_{\mu=1}^{m}r^2\left(d\theta_\mu^2+\sin^2\theta_\mu d\phi^2\right). \end{aligned}$$

Particularly, if $m_\mu = M$ and $e_\mu = e$ for $1 \leqslant \mu \leqslant m$, then we get that

$$\begin{aligned} ds^2 &= \left(1 - \frac{2GM}{c^2 r} + \frac{4\pi G e^4}{c^4 r^2}\right) m dt^2 - \\ &- \frac{m dr^2}{1 - \frac{2GM}{c^2 r} + \frac{4\pi G e^4}{c^4 r^2}} - \\ &- \sum_{\mu=1}^{m} r^2 \left(d\theta_\mu^2 + \sin^2 \theta_\mu d\phi^2\right). \end{aligned}$$

Subcase 3.3. *$t_\mu = t$, $\theta_\mu = \theta$ and $\phi_\mu = \phi$.*

In this subcase, the combinatorial metric is

$$\begin{aligned} ds^2 &= \sum_{\mu=1}^{m} \left(1 - \frac{r_{\mu s}}{r_\mu} + \frac{r_{\mu e}^2}{r_\mu^2}\right) dt^2 - \\ &- \sum_{\mu=1}^{m} \left(1 - \frac{r_{\mu s}}{r_\mu} + \frac{r_{\mu e}^2}{r_\mu^2}\right)^{-1} dr_\mu^2 - \\ &- \sum_{\mu=1}^{m} r_\mu^2 \left(d\theta^2 + \sin^2 \theta d\phi^2\right). \end{aligned}$$

Case 4. *$\widehat{m} = 4$, i.e., $t_\mu = t, r_\mu = r, \theta_\mu = \theta$ and $\phi_\mu = \phi$ for $1 \leqslant \mu \leqslant m$.*

In this subcase, the combinatorial metric is

$$\begin{aligned} ds^2 &= \sum_{\mu=1}^{m} \left(1 - \frac{r_{\mu s}}{r} + \frac{r_{\mu e}^2}{r^2}\right) dt^2 - \\ &- \sum_{\mu=1}^{m} \left(1 - \frac{r_{\mu s}}{r} + \frac{r_{\mu e}^2}{r^2}\right)^{-1} dr^2 - \\ &- m r^2 \left(d\theta^2 + \sin^2 \theta d\phi^2\right). \end{aligned}$$

Furthermore, if $m_\mu = M$ and $e_\mu = e$ for $1 \leqslant \mu \leqslant m$, we obtain that

$$\begin{aligned} ds^2 &= \left(1 - \frac{2GM}{c^2 r} + \frac{4\pi G e^4}{c^4 r^2}\right) m dt^2 - \\ &- \frac{m dr^2}{1 - \frac{2GM}{c^2 r} + \frac{4\pi G e^4}{c^4 r^2}} - \\ &- m r^2 \left(d\theta^2 + \sin^2 \theta d\phi^2\right). \end{aligned}$$

Similarly, we define the coordinate transformation

$$(t, r, \theta, \phi) \to ({}_s t,\ {}_s r,\ {}_s\theta,\ {}_s\phi) = (t\sqrt{m}, r\sqrt{m}, \theta, \phi).$$

Then the previous formula turns to

$$\begin{aligned} ds^2 &= \left(1 - \frac{2GM}{c^2 r} + \frac{4\pi G e^4}{c^4 r^2}\right) d_s t^2 - \\ &- \frac{d_s r^2}{1 - \frac{2GM}{c^2 r} + \frac{4\pi G e^4}{c^4 r^2}} - \\ &- {}_s r^2 \left(d_s\theta^2 + \sin^2\ {}_s\theta d_s\phi^2\right) \end{aligned}$$

in this new coordinate system $({}_s t,\ {}_s r,\ {}_s\theta,\ {}_s\phi)$, whose geometrical behavior likes a charged gravitational field.

4 Multi-time system

A *multi-time system* is such a combinatorial field $(\mathscr{C}_G|\bar{t})$ consisting of fields $M_1, M_2, \cdots, M_m$ on reference frames

$$(t_1, r_1, \theta_1, \phi_1), \cdots, (t_m, r_m, \theta_m, \phi_m)$$

and there are always exist two integers $\kappa,\ \lambda,\ 1 \leqslant \kappa \neq \lambda \leqslant m$ such that $t_\kappa \neq t_\lambda$. Notice that these combinatorial fields discussed in Section 3 are all with $t_\mu = t$ for $1 \leqslant \mu \leqslant m$, i.e., we can establish a time variable t for all fields in this combinatorial field. But if we can not determine all the behavior of living things in the Universe implied in the *weak anthropic principle*, we can not find such a time variable t for all fields. If so, we need a multi-time system for describing the Universe.

Among these multi-time systems, an interesting case appears in $\widehat{m} = 3,\ r_\mu = r,\ \theta_\mu = \theta,\ \phi_\mu = \phi$, i.e., beings live in the same dimensional 3 space, but with different notions on the time. Applying Theorem 3.1, we discuss the Schwarzschild and Reissner-Nordström metrics following.

4.1 Schwarzschild multi-time system

In this case, the combinatorial metric is

$$\begin{aligned} ds^2 &= \sum_{\mu=1}^{m} \left(1 - \frac{2Gm_\mu}{c^2 r}\right) dt_\mu^2 - \\ &- \sum_{\mu=1}^{m} \left(1 - \frac{2Gm_\mu}{c^2 r}\right)^{-1} dr^2 - \\ &- m r^2 \left(d\theta^2 + \sin^2 \theta d\phi^2\right). \end{aligned}$$

Applying the projective principle to this equation, we get metrics on gravitational fields $M_1, M_2, \cdots, M_m$ following:

$$\begin{aligned} ds_1^2 &= \left(1 - \frac{2Gm_1}{c^2 r}\right) dt_1^2 - \\ &- \left(1 - \frac{2Gm_1}{c^2 r}\right)^{-1} dr^2 - \\ &- r^2 \left(d\theta^2 + \sin^2 \theta d\phi^2\right), \end{aligned}$$

$$\begin{aligned} ds_2^2 &= \left(1 - \frac{2Gm_2}{c^2 r}\right) dt_2^2 - \\ &- \left(1 - \frac{2Gm_2}{c^2 r}\right)^{-1} dr^2 - \\ &- r^2 \left(d\theta^2 + \sin^2 \theta d\phi^2\right), \end{aligned}$$

$$\cdots\cdots\cdots\cdots\cdots\cdots,$$

$$ds_m^2 = \left(1-\frac{2Gm_m}{c^2r}\right)dt_m^2 - \left(1-\frac{2Gm_m}{c^2r}\right)^{-1}dr^2 - r^2\left(d\theta^2+\sin^2\theta d\phi^2\right).$$

Particularly, if $m_\mu = M$ for $1 \leqslant \mu \leqslant m$, we then get that

$$ds^2 = \left(1-\frac{2GM}{c^2r}\right)\sum_{\mu=1}^{m} dt_\mu^2 - \left(1-\frac{2GM}{c^2r}\right)^{-1} mdr^2 - mr^2\left(d\theta^2+\sin^2\theta d\phi^2\right).$$

Its projection on the gravitational field M_μ is

$$ds_\mu^2 = \left(1-\frac{2GM}{c^2r}\right)dt_\mu^2 - \left(1-\frac{2GM}{c^2r}\right)^{-1}dr^2 - r^2\left(d\theta^2+\sin^2\theta d\phi^2\right),$$

i.e., the Schwarzschild metric on M_μ, $1 \leqslant \mu \leqslant m$.

4.2 Reissner-Nordström multi-time system

In this case, the combinatorial metric is

$$ds^2 = \sum_{\mu=1}^{m}\left(1-\frac{2Gm_\mu}{c^2r}+\frac{4\pi Ge_\mu^4}{c^4r^2}\right)dt_\mu^2 - \sum_{\mu=1}^{m}\left(1-\frac{2Gm_\mu}{c^2r}+\frac{4\pi Ge_\mu^4}{c^4r^2}\right)^{-1}dr^2 - mr^2\left(d\theta^2+\sin^2\theta d\phi^2\right).$$

Similarly, by the projective principle we obtain the metrics on charged gravitational fields $M_1, M_2, \cdots, M_m$ following

$$ds_1^2 = \left(1-\frac{2Gm_1}{c^2r}+\frac{4\pi Ge_1^4}{c^4r^2}\right)dt_1^2 - \left(1-\frac{2Gm_1}{c^2r}+\frac{4\pi Ge_1^4}{c^4r^2}\right)^{-1}dr^2 - r^2\left(d\theta^2+\sin^2\theta d\phi^2\right),$$

$$ds_2^2 = \left(1-\frac{2Gm_2}{c^2r}+\frac{4\pi Ge_2^4}{c^4r^2}\right)dt_2^2 - \left(1-\frac{2Gm_2}{c^2r}+\frac{4\pi Ge_2^4}{c^4r^2}\right)^{-1}dr^2 - r^2\left(d\theta^2+\sin^2\theta d\phi^2\right),$$

$$\cdots\cdots\cdots\cdots\cdots\cdots\cdots,$$

$$ds_m^2 = \left(1-\frac{2Gm_m}{c^2r}+\frac{4\pi Ge_m^4}{c^4r^2}\right)dt_m^2 - \left(1-\frac{2Gm_m}{c^2r}+\frac{4\pi Ge_m^4}{c^4r^2}\right)^{-1}dr^2 - r^2\left(d\theta^2+\sin^2\theta d\phi^2\right).$$

Furthermore, if $m_\mu = M$ and $e_\mu = e$ for $1 \leqslant \mu \leqslant m$, we obtain that

$$ds^2 = \left(1-\frac{2GM}{c^2r}+\frac{4\pi Ge^4}{c^4r^2}\right)\sum_{\mu=1}^{m} dt^2 - \left(1-\frac{2GM}{c^2r}+\frac{4\pi Ge^4}{c^4r^2}\right)^{-1} mdr^2 - mr^2\left(d\theta^2+\sin^2\theta d\phi^2\right).$$

Its projection on the charged gravitational field M_μ is

$$ds_\mu^2 = \left(1-\frac{2GM}{c^2r}+\frac{4\pi Ge^4}{c^4r^2}\right)dt_\mu^2 - \left(1-\frac{2GM}{c^2r}+\frac{4\pi Ge^4}{c^4r^2}\right)^{-1}dr^2 - r^2\left(d\theta^2+\sin^2\theta d\phi^2\right),$$

i.e., the Reissner-Nordström metric on M_μ, $1 \leqslant \mu \leqslant m$.

As a by-product, these calculations and formulas mean that these beings with time notion different from that of human beings will recognize differently the structure of our universe if these beings are intellectual enough to do so.

5 Discussions

5.1 Geometrical structure

A simple calculation shows that the dimension of the combinatorial gravitational field $(\mathscr{C}|\bar{t})$ in Section 3 is

$$\dim(\mathscr{C}|\bar{t}) = 4m + (1-m)\widehat{m}. \tag{5.1}$$

For example, $\dim(\mathscr{C}|\bar{t}) = 7,\ 10,\ 13,\ 16$ if $\widehat{m} = 1$ and $6,\ 8,\ 10$ if $\widehat{m} = 1$ for $m = 2,\ 3,\ 4$. In this subsection, we analyze these geometrical structures with metrics appeared in Section 3.

As we have said in Section 1, the visible geometry is the spherical geometry of dimensional 3. That is why the sky looks like a spherical surface. In this geometry, we can only see the images of bodies with $\dim \geqslant 3$ on our spherical surface (see [1–2] and [4] in details). But the situation is a little difference from that of the transferring information, which is transferred in all possible routes. In other words, a geometry of dimensional $\geqslant 1$. Therefore, not all information transferring can be seen by our eyes. But some of them can be felt by

our six organs with the help of apparatus if needed. For example, the *magnetism* or *electromagnetism* can be only detected by apparatus. These notions enable us to explain the geometrical structures in combinatorial gravitational fields, for example, the Schwarzschild or Reissner-Nordström metrics.

Case 1. $\widehat{m} = 4$.

In this case, by the formula (5.1) we get $\dim(\mathscr{C}|\bar{t}) = 4$, i.e., all fields $M_1, M_2, \cdots, M_m$ are in $\mathbf{R}^4$, which is the most enjoyed case by human beings. We have gotten the Schwarzschild metric

$$\begin{aligned} ds^2 &= \sum_{\mu=1}^{m}\left(1-\frac{2Gm_\mu}{c^2r}\right)dt^2 - \\ &\quad -\sum_{\mu=1}^{m}\left(1-\frac{2Gm_\mu}{c^2r}\right)^{-1}dr^2 - \\ &\quad - mr^2(d\theta^2+\sin^2\theta d\phi^2) \end{aligned}$$

or the Reissner-Nordström metric

$$\begin{aligned} ds^2 &= \sum_{\mu=1}^{m}\left(1-\frac{r_{\mu s}}{r}+\frac{r_{\mu e}^2}{r^2}\right)dt^2 - \\ &\quad -\frac{dr^2}{\sum\limits_{\mu=1}^{m}\left(1-\frac{r_{\mu s}}{r}+\frac{r_{\mu e}^2}{r^2}\right)} - \\ &\quad - mr^2\left(d\theta^2+\sin^2\theta d\phi^2\right) \end{aligned}$$

for non-charged or charged combinatorial gravitational fields in vacuum in Sections 3. If it is so, the behavior of Universe can be realized finally by human beings. This also means that the discover of science will be ended, i.e., we can established the *Theory of Everything* finally for the Universe.

Case 2. $\widehat{m} \leqslant 3$.

If the Universe is so, then $\dim(\mathscr{C}|\bar{t}) \geqslant 5$. In this case, we know the combinatorial Schwarzschild metrics and combinatorial Reissner-Nordström metrics in Section 3, for example, if $t_\mu = t$, $r_\mu = r$ and $\phi_\mu = \phi$, the combinatorial Schwarzschild metric is

$$\begin{aligned} ds^2 &= \sum_{\mu=1}^{m}\left(1-\frac{r_{\mu s}}{r}\right)dt^2 - \sum_{\mu=1}^{m}\frac{dr^2}{\left(1-\frac{r_{\mu s}}{r}\right)} - \\ &\quad -\sum_{\mu=1}^{m} r^2\left(d\theta_\mu^2+\sin^2\theta_\mu d\phi^2\right) \end{aligned}$$

and the combinatorial Reissner-Nordström metric is

$$\begin{aligned} ds^2 &= \sum_{\mu=1}^{m}\left(1-\frac{r_{\mu s}}{r}+\frac{r_{\mu e}^2}{r^2}\right)dt^2 - \\ &\quad -\sum_{\mu=1}^{m}\frac{dr^2}{\left(1-\frac{r_{\mu s}}{r}+\frac{r_{\mu e}^2}{r^2}\right)} - \\ &\quad -\sum_{\mu=1}^{m} r^2\left(d\theta_\mu^2+\sin^2\theta_\mu d\phi^2\right). \end{aligned}$$

Particularly, if $m_\mu = M$ and $e_\mu = e$ for $1 \leqslant \mu \leqslant m$, then we get that

$$\begin{aligned} ds^2 &= \left(1-\frac{2GM}{c^2r}\right)mdt^2 - \frac{mdr^2}{\left(1-\frac{2GM}{c^2r}\right)} - \\ &\quad -\sum_{\mu=1}^{m} r^2\left(d\theta_\mu^2+\sin^2\theta_\mu d\phi^2\right) \end{aligned}$$

for combinatorial gravitational field and

$$\begin{aligned} ds^2 &= \left(1-\frac{2GM}{c^2r}+\frac{4\pi Ge^4}{c^4r^2}\right)mdt^2 - \\ &\quad -\frac{mdr^2}{\left(1-\frac{2GM}{c^2r}+\frac{4\pi Ge^4}{c^4r^2}\right)} - \\ &\quad -\sum_{\mu=1}^{m} r^2\left(d\theta_\mu^2+\sin^2\theta_\mu d\phi^2\right) \end{aligned}$$

for charged combinatorial gravitational field in vacuum. In this case, the observed interval in the field M_O where human beings live is

$$\begin{aligned} ds_O &= a(t,r,\theta,\phi)dt^2 - b(t,r,\theta,\phi)dr^2 - \\ &\quad - c(t,r,\theta,\phi)d\theta^2 - d(t,r,\theta,\phi)d\phi^2. \end{aligned}$$

How to we explain the differences $ds - ds_O$ in physics? Notice that we can only observe the line element ds_O, a projection of ds on M_O. Whence, all contributions in $ds - ds_O$ come from the spatial direction not observable by human beings. In this case, we are difficult to determine the exact behavior. Furthermore, if $\widehat{m} \leqslant 3$ holds, because there are infinite combinations $(\mathscr{C}_G|\bar{t})$ of existent fields underlying a connected graph G, we can not find an ultimate theory for the Universe, i.e., there are no a *Theory of Everything* for the Universe and the science established by ours is approximate, holds on conditions and the discover of science will be endless forever.

5.2 Physical formation

A generally accepted notion on the formation of Universe is the Big Bang theory ([24]), i.e., the origin of Universe is from an exploded at a singular point on its beginning. Notice that the geometry in the Big Bang theory is just a Euclidean $\mathbf{R}^3$ geometry, i.e., a visible geometry by human beings. Then *how is it came into being for a combinatorial spacetime*? *Weather it is contradicts to the experimental data*? We will explain these questions following.

Realization 5.1 *Any combinatorial spacetime was formed by $|G|$ times Big Bang in an early space.*

Certainly, if there is just one time Big Bang, then there exists one spacetime observed by us, not a multiple or combinatorial spacetime. But there are no arguments for this claim.

It is only an assumption on the origin of Universe. If it is not exploded in one time, but in $m \geqslant 2$ times in different spatial directions, *what will happens for the structure of spacetime*?

The process of Big Bang model can be applied for explaining the formation of combinatorial spacetimes. Assume the dimension of original space is bigger enough and there are m explosions for the origin of Universe. Then likewise the standard process of Big Bang, each time of Big Bang brought a spacetime. After the m Big Bangs, we finally get a multi-spacetime underlying a combinatorial structure, i.e., a combinatorial spacetime $(\mathscr{C}_G|\bar{t})$ with $|G| = m$, such as those shown in Fig. 5.1 for $G = C_4$ or K_3.

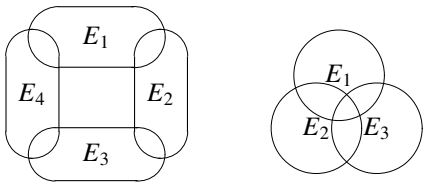

Fig. 5.1

where E_i denotes i^{th} time explosion for $1 \leq i \leqslant 4$. In the process of m Big Bangs, we do not assume that each explosion E_i, $1 \leqslant i \leqslant m$ was happened in a Euclidean space $\mathbf{R}^3$, but in $\mathbf{R}^n$ for $n \geqslant 3$. Whence, the intersection $E_i \cap E_j$ means the same spatial directions in explosions E_i and E_j for $1 \leqslant i, j \leqslant m$. Whence, information in E_i or E_j appeared along directions in $E_i \cap E_j$ will both be reflected in E_j or E_i. As we have said in Subsection 5.1, if $\dim E_i \cap E_j \leqslant 2$, then such information can not be seen by us but only can be detected by apparatus, such as those of the *magnetism* or *electromagnetism*.

Realization 5.2 *The spacetime lived by us is an intersection of other spacetimes.*

This fact is an immediately conclusion of Realization 5.1.

Realization 5.3 *Each experimental data on Universe obtained by human beings is synthesized, not be in one of its spacetimes.*

Today, we have known a few datum on the Universe by COBE or WMAP. In these data, the one well-known is the 2.7^oK cosmic microwave background radiation. Generally, this data is thought to be an evidence of Big Bang theory. If the Universe is a combinatorial one, *how to we explain it*? First, the 2.7^oK is not contributed by one Big Bang in $\mathbf{R}^3$, but by many times before 137 light years, i.e., it is a synthesized data. Second, the 2.7^oK is surveyed by WMAP, an explorer satellite in $\mathbf{R}^3$. By the projective principle in Section 3, it is only a projection of the cosmic microwave background radiation in the Universe on the space $\mathbf{R}^3$ lived by us. In fact, all datum on the Universe surveyed by human beings can be explained in such a way. So there are no contradiction between combinatorial model and datum on the Universe already known by us, but it reflects a combinatorial behavior of the Universe.

Submitted on February 22, 2010 / Accepted March 12, 2010

References

1. Belot G. Remarks on the geometry of visibles. *Philosophical Quarterly*, 2003, v. 53, 581–586.
2. Reid T. An inquiry into the human mind on the principles of common sense. In D. Brookes ed., Edinburgh University Press, 1997.
3. Shtanov Y.V. On brane-world cosmology. arXiv: hep-th/0005193.
4. Yaffe G. Reconsidering Reid's geometry of visibles. *Philosophical Quarterly*, 2002, v. 52, 602–620.
5. Mao L.F. Geometrical theory on combinatorial manifolds. *JP J. Geometry and Topology*, 2007, v. 7, no. 1, 65–114.
6. Mao L.F. An introduction to Smarandache multi-spaces and mathematical combinatorics. *Scientia Magna*, 2007, v. 3, no.1, 54–80.
7. Mao L.F. Curvature equations on combinatorial manifolds with applications to theoretical physics. *International J. Mathematical Combinatorics*, 2008, v. 1, 1–25.
8. Mao L.F. Combinatorially Riemannian submanifolds. *International J. Mathematical Combinatorics*, 2008, v. 2, 1–25.
9. Mao L.F. Combinatorial fields-an introduction. *International J. Mathematical Combinatorics*, 2009, v. 3, 1–22.
10. Rabounski D. Smarandache spaces as a new extension of the basic space-time of general relativity. *Progress in Physics*, 2010, v. 2, L1–L2.
11. Smarandache F. Mixed noneuclidean geometries. arXiv: math/0010119.
12. Moorw G.W. What is a brane? *Notices of the AMS*, 2005, v. 52, no. 2, 214–215.
13. Tegmark M. Parallel universes. In J. D. Barrow, P. C. W. Davies and C. L. Harper eds., *Science and Ultimate Reality: From Quantum to Cosmos*, Cambridge University Press, 2003.
14. Gunther U. and Zhuk A. Phenomenology of brane-world cosmological models. arXiv: gr-qc/0410130.
15. Ida D. Brane-world cosmology. arXiv: gr-qc/9912002.
16. Kanti P. Madden R. and Olive K.A. A 6-d brane world model. arXiv: hep-ph/0104177.
17. Papantonopoulos E. Braneworld cosmological models. arXiv: gr-qc/0410032.
18. Papantonopoulos E. Cosmology in six dimensions. arXiv: gr-qc/0601011.
19. Zhang T.X. A new cosmological model: black hole universe. *Progress in Physics*, 2009, v. 3, 3–11.
20. Mao L.F. Combinatorial geometry with applications to field theory. InfoQuest, USA, 2009.
21. Mao L.F. A combinatorial decomposition of Euclidean spaces $\mathbf{R}^n$ with contribution to visibility. To be submitted to publication.
22. Mao L.F. Lie multi-groups underlying graphs. To be submitted to publication.
23. Mao L.F. Constructing principal fiber bundles by voltage assignment. To be submitted to publication.
24. Peacock J.A. Cosmological physics. Cambridge University Press, 1999.

The "Proton Spin Crisis" — a Quantum Query

Johan Hansson

Department of Physics Luleå University of Technology, SE-97187 Luleå, Sweden. E-mail: c.johan.hansson@ltu.se

The "proton spin crisis" was introduced in the late 1980s, when the EMC-experiment revealed that little or nothing of a proton's spin seemed to be carried by its quarks. The main objective of this paper is to point out that it is wrong to assume that the proton spin, as measured by completely different experimental setups, should be the same in all circumstances, an assumption explicitly made in all present theoretical treatments of the "crisis". As spin is a genuine quantum property, without any objective existence outside its measuring apparatus context, proper account of quantum mechanical measurement theory must be taken.

The "proton spin crisis" [1] essentially refers to the experimental finding that very little of the spin of a proton seems to be carried by the quarks from which it is supposedly built. This was a very curious and unexpected experimental result of the European Muon Collaboration, EMC [2] (later consolidated by other experiments), as the whole idea of the original quark model of Gell-Mann [3] and Zweig [4] was to account for 100 percent of the hadronic spins, solely in terms of quarks. Although "improved" parton models can just about accomodate the experimental results, the purpose of this paper is to point out that the "proton spin crisis" may be due to a misinterpretation of the underlying, quantum mechanical theory. As spin is a fundamentally quantum mechanical entity, without any classical analog, special care must be taken to treat it in a correct quantum mechanical manner.

According to Niels Bohr, *the whole experimental setup* must be considered when we observe quantum mechanical systems. It means that a quantal object does not "really exist" independently of how it is observed. This notion was later quantified by Bell [5], and verified experimentally by Clauser and Freedman [6], Aspect, Dalibard and Roger [7] and others. These experimentally observed violations of Bell's theorem [5] are in accordance with quantum mechanics, but incompatible with a locally realistic world view, proving that quantum objects do not have objective properties unless and until they are actually measured*. The quantum states are not merely unknown, but completely undecided until measured. It is important to stress that *this is not merely a philosophical question, but an experimentally verified prediction based upon the very foundations of quantum theory itself*. To quote John Wheeler: "No elementary quantum phenomenon is a phenomenon until it is a registered (observed) phenomenon" [8]. Unless a specific observable is actually measured, it really does not exist. This means that we should not *a priori* assume that different ways of probing the system will give the same results, as the *system itself* will change when we change the method of observation.

*To be exact, also the possibility exists of non-local "hidden variable" theories, where objects *do* exist at all times. However, such theories manifestly break Lorentz-covariance.

To exemplify this for the spin of the proton, let us compare two different experimental setups designed to measure it:

i) The Stern-Gerlach (SG) experiment, which uses an inhomogeneous magnetic field to measure the proton spin state;

ii) Deep inelastic scattering (DIS), which uses an elementary probe (electron or neutrino) that inelastically scatters off the "proton" (actually elastically off partons).

We should at once recognize i) and ii) as different, or — in the words of Bohr — "complementary", physical setups. If one measures the first, the other cannot be measured simultaneously, and vice versa. DIS disintegrates the proton and produces "jets" of, often heavier, hadrons as the collision energy is much larger than the binding energy, so there is no proton left to measure. Also, the very fact that the hard reaction in DIS is describable in perturbation theory means that we are dealing with a different quantum mechanical object than an undisturbed proton.

In the case of using a SG apparatus to measure the spin, the proton is intact both before and after the measurement, potential scattering being by definition elastic. SG thus measures the total spin state of the proton, but does not resolve any partons. It therefore seems natural to identify the spin of an undisturbed proton with the result from a Stern-Gerlach type of experiment.

As we have seen, i) and ii) simply do not refer to the same physical system, but the "fundamental spin sum-rule", always assumed to hold in treatments of the spin crisis, explicitly equates the spin of the proton, i), with the sum-total of the measured partonic spins and orbital angular momenta, ii). Instead, it should generally read

$$\frac{\Sigma}{2} + L_q + L_G + \Delta G \neq \frac{1}{2}\,, \tag{1}$$

as the left hand side describes the measured spin of the partons, while the right hand side describes the spin of the proton. (Remember that the left and right hand sides correspond to different physical systems, as defined by the respective *complementary* experimental setups used to measure them.) The quantities above stand for: Σ = fraction of proton's spin

carried by the spin of quarks and anti-quarks, L_q = quark orbital angular momentum contribution, L_G = gluon orbital angular momentum contribution, ΔG = gluon spin contribution.

An additional complication is the following: While in quantum electrodynamics (QED) an atomic wave function can approximately be separated into independent parts due to the weak interaction, and the spins of the constituents (nuclei and electrons) can be measured separately as they can be studied in isolation*, in quantum chromodynamics (QCD) it fails as the interactions between fields in an undisturbed proton are much stronger than in the QED case, making even an approximate separation impossible. Still worse, in QCD at low momentum transfers†, like in an undisturbed proton, the particles "quarks" and "gluons" cannot even be defined [9] and thus do not "exist" within the proton, even when disregarding the quantum mechanical measurement process described above. The simple parton model (with or without orbital angular momenta) is simply not tenable in strong QCD.

However, even if we would assume, as is conventional, that ("clothed") partons within the proton *are* defined, the proton wave function, Ψ, could not be factorized into separate valence quark spin wave functions $(|\chi_1\rangle, |\chi_2\rangle, |\chi_3\rangle)$ as this would not result in an eigenstate of the strongly spin-dependent Hamiltonian, entering the energy eigenvalue equation

$$H\psi_n = E_n\psi_n. \tag{2}$$

The proton wave function could as usual be written as a superposition of energy eigenstates

$$\Psi = \sum_n c_n\psi_n\,, \tag{3}$$

but

$$\Psi^{SG}(\mathbf{x}_1, \mathbf{x}_2, \mathbf{x}_3, s_1, s_2, s_3) \neq u(\mathbf{x}_1, \mathbf{x}_2, \mathbf{x}_3)\,|\chi_1\rangle|\chi_2\rangle|\chi_3\rangle, \tag{4}$$

where s_1, s_2, s_3 encodes the spin-dependence, and $u(\mathbf{x}_1, \mathbf{x}_2, \mathbf{x}_3)$ would be the space-part of a spin-independent system. In reality the quarks would always be correlated and the wave function could never be separated into product states, except as an approximation if the interaction would be sufficiently small, as in DIS

$$\Psi^{DIS}(\mathbf{x}_1, \mathbf{x}_2, \mathbf{x}_3, s_1, s_2, s_3) \simeq u(\mathbf{x}_1, \mathbf{x}_2, \mathbf{x}_3)\,|\chi_1\rangle|\chi_2\rangle|\chi_3\rangle. \tag{5}$$

Note that $\Psi^{SG} \neq \Psi^{DIS}$ as they describe *different* physical systems, defined by their different modes of observation. In SG there would be an intrinsic, unavoidable *interference effect* for the spin (much like in the famous double-slit experiment for position) which is lost when DIS experiments measure spin structure functions of the "proton". The DIS structure functions are proportional to cross sections, which by necessity are classical quantities incapable of encoding quantum interference. As each individual experimental data point is a classical (non-quantum) result, structure functions are by construction related to incoherent sums of individual probability distributions. Thus, even if we (wrongly) would assume the parton model to be applicable in both cases i) and ii), SG would result from adding spin *amplitudes* (taking full account of quantum interference terms), while DIS would result from adding spin *probabilities* (absolute squares of amplitudes). However, we emphasize again that in the case of SG the parton spins are not merely unknown, but actually *undefined*. An experiment like SG probes the spin state of the *proton*, while an experiment like DIS probes the spin state of the *partons* and the final (= observed) system is not a proton at all but "jets" of hadrons. These two experiments are disjoint, or complementary in the words of Bohr, and do *not* describe the same physical object.

In conclusion, we have explained why the "proton" tested by different experimental setups in general *cannot* be considered as the same physical object. Rather, the whole experimental situation must be taken into account, as quantum mechanical objects and observables do not have an objective existence unless measured. We should thus not enforce, by the "spin sum-rule", the same spin (1/2) for the "proton" when measured by DIS as when it is directly measured on the proton as a whole, *e.g.* by SG. The "proton" as measured by deep inelastic scattering is a *different* physical system than a (virtually) undisturbed proton. There is no reason why spin measurements on one should apply to the other. Especially, there is no need for parton spins, as measured by DIS, to add up to the polarized spin of an otherwise undisturbed proton, just like the EMC-experiment [2] and its successors show. On a more pessimistic note, DIS spin data can never directly unravel the spin of the proton because the two are mutually incompatible. At best, DIS can only serve as an indirect test of QCD by supplying asymptotic boundary conditions to be used in future non-perturbative QCD calculations of the proton spin. If the result of those calculations does not come out spin-1/2, QCD is not the correct theory of strong interactions.

Submitted on March 05, 2010 / Accepted on March 08, 2010

*Wigner's classification of particles according to their mass and spin is given by irreducible representations of the Poincaré group, *i.e.* noninteracting fields.

†More precisely, the elementary quanta of QCD are defined only as the momentum transfer goes to infinity.

References

1. Leader E., Anselmino M. *Z. Phys. C*, 1988, v. 41, 239.
2. Ashman J., *et al. Phys. Lett. B*, 1988, v. 206, 364; *Nucl. Phys. B*, 1989, v. 328, 1.
3. Gell-Mann M. *Phys. Lett.*, 1964, v. 8, 214.
4. Zweig G. *CERN reports*, TH-401, TH-412, 1964.
5. Bell J. S. *Physics*, 1964, v. 1, 195.
6. Freedman S. J., Clauser J. F. *Phys. Rev. Lett.*, 1972, v. 28, 938.
7. Aspect A., Dalibard J., Roger G. *Phys. Rev. Lett.*, 1982, v. 49, 91; 1804.
8. In preface to *The Quantum Theory of Measurement*, Eds. Wheeler J. A. and Zurek W. H., Princeton University Press, New Jersey, 1983.
9. Hansson J. *Can. J. Phys.*, 2002, v. 80, 1093.

Is the Field of Numbers a Real Physical Field? On the Frequent Distribution and Masses of the Elementary Particles

Anatoly V. Belyakov
E-mail: belyakov.lih@gmail.com

Frequent distributions of the databases of the numerical values obtained by resolving algorithms, which describe physical and other processes, give a possibility for bonding the probability of that results the algorithms get. In the frequent distribution of the *fractions* of integers (rational numbers), local maxima which meet the ratios of masses of the elementary particles have been found.

Consider a general case of an arbitrary function $F(x, y, z, \dots)$. Take under consideration a region of the values of this function, split into numerous intervals. Filling up the intervals by item-by-item examination of the possible numerical values of the parameters $x, y, z, \dots$, expressed with integers, will be non-uniform.

Any algorithm has its own individual *frequent distribution*. The distributions can be created* for any formula, which has two or more free parameters (the distributions of the parameters can sometimes have unexpected or complicate form, containing both minima and peaks of the probability).

Frequent distributions give a possibility for bonding the probability of the appearance of numerical values of a function in the region of its existence. This is because the number of the numerical values of the function, hitting into a respective interval, in by item-by-item examination of the possible numerical values of the function's arguments, is proportional to the probability of an average numerical value of the function in the interval. The frequent distributions manifest the reproductivity of numerical values of the function due to the possible variations of its arguments. A frequent distribution itself cannot provide exact numerical solutions. However, if the object or process under consideration is described by not a single function but a few ones, the frequent distributions of these functions can logically be summarized or multiplied in order to manifest, more clear, such regions wherein the probability is high to that in the rest regions. Form of the distribution depends on both the form of the function and the dependencies among the positive integers; in the distribution obtained as above, the properties of the integers become not limited by the plain function of their item-by-item examination, but are more complicate thus an *individualization* of the integers occurs.

Once sharp manifested maxima, attractors, or regions of zero probability appear, it is important to find what peculiarities the algorithm bears. This however can be done only through respective analysis of a large number of the calculation results. In early years, this problem was unable to be considered in serious: processing so large numerical databases, and enforced extracting the probability from chaos, require huge time of routine job; therefore this job became accessed only due to the computer techniques.

It should be noted that the discrete nature of experimental results was discovered in the background of normal distribution of their numerical values (fine structure of the histograms) in already many years ago, by experimental studies conducted, commencing in 1951, by Simon E. Shnoll and his experimental team (see his monograph [1] and bibliography therein). As a result, Shnoll suggested that form of the histograms is connected with the mathematical algorithms, which express the respective processes we measure.

Below are specific examples, which illustrate the connexion of the frequent distributions and the real physical processes and phenomena.

There is a very interesting property of the frequent distributions: several kinds of the distributions include the *ratios of masses of the elementary particles*. This property is attributed to the frequent distributions of the databases of numerical values of the functions, constructed on *fractions*. We found these are plain exponential functions $A^{x/y}$, where A is presented by special numbers $\pi = 3.1416\dots$, $e = 2.17183\dots$, and the reverse fine structure constant $\alpha = 137.036\dots$ In a few cases (hyperons), we mean A the relative mass of the proton $m_p/m_e = 1836$.

In order to be sure in it, we should do follows. Collect a database of numerical values of such a function in the framework of the complete item-by-item examination of its arguments x and y presented by integers, and in the scale which is enough large for covering the necessary scale of masses of the elementary particles (in the units of mass of the electron). Then we should distribute the numerical values along the axis of abscissas, covering numerous intervals by them. Once the distribution done, we will see that it has local maxima (peaks) in numerous locations of the scale, which meet the numerical values of masses of the elementary particles. Peaks of the distributions have a delta-like form.

Distributions of fractions along the numerical axis are self-similar. They reproduce themselves in the peaks of the first, the second and higher orders upto most small segments of the scale. It is possible to see that there is a fractal struc-

*There is a ready-to-use function "frequency" in MS Excel; another software can be applied as well.

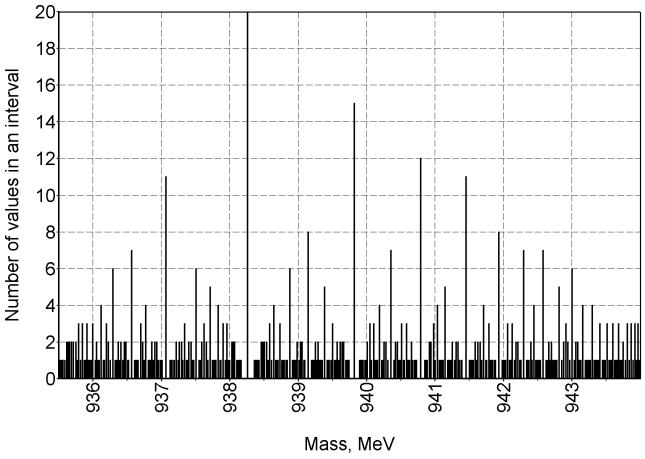

Fig. 1: Mass of the proton (938.27) in distribution $0.511\,\pi^{x/y}$.

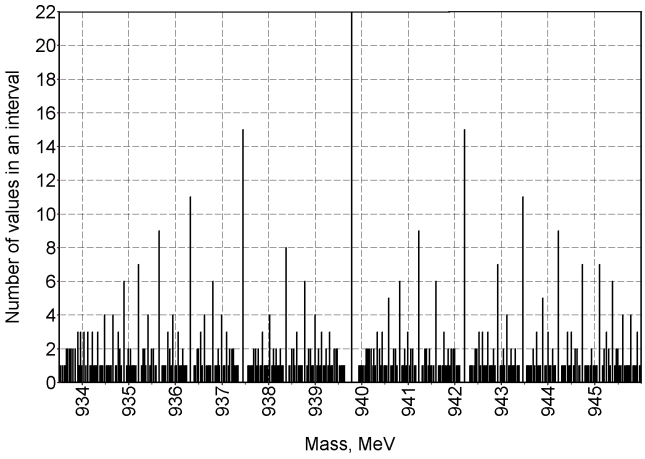

Fig. 2: Mass of the neutron (939.57) in distribution $0.511\,a^{x/y}$.

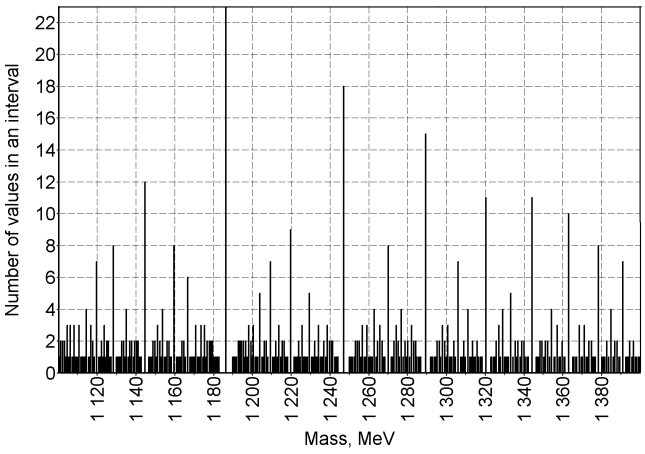

Fig. 3: Mass of the Σ^+ (1189) particle in distribution $0.511\,e^{x/y}$.

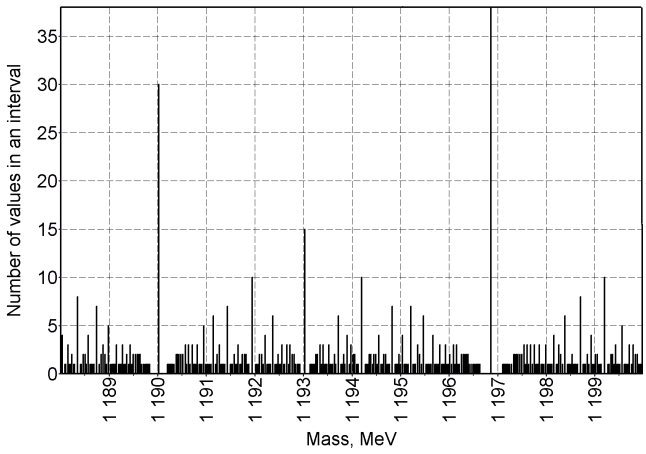

Fig. 4: Masses of the Σ^+ (1189.4), Σ^0 (1192.5), Σ^- (1197.3) particles in distribution $0.511\,a^{x/y}$.

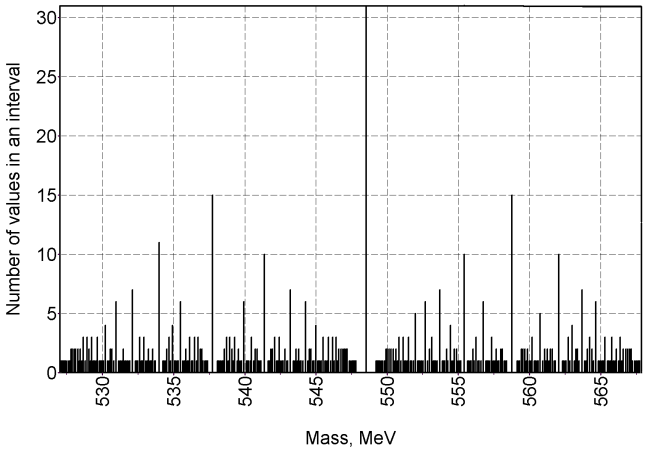

Fig. 5: Mass of the η (548.8) particle in $0.511\,(m_p/m_e)^{x/y}$ distribution.

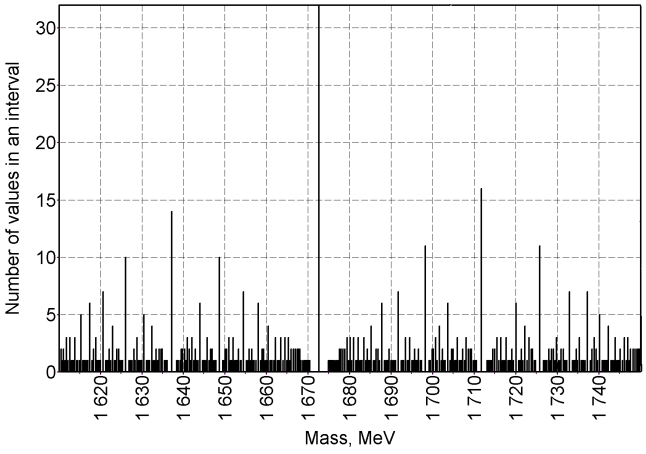

Fig. 6: Masses of the Ω^-, Σ_1 (1672, 1670) particles in distribution $0.511\,(m_p/m_e)^{x/y}$.

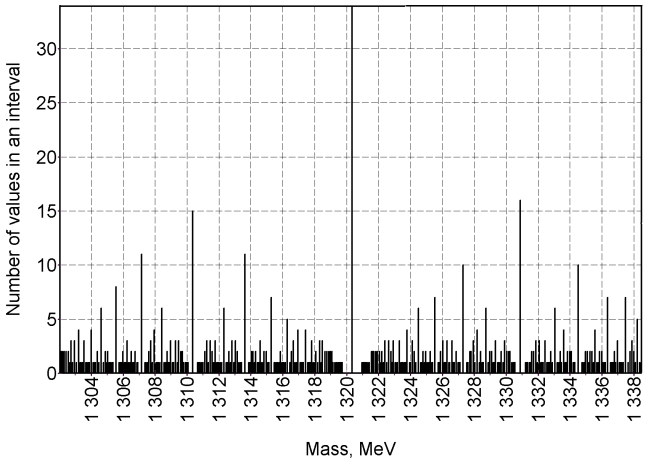

Fig. 7: Mass of the Ξ^-- (1321) particle in 0.511 $(m_p/m_e)^{x/y}$ distribution.

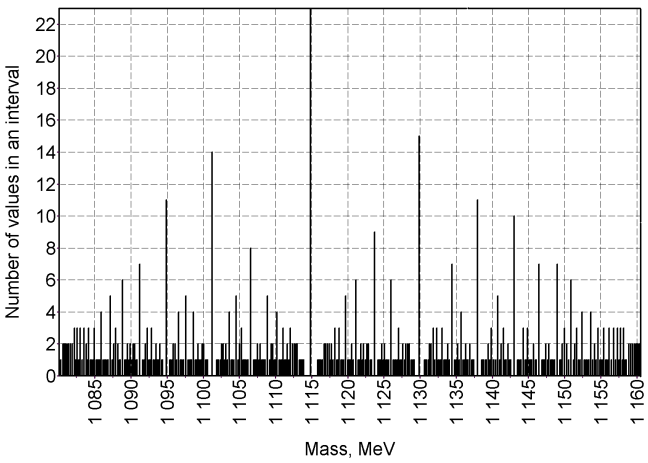

Fig. 8: Mass of the Λ (1115) particle in distribution 0.511 $a^{x/y}$.

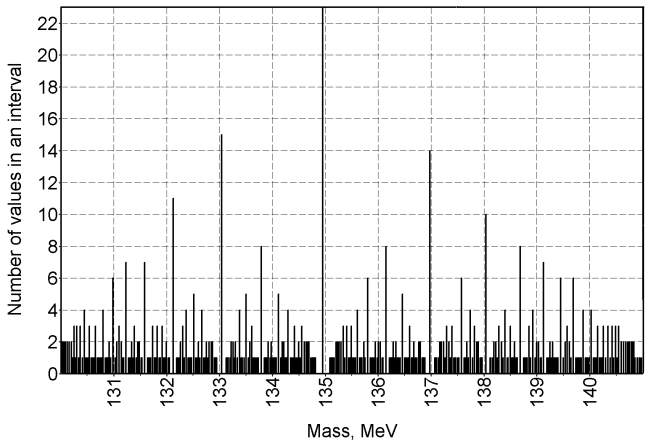

Fig. 9: Mass of the π^0 (134.9) particle in distribution 0.511 $a^{x/y}$.

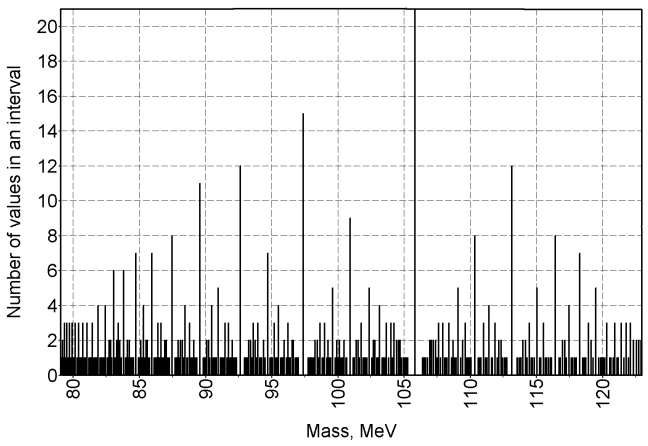

Fig. 10: Mass of the μ^- (105.7) particle in distribution 0.511 $e^{x/y}$.

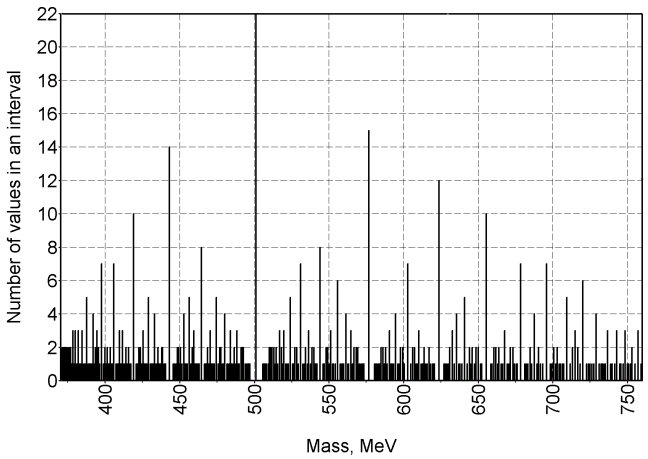

Fig. 11: Mass of the K^0 (498.7) particle in distribution 0.511 $a^{x/y}$.

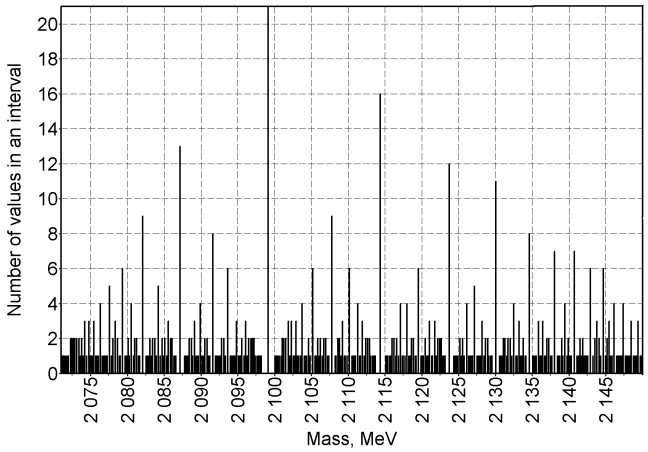

Fig. 12: Mass of the Λ_4 (2100) particle in 0.511 $(m_p/m_e)^{x/y}$ distribution.

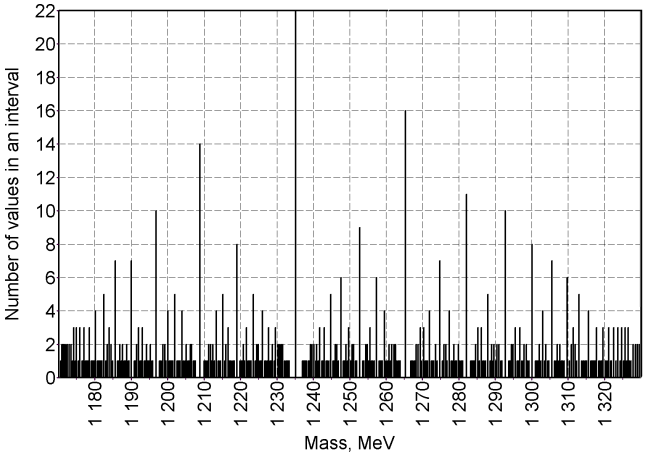

Fig. 13: Masses of the b_1^0, Δ_1 (1233, 1232) particles in distribution $0.511\,a^{x/y}$.

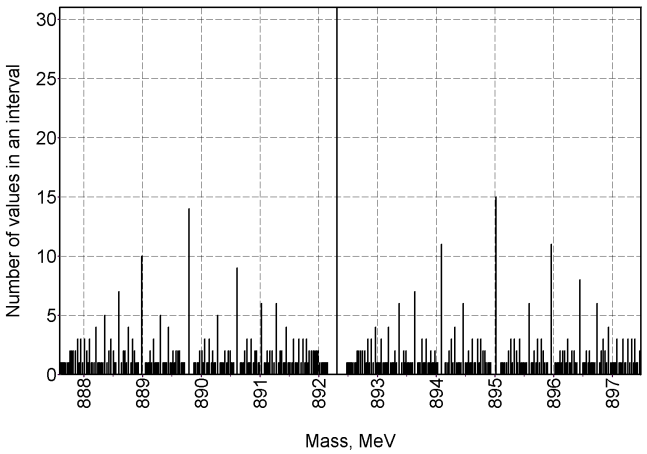

Fig. 14: Mass of the K^* (892.2) particle in distribution $0.511\,a^{x/y}$.

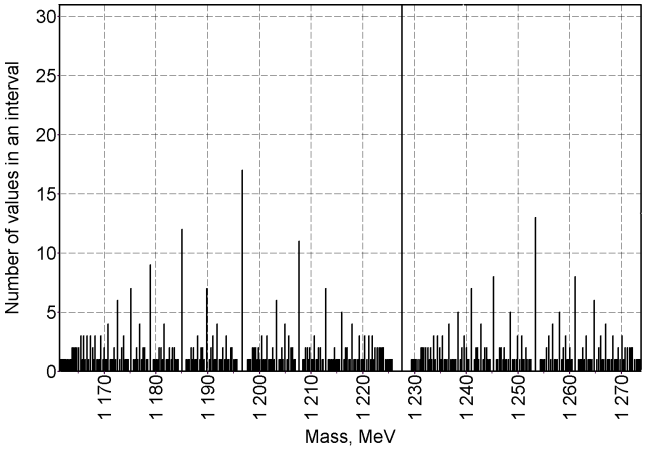

Fig. 15: Mass of the B (1230) particle in distribution $0.511\,\pi^{x/y}$.

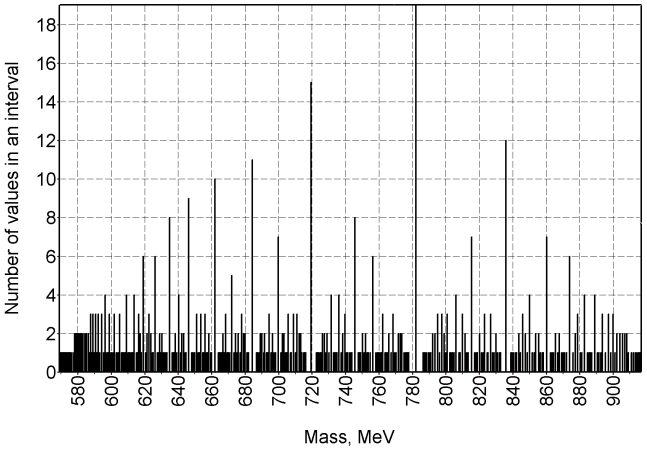

Fig. 16: Mass of the ω (782.7) particle in distribution $0.511\,e^{x/y}$.

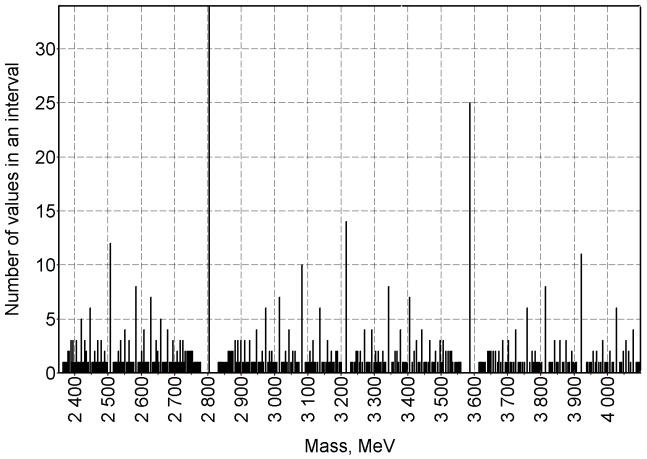

Fig. 17: Masses of the η_c (2820), χ (3556) particles in distribution $0.511\,a^{x/y}$.

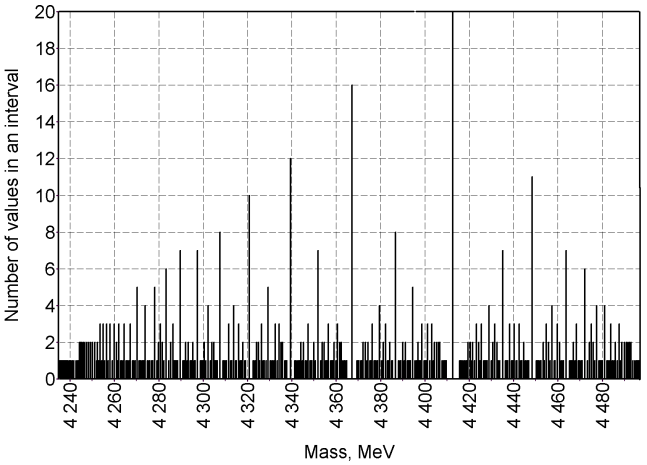

Fig. 18: Mass of the ψ''' (4414) particle in distribution $0.511\,a^{x/y}$.

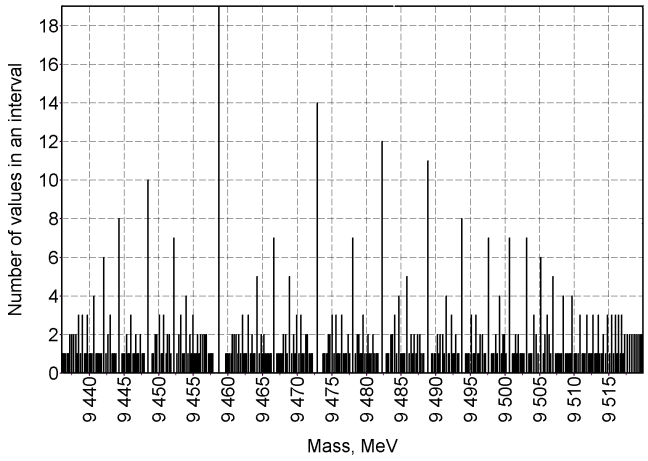

Fig. 19: Mass of the Y (9460) particle in distribution 0.511 $e^{x/y}$.

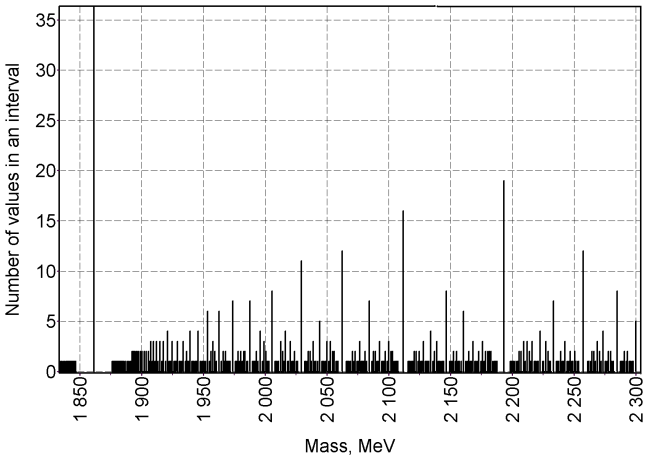

Fig. 20: Some main peaks correspond with masses of the D^0 (1863), D^{*0} (2006), Σ_3 (2030), N_4 (2190), Λ_c^+ (2260) particles in distribution 0.511 $a^{x/y}$.

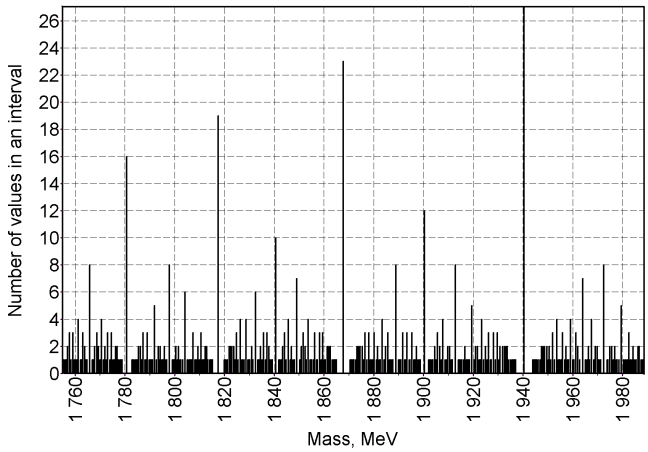

Fig. 21: Main peaks correspond with masses of the τ^- (1782), Λ_3, Ξ_1 (1820, 1820), D^+ (1868), S (1940) particles in distribution 0.511 $\pi^{x/y}$.

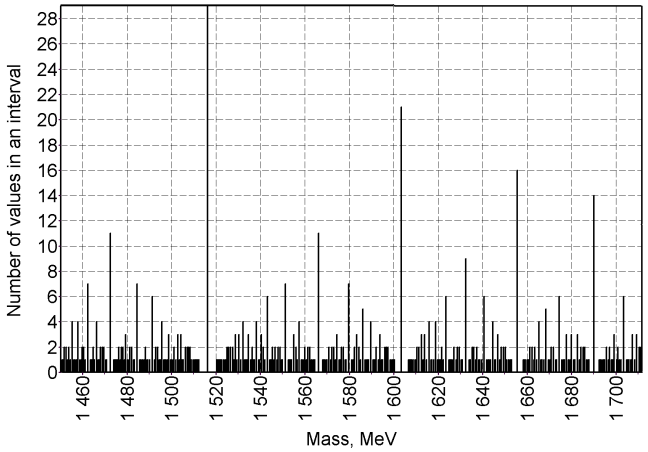

Fig. 22: Main peaks correspond with masses of the f′, Λ_2, N_2 (1516, 1518, 1520), ρ' (1600), Δ_2 (1650), N_3, g (1688, 1690) particles in distribution 0.511 $a^{x/y}$.

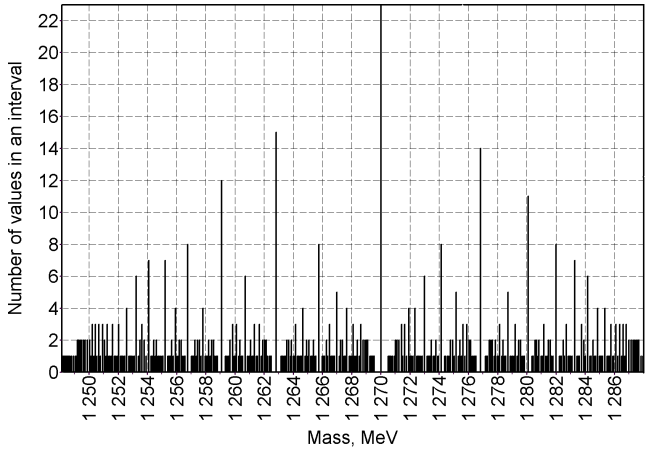

Fig. 23: Mass of the f (1270) particle in distribution 0.511 $e^{x/y}$.

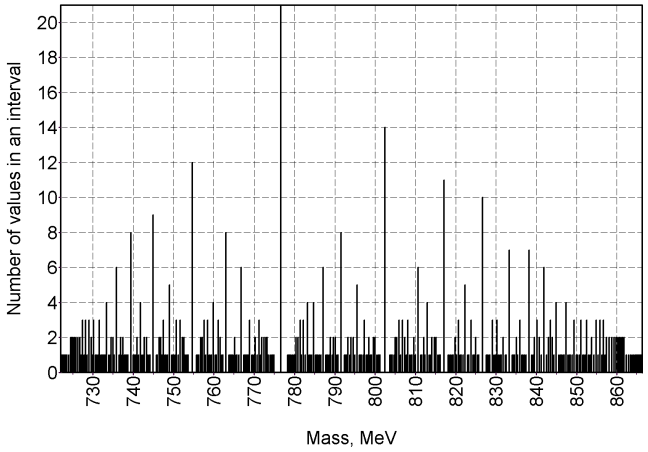

Fig. 24: Mass of the ρ (773) particle in distribution 0.511 $\pi^{x/y}$.

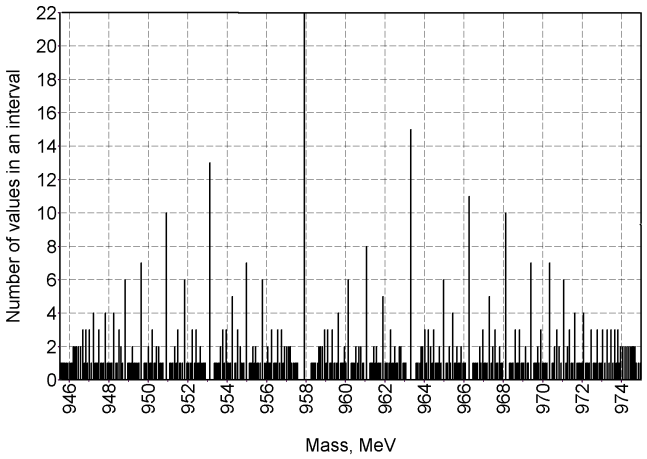

Fig. 25: Mass of the η' (958) particle in distribution 0.511 $\pi^{x/y}$.

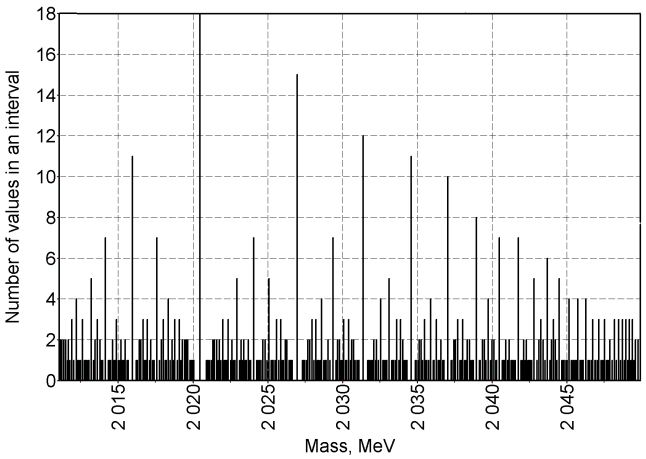

Fig. 26: Mass of the h (2020) particle in distribution 0.511 $\pi^{x/y}$.

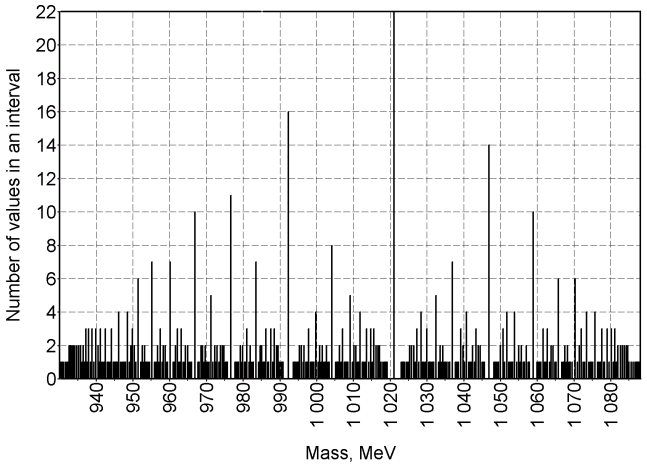

Fig. 27: Mass of the φ (1020) particle in distribution 0.511 $e^{x/y}$.

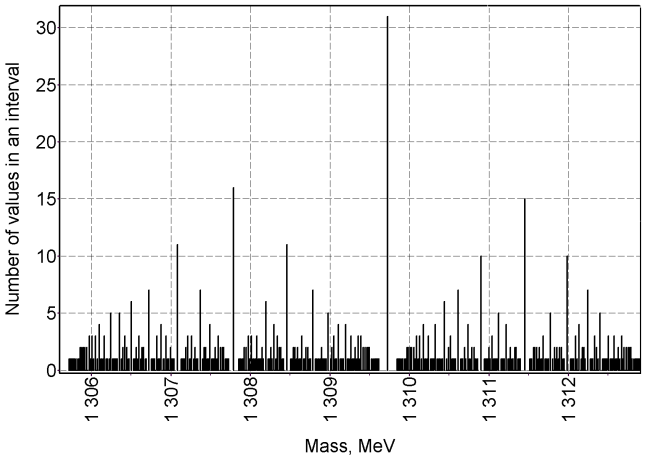

Fig. 28: Mass of the A (1310) particle in distribution 0.511 $a^{x/y}$.

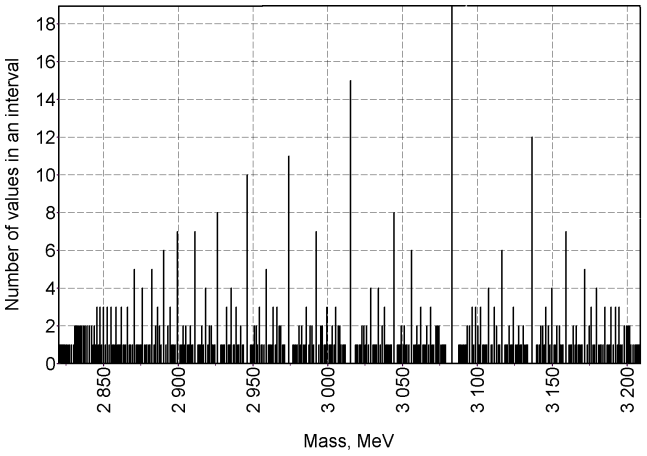

Fig. 29: Mass of the J/ψ (3096) particle in distribution 0.511 $a^{x/y}$.

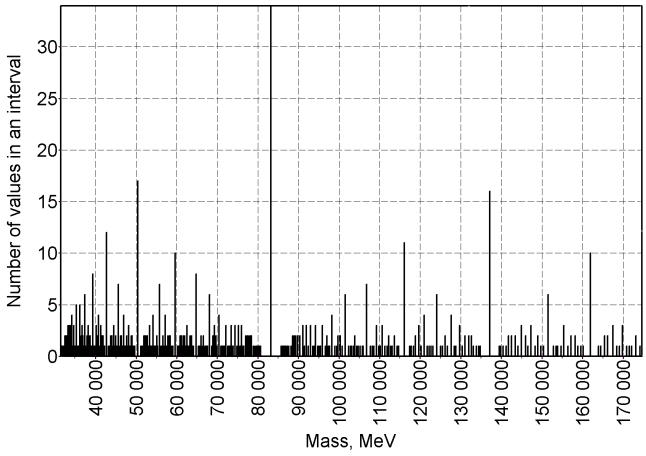

Fig. 30: Mass of the W (82000) particle in distribution 0.511 $e^{x/y}$.

ture of the distribution, when compressing the scale of the diagram by respective changing the variations by x and y (with the same number of the interval unchanged). Therefore, generally speaking, any arbitrary numerical value of the mass could meet, in the diagram, a peak of the first or higher orders. An objective criterion can be a relative error of the calculation, which is the ratio of the error of our calculation by the length of the respective local interval (or the distance between the peaks of the same order; the peak heights differ from each other as seen in Fig. 21 and Fig. 22). I checked about 50 numerical values of the masses; the relative error of the calculation was under a few percents only.

Figures 1–30 show specific examples of my calculations: these are frequent distributions, local maxima of which meet the relative masses of very different particles. The axis of abscissas is given in MeV. The histograms are created in the same way; they have 1000 numerical values distributed along 350 intervals.

It is probable, all the masses meet respective peaks in the distributions. This is not a result of my "passion" to numerology. This also does not mean that the masses of the particles are expressed just by the same functions. Meanwhile, these correspondences appear with so high precision and so often that they cannot be random, absolutely. On the other hand, the numerical values of some masses meet not the peaks, whose height is proportional to the number of the pairs x and y producing the same fraction, but empty spaces neighbouring the peaks (the spaces are presented by most rare appeared ratios of the prime numbers). As is obvious, the empty space neighbouring the peaks manifest minima of the relative density of rational numbers in their distribution along the numerical axis. Connexion of the spaces with the most stable states of oscillation processes was shown by Kyril I. Dombrowski [2, 3].

Is there a spectrum of masses of the elementary particles, if we mean it as the presence of the cross-dependency of the masses, and a possible algorithm of their calculation? I think that not. This is despite we can suppose that the numerical values of the masses constitute the "fine structure" of a distribution according to an unknown algorithm.

It is likely as the numerical values of the masses have a probabilistic origin, and are connected somehow with the properties of the prime numbers. It is probable, a rôle is played here by the fact that the prime number fractions or ratios are more fundamental quantities than the prime numbers themselves. This is because each single fraction of the infinite row is a result of ratios of infinite number of the pairs of arbitrary prime numbers.

At present time, many elementary particles were experimentally discovered. The particles have very different lifespans. This fact and also the shape of distributions constructed on fractions lead us to a conclusion that the first order masses "create" the second order masses, the second order masses "create" the third order masses, and so on to infinity. Such a process is specific to a continuous non-viscous medium, when perturbations appear in it. We cannot except that physical experiments can produce infinite variety of the elementary particles.

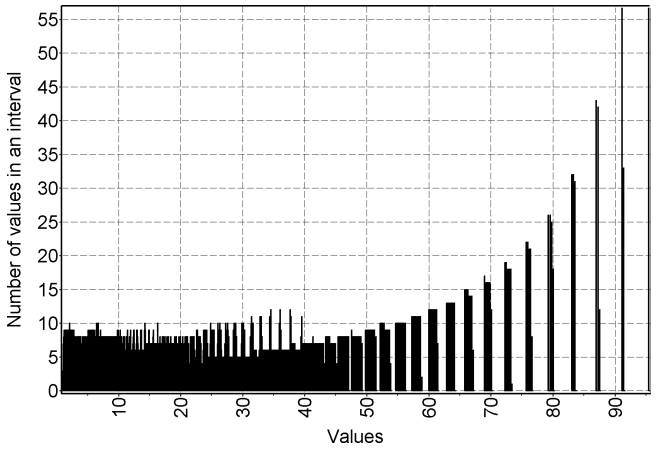

Fig. 31: Distribution on the function $100 \exp\left(-ax(b-y)^{0.5}\right)$, where $a = 0.00147$, $b = 1000$.

Another example is provided by frequent distribution of the exponent (Fig. 31)

$$100 \exp\left(-ax(b-y)^{0.5}\right),$$

modelling the well-known formula which expresses the transparency of the potential barrier of the tunnelling effect, where x and y are variables characterizing mass and energy of the particle. Shape of the distribution is very dependent on the numerical coefficients a and b. Moreover, several numerical values of the function are not realized at all. This form of histograms is specific to those functions, which do not contain ratios or fractions.

In this case, in item-by-item examination of the integers x and y along an abstract scale from 1 to 100, there is about 10,000 numerical values of the exponent. The axis of ordinates means the number of the coinciding numerical values of the function along the interval.

As we found, the distribution of the exponent has the most number of the intervals (nonzero numerical values of the ordinate, whose common number is as well dependent also on the given length of the unit interval) with several specific numerical values a and b. For instance, Fig. 31. With $b = 1000$ and $a = 0.00147$, difference between the neighboring intervals (i.e. the relative length of the interval) is 0.003 of the current numerical value f the function, while this is in the background of 1124 nonzero intervals (the graph has 10,000 intervals totally).

With these parameters, the term under the exponent approaches numerically to -1 independent from the "size" of the database. On the other hand, the *tunnelling effect* appears with the *same condition* in an analogous physical formula! I also attempted to employ frequent distributions in order to

explain the most brighty lines of the radiation spectra for different kinds of radiation [4].

Thus I suggest that, aside for the known physical fields, the field of the positive integers exists as a physical field of the Nature. Pattern of this field has concentrations (peaks) and rarefractions of integers, which determine special numbers such as e, π, and, probable, the fundamental physical constants (the fine structure constant, the gravitational constant, and the others). Physical phenomena process in the inhomogeneous background of this field; any function using the field of integers (database of integers) produces surfs of probability in it (a relative analogy). We should not except that the stable orbits of the cosmic bodies originate from the probabilistic frequent distributions in the gravitational field (the field of the gravitational potential) of the attracting masses they orbit.

It is obvious that the discrete distributions of experimental data, and also their connexion with the aforementioned frequent distributions, are true for the microscales in the first row. There in the microscales, physical quantities exist in the boundary of their decay, thus the possibility of this solution is due to the discrete origin of physical phenomena, which is manifested in the microscales very much. On the other hand, our conclusion are most probable true for a general case as well: non-prime numbers can be represented as the ratios of primes, so the aforementioned frequent distributions are still true for even smallest intervals.

Are we lawful to claim that the parameters of physical or other processes, which are described as above, have not only the quantitative expression but also the probabilistic expression as just said before?

Should we, within the given dependencies which describe some processes or phenomena, find out a possibility for the prediction of the regions of the most probable solutions as those most rational to the others, or for the prediction of those intervals of numerical values, where the considered phenomenon processes most intense (all these not only in the microscales)?

If so, we get a possibility for solving the reverse problems, which target re-construction of the probabilistic distribution of the primary experimental results on the basis of a respective algorithm. This is related first of all to those problems, which are based on the discrete data (primes). This is, for instance, industry or economics: the number of working sections, workgroups, units of equipment, produced units, the number of working personell, and so on.

If all that has been said above is true, and the results of solving similar algorithms (in the case where the algorithms are expressed by the functions whose arguments are more than two) can bear not only a numerical meaning but also a probabilistic meaning, this fact leads to important sequels. There are many problems where numerous parameters are unknown, or cannot be determined in exact. This is economics, game theory, military, meteorology, and many others. In such a case, given a respective algorithm, we could replace the unknown parameters in it with the numbers taken in the respective interval then create frequent distributions thus obtaining probabilistic solutions. Experimental tests are needed in this direction.

Finally, I would like to attract attention of physicists to this problem surveyed here. As is probable, this problem draws that dialectic boundary where chaos meets order, and chance meets regularity.

Submitted on February 14, 2010 / Accepted on February 18, 2010

References

1. Shnoll S. E. Cosmic physical factors in random processes. Svenska fysikarkivet, Stockholm, 2009, 388 pages.
2. Dombrowski K. I. *Bulletin of Soviet Atron. Geodesical Society*, 1956, no. 17(24), 46–50.
3. Dombrowski K. I. Rational numbers distribution and resonance. *Progress in Physics*, 2005, v. 1, 65–67.
4. Belyakov A. V. Geometrodynamics and elements of the matrix calculus of spectra. *Proceedings of Vladimir State Teacher University, the Scientific Didactic Journal*, 2002, no. 7, 29–37 (*in Russian*).

Fractal Scaling Models of Natural Oscillations in Chain Systems and the Mass Distribution of Particles

Hartmut Müller

Global Scaling Research Institute in memoriam Leonhard Euler, Munich, Germany. E-mail: info@globalscaling.de

The paper presents a fractal scaling model of a chain system of quantum harmonic oscillators, that reproduces some systematic features in the mass distribution of hadrons, leptons and gauge bosons.

1 Introduction

The origin of particle masses is one of the most important unsolved problems of modern physics. Also the discrete character of the distribution of particle masses is untreated. In this paper we won't discuss the current situation in the standard theory. Based on a fractal scaling model [1] of natural oscillations in chain systems of harmonic quantum oscillators we will analyze the distributions of particles in dependence on their masses to find out systematic features.

Fractal scaling models [2] of natural oscillations are not based on any statements about the nature of the link or interaction between the elements of the oscillating chain system. Therefore the model statements are quite generally, what opens a wide field of possible applications. Logarithmic scaling is a well known property of inclusive distributions in high energy particle reactions [3]. The quantity of secondary particles increases in dependence on the logarithm of the collision energy.

In the framework of the standard theory, the electron is stable because it's the least massive particle with non-zero electric charge. Its decay would violate charge conservation. The proton is stable, because it's the lightest baryon and the baryon number is conserved. Therefore the proton is the most important baryon, while the electron is the most important lepton and the proton-to-electron mass ratio can be understood as a fundamental physical constant. In the framework of the standard theory, the W- and Z-bosons are elementary particles that mediate the weak force. The rest masses of all theses particles are measured with high precision. The masses of other elementary or stable particles (quarks, neutrinos) are unknown.

In the framework of our model [1], particles are resonance states in chain systems of harmonic quantum oscillators and the masses of fundamental particles are connected by the scaling exponent $\frac{3}{2}$. For example, the proton-to-electron mass ratio is $7\frac{1}{2}$, but the W-boson-to-proton mass ratio is $4\frac{1}{2}$. This means, they are connected by the equation:

$$\ln\left(\frac{m_w}{m_p}\right) = \ln\left(\frac{m_p}{m_e}\right) - 3\,. \tag{1}$$

Therefore the W-boson-to-electron mass ratio corresponds to $4\frac{1}{2} + 7\frac{1}{2} = 12$:

$$\ln\left(\frac{m_w}{m_e}\right) = 12. \tag{2}$$

Already within the eighties the scaling exponent $\frac{3}{2}$ was found in the distribution of particle masses by Valery A. Kolombet [4]. In addition, we have shown [2] that the masses of the most massive celestial bodies in the Solar System are connected by the same scaling exponent $\frac{3}{2}$. The scaling exponent $\frac{3}{2}$ arises as consequence of natural oscillations in chain systems of similar harmonic oscillators [1]. If the natural frequency of one harmonic oscillator is known, one can calculate the complete fractal spectrum of natural frequencies of the chain system, in which spectral nodes arise on the distance of 1 and $\frac{1}{2}$ logarithmic units.

Near spectral nodes the spectral density reaches local maximum and natural frequencies are distributed maximum densely. The energy efficiency of natural oscillations is very high. Therefore one can expect that spectral nodes represent states of the oscillating chain system, which have the highest degree of effectiveness. For this reason we suspect, that stable particles correspond to main spectral nodes.

2 Methods

Based on the continued fraction method [5] we will search the natural frequencies of a chain system of many similar harmonic oscillators in this form:

$$f_{jk} = f_{00} \exp\left(S_{jk}\right). \tag{3}$$

f_{jk} is a set of natural frequencies of a chain system of similar harmonic oscillators, f_{00} is the natural oscillation frequency of one oscillator, S_{jk} is a set of finite continued fractions with integer elements:

$$S_{jk} = n_{j0} + \cfrac{1}{n_{j1} + \cfrac{1}{n_{j2} + \ddots + \cfrac{1}{n_{jk}}}} = [n_{j0}; n_{j1}, n_{j2}, \ldots, n_{jk}]\,, \tag{4}$$

where $n_{j0}, n_{j1}, n_{j2}, \ldots, n_{jk} \in Z$, $j = 0\,, \infty$. We investigate continued fractions (4) with a finite quantity of layers k, which generate discrete spectra, because in this case all S_{jk} represent rational numbers. Therefore the free links n_{j0} and the partial denominators $n_{j1}, n_{j2}, \ldots, n_{jk}$ can be interpreted as "quantum

Particle	Rest mass m, MeV/c^2 [6]	$\ln(m/m_{00})$	S	d
electron (m_{00})	0.510998910 ± 0.000000013	0	[0]	0.000
proton	938.27203 ± 0.00008	7.515	[7; 2]	0.015
neutron	939.565346 ± 0.000023	7.517	[7; 2]	0.017
W-boson	80398 ± 25	11,966	[12]	−0.034
Z-boson	91187.6 ± 2.1	12.092	[12]	0,092

Table 1: The rest masses of well measured stable and fundamental particles and the S-values (4) of the nearest main spectral nodes for the electron calibrated model spectrum. The deviation $d = (\ln(m/m_{00}) - S)$ is indicated.

numbers". The present paper follows the Terskich [5] definition of a chain system, where the interaction between the elements proceeds only in their movement direction. Model spectra (4) are not only logarithmic-invariant, but also fractal, because the discrete hyperbolic distribution of natural frequencies f_{jk} repeats itself on each spectral layer. The partial denominators run through positive and negative integer values. Ranges of relative low spectral density (spectral gaps) and ranges of relative high spectral density (spectral nodes) arise on each spectral layer. In addition to the first spectral layer, Fig. 1 shows the second spectral layer $k = 2$ with $|n_{j1}| = 2$ (logarithmic representation). Maximum spectral density areas (spectral nodes) arise automatically on the distance of integer and half logarithmic units.

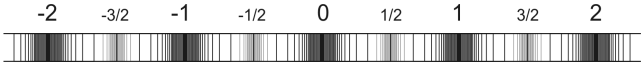

Fig. 1: The spectrum (4) on the first layer $k = 1$, for $|n_{j0}| = 0,\ 1\ 2, \ldots$ and $|n_{j1}| = 2,\ 3,\ 4, \ldots$ and, in addition, the second spectral layer $k = 2$, with $|n_{j1}| = 2$ and $|n_{j2}| = 2,\ 3,\ 4, \ldots$ (logarithmic representation).

Fractal scaling models of natural oscillations are not based on any statements about the nature of the link or interaction between the elements of the oscillating chain system. For this reason we assume that our model could be useful also for the analysis of natural oscillations in chain systems of harmonic quantum oscillators. We assume that in the case of natural oscillations the amplitudes are low, the oscillations are harmonic and the oscillation energy E depends only on the frequency (h is the Planck constant):

$$E = hf\,. \tag{5}$$

In the framework of our model (3) all particles are resonances, in which to the oscillation energy (5) corresponds the particle mass m:

$$m = f\frac{h}{c^2}\,. \tag{6}$$

In this connection the equation (6) means that quantum oscillations generate mass. Under consideration of (3) now we can create a fractal scaling model of the mass spectrum of model particles. This mass spectrum is described by the same continued fraction (4), for $m_{00} = f_{00}\frac{h}{c^2}$:

$$\ln\left(\frac{m_{jk}}{m_{00}}\right) = [n_{j0}; n_{j1}, n_{j2}, \ldots, n_{jk}]\,. \tag{7}$$

The frequency spectrum (4) and the mass spectrum (7) are isomorphic. The mass spectrum (7) is fractal and consequently it has a clear hierarchical structure, in which continued fractions (4) of the form $[n_{j0}]$ and $[n_{j0}; 2]$ define main spectral nodes, as Fig. 1 shows.

3 Results

In the present paper we will compare the scaling model mass spectrum (7) in the range of 100 KeV/c^2 to 100 GeV/c^2 with the mass distribution of well-known particles — hadrons, leptons and gauge bosons.

The model mass spectrum (7) is logarithmically symmetrical and the main spectral nodes arise on the distance of 1 and $\frac{1}{2}$ logarithmic units, as fig. 1 shows. The mass m_{00} in (7) corresponds to the main spectral node $S_{00} = [0]$, because $\ln(m_{00}/m_{00}) = 0$. Let's assume that m_{00} is the electron rest mass 0.510998910(13) MeV/c^2 [6]. In this case (7) describes the mass spectrum that corresponds to the natural frequency spectrum (4) of a chain system of vibrating electrons. Further stable or fundamental model particles correspond to further main spectral nodes of the form $[n_{j0}]$ and $[n_{j0}; 2]$. Actually, near the node [12] we find the W- and Z-bosons, but near the node [7; 2] the proton and neutron masses, as Table 1 shows.

Theoretically, a chain system of vibrating protons generates the same spectrum (7). Also in this case, stable or fundamental model particles correspond to main spectral nodes of the form $[n_{j0}]$ and $[n_{j0}; 2]$, but relative to the electron calibrated spectrum, they are moved by $-7\frac{1}{2}$ logarithmic units. Actually, if m_{00} is the proton rest mass 938.27203(8) MeV/c^2 [6], then the electron corresponds to the node $[-7; -2]$, but the W- and Z-bosons correspond to node [4; 2].

Consequently, the core claims of our model don't depend on the selection of the calibration mass m_{00}, if it is the rest mass of a fundamental resonance state that corresponds to a main spectral node. As mentioned already, this is why the model spectrum (7) is logarithmically symmetrical.

Because a chain system of any similar harmonic oscillators generates the spectrum (7), m_{00} can be much more smaller than the electron mass. Only one condition has to be fulfilled: m_{00} has to correspond to a main spectral node of the model spectrum (7). On this background all particles

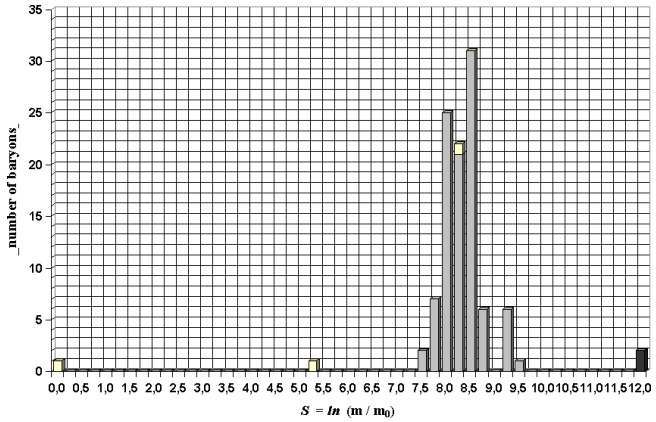

Fig. 2: This histogram was built based on Table 2 and shows the distribution of baryons (grey bars) and leptons (white bars) over $\frac{1}{4}$ logarithmic units wide S-intervals in the range of the electron mass ($S = 0$, white bar) to the W- and Z-bosons ($S = 12$, black bar).

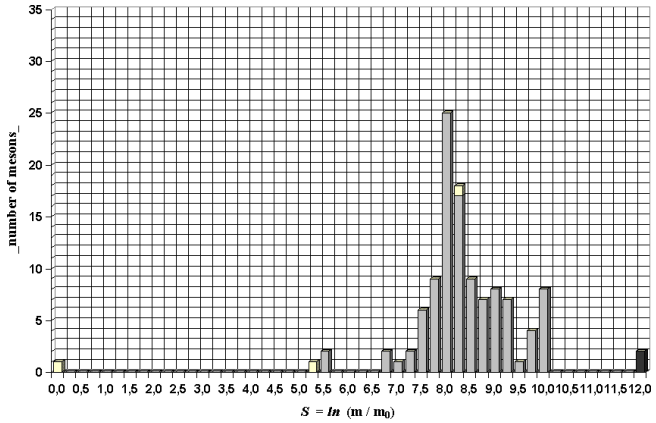

Fig. 3: This histogram was built based on Table 3 and shows the distribution of mesons (grey bars) and leptons (white bars) over $\frac{1}{4}$ logarithmic units wide S-intervals in the range of the electron mass ($S = 0$, white bar) to the W- and Z-bosons ($S = 12$, black bar).

can be interpreted as resonance states in a chain system of harmonic quantum oscillators, in which the rest mass of each single oscillator goes to zero. In the framework of our oscillation model this way can be understood the transition of massless to massive states.

In our model massive particles don't arise because of a symmetry violation. Massive particles arise as resonance states and their mass distribution is logarithmically symmetric.

Further we will investigate the distribution of hadrons (baryons and mesons) in dependence on their rest masses. For this we will split up the mass spectrum (7) into equal in size logarithmic intervals and build histograms. To separate clear the main spectral nodes $[n_{j0}]$ and $[n_{j0}; 2]$, we have to split up the spectrum (7) into S-intervals of $\frac{1}{4}$ logarithmic units.

Table 2 shows the measured masses of baryons, the calculated S-intervals of $\frac{1}{4}$ logarithmic units width and the corresponding calculated mass-intervals. Based on Table 2 a histogram was built (Fig. 2) that shows the distribution of baryons over the $\frac{1}{4}$ logarithmic S-intervals. Based on Table 3,

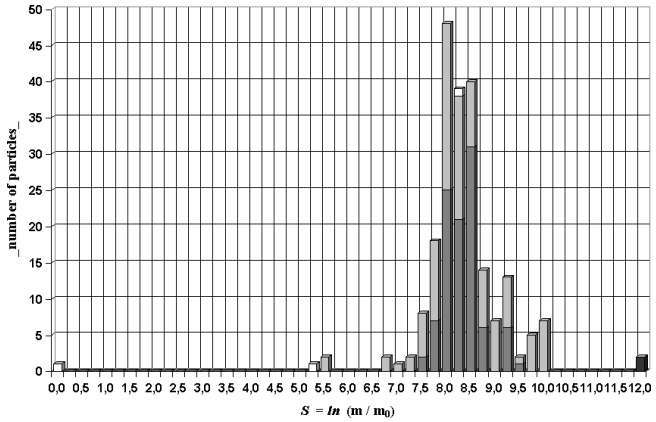

Fig. 4: This histogram was built based on tables 2, 3, 4, 5 and shows the distribution of baryons (dark grey bars), mesons (light grey bars) and leptons (white bars) over $\frac{1}{4}$ logarithmic units wide S-intervals in the range of the electron mass ($S = 0$, white bar) to the W- and Z-bosons ($S = 12$, black bar).

Figure 3 shows the distribution of mesons, but Figure 4 shows the distribution of baryons, mesons, leptons and gauge bosons over the $\frac{1}{4}$ logarithmic S-intervals in the range of 0 to 12 logarithmic units.

All known baryons are distributed over an interval of 2 logarithmic units, of $S = [7; 2]$ to $S = [9; 2]$, as Figure 2 shows. Maximum of baryons occupy the logarithmic center $S = [8; 2]$ of this interval. Figure 3 shows that maximum of mesons occupy the spectral node $S = [8]$ that split up the interval of $S = [0]$ to $S = [12]$ between the electron and the W- and Z-bosons proportionally of $\frac{2}{3}$.

The mass distribution of leptons isn't different of the baryon and meson mass distributions, but follows them, as Figure 4 shows. The mass of the most massive lepton (tauon) is near the maximum of the baryon and meson mass distributions, as Figures 2–4 show.

4 Resume

In the framework of the present model discrete scaling mass distributions arise as result of natural oscillations in chain systems of harmonic quantum oscillators. The observable mass distributions of baryons, mesons, leptons and gauge bosons are connected by the model scaling exponent $\frac{2}{3}$. In addition, with high precision, the masses of known fundamental and stable particles are connected by the model scaling exponent $\frac{3}{2}$. Presumably, the complete mass distribution of particles is logarithmically symmetric and, possibly, massive particles don't arise because of a symmetry violation, but as resonance states in chain systems of quantum oscillators.

Acknowledgements

The author is deeply grateful to S. E. Shnoll, V. A. Panchelyuga and V. A Kolombet for valuable discussions and support.

Submitted on March 13, 2010 / Accepted on March 22, 2010

References

1. Müller H. Fractal scaling models of natural oscillations in chain systems and the mass distribution of the celestial bodies in the Solar System. *Progress in Physics*, 2010.
2. Müller H. Fractal scaling models of resonant oscillations in chain systems of harmonic oscillators. *Progress in Physics*, 2009.
3. Feynman R. Very High-Energy Collisions of Hadrons. *Phys. Rev. Lett.*, 1969, v. 23, 1415.
4. Kolombet V. Macroscopic fluctuations, masses of particles and discrete space-time, *Biofizika*, 1992, v. 36, 492–499 (in Russian).
5. Terskich V. The continued fraction method. Leningrad, 1955 (in Russian).
6. Particle listings. Particle Data Group, www.pdg.lbl.gov

Table 2. The measured masses of baryons [6], the calculated *S*-intervals of $\frac{1}{4}$ logarithmic units width and the corresponding calculated mass-intervals.

baryons	measured mass MeV/c^2	mass interval MeV/c^2	*S*-interval	*S*
N-baryons, $S=0$, $I=1/2$				
proton	938.27203 ± 0.00008	815 – 1047	7.375 – 7.625	[7; 2]
neutron	939.565346 ± 0.000023	815 – 1047	7.375 – 7.625	[7; 2]
N(1440)	1420 – 1470	1344 – 1726	7.875 – 8.125	[8]
N(1520)	1515 – 1525	1344 – 1726	7.875 – 8.125	[8]
N(1650)	1645 – 1670	1344 – 1726	7.875 – 8.125	[8]
N(1675)	1670 – 1680	1344 – 1726	7.875 – 8.125	[8]
N(1680)	1680 – 1690	1344 – 1726	7.875 – 8.125	[8]
N(1710)	1680 – 1740	1344 – 1726	7.875 – 8.125	[8]
N(1720)	1700 – 1750	1344 – 1726	7.875 – 8.125	[8]
N(2190)	2100 – 2200	1726 – 2216	8.125 – 8.375	[8; 4]
N(2220)	2200 – 2300	2216 – 2846	8.375 – 8.625	[8; 2]
N(2250)	2200 – 2350	2216 – 2846	8.375 – 8.625	[8; 2]
N(2600)	2550 – 2750	2216 – 2846	8.375 – 8.625	[8; 2]
Δ-baryons, $S=0$, $I=1/2$				
Δ(1232)	1231 – 1233	1047 – 1344	7.625 – 7.875	[8; −4]
Δ(1600)	1550 – 1700	1344 – 1726	7.875 – 8.125	[8]
Δ(1620)	1600 – 1660	1344 – 1726	7.875 – 8.125	[8]
Δ(1700)	1670 – 1750	1344 – 1726	7.875 – 8.125	[8]
Δ(1905)	1865 – 1915	1726 – 2216	8.125 – 8.375	[8; 4]
Δ(1910)	1870 – 1920	1726 – 2216	8.125 – 8.375	[8; 4]
Δ(1920)	1900 – 1970	1726 – 2216	8.125 – 8.375	[8; 4]
Δ(1930)	1900 – 2020	1726 – 2216	8.125 – 8.375	[8; 4]
Δ(1950)	1915 – 1950	1726 – 2216	8.125 – 8.375	[8; 4]
Δ(2420)	2300 – 2500	2216 – 2846	8.375 – 8.625	[8; 2]
Λ-baryons, $S=-1$, $I=0$				
Λ	1115.683 ± 0.006	1047 – 1344	7.625 – 7.875	[8; −4]
Λ(1405)	1406 ± 4	1344 – 1726	7.875 – 8.125	[8]
Λ(1520)	1519.5 ± 1.0	1344 – 1726	7.875 – 8.125	[8]
Λ(1600)	1560 – 1700	1344 – 1726	7.875 – 8.125	[8]
Λ(1670)	1660 – 1680	1344 – 1726	7.875 – 8.125	[8]
Λ(1690)	1685 – 1695	1344 – 1726	7.875 – 8.125	[8]
Λ(1800)	1720 – 1850	1726 – 2216	8.125 – 8.375	[8; 4]
Λ(1810)	1750 – 1850	1726 – 2216	8.125 – 8.375	[8; 4]
Λ(1820)	1815 – 1825	1726 – 2216	8.125 – 8.375	[8; 4]
Λ(1830)	1810 – 1830	1726 – 2216	8.125 – 8.375	[8; 4]
Λ(1890)	1850 – 1910	1726 – 2216	8.125 – 8.375	[8; 4]
Λ(2100)	2090 – 2110	1726 – 2216	8.125 – 8.375	[8; 4]
Λ(2110)	2090 – 2140	1726 – 2216	8.125 – 8.375	[8; 4]
Λ(2350)	2340 – 2370	2216 – 2846	8.375 – 8.625	[8; 2]
Σ-baryons, $S=-1$, $I=1$				
Σ^+	1189.37 ± 0.07	1047 – 1344	7.625 – 7.875	[8; −4]
Σ^0	1192.642 ± 0.024	1047 – 1344	7.625 – 7.875	[8; −4]
Σ^-	1197.449 ± 0.030	1047 – 1344	7.625 – 7.875	[8; −4]
$\Sigma(1385)^+$	1382.8 ± 0.4	1344 – 1726	7.875 – 8.125	[8]
$\Sigma(1385)^0$	1383.7 ± 1.0	1344 – 1726	7.875 – 8.125	[8]
$\Sigma(1385)^-$	1387.2 ± 0.5	1344 – 1726	7.875 – 8.125	[8]
Σ(1660)	1630 – 1690	1344 – 1726	7.875 – 8.125	[8]
Σ(1670)	1665 – 1685	1344 – 1726	7.875 – 8.125	[8]
Σ(1750)	1730 – 1800	1726 – 2216	8.125 – 8.375	[8; 4]
Σ(1775)	1770 – 1780	1726 – 2216	8.125 – 8.375	[8; 4]
Σ(1915)	1900 – 1935	1726 – 2216	8.125 – 8.375	[8; 4]
Σ(1940)	1900 – 1950	1726 – 2216	8.125 – 8.375	[8; 4]
Σ(2030)	2025 – 2040	1726 – 2216	8.125 – 8.375	[8; 4]
Σ(2250)	2210 – 2280	2216 – 2846	8.375 – 8.625	[8; 2]
Ξ-baryons, $S=-2$, $I=1/2$				
Ξ^0	1314.86 ± 0.20	1047 – 1344	7.625 – 7.875	[8; −4]
Ξ^-	1321.71 ± 0.07	1047 – 1344	7.625 – 7.875	[8; −4]
$\Xi(1530)^0$	1531.80 ± 0.32	1344 – 1726	7.875 – 8.125	[8]
$\Xi(1530)^-$	1535.0 ± 0.6	1344 – 1726	7.875 – 8.125	[8]
Ξ(1690)	1690 ± 10	1344 – 1726	7.875 – 8.125	[8]
Ξ(1820)	1823 ± 5	1726 – 2216	8.125 – 8.375	[8; 4]
Ξ(1950)	1950 ± 15	1726 – 2216	8.125 – 8.375	[8; 4]
Ξ(2030)	2025 ± 5	1726 – 2216	8.125 – 8.375	[8; 4]

baryons	measured mass MeV/c^2	mass interval MeV/c^2	S-interval	S
Ω-baryons, $S=-3$, $I=0$				
Ω^-	1672.45 ± 0.29	1344 – 1726	7.875 – 8.125	[8]
$\Omega(2250)^-$	2252 ± 9	2216 – 2846	8.375 – 8.625	[8; 2]
charmed baryons, $C=+1$				
Λ_c^+	2286.46 ± 0.14	2216 – 2846	7.375 – 8.625	[8; 2]
$\Lambda_c(2595)^+$	2595.4 ± 0.6	2216 – 2846	7.375 – 8.625	[8; 2]
$\Lambda_c(2625)^+$	2628.1 ± 0.6	2216 – 2846	7.375 – 8.625	[8; 2]
$\Lambda_c(2880)^+$	2881.53 ± 0.35	2846 – 3654	8.625 – 8.875	[9; −4]
$\Lambda_c(2940)^+$	2939.3 ± 1.5	2846 – 3654	8.625 – 8.875	[9; −4]
$\Sigma_c(2455)^{++}$	2454.02 ± 0.18	2216 – 2846	8.375 – 8.625	[8; 2]
$\Sigma_c(2455)^+$	2452.9 ± 0.4	2216 – 2846	8.375 – 8.625	[8; 2]
$\Sigma_c(2455)^0$	2453.76 ± 0.18	2216 – 2846	8.375 – 8.625	[8; 2]
$\Sigma_c(2801)^{++}$	2801 ± 6	2216 – 2846	8.375 – 8.625	[8; 2]
$\Sigma_c(2800)^+$	2792 ± 14	2216 – 2846	8.375 – 8.625	[8; 2]
$\Sigma_c(2800)^0$	2802 ± 7	2216 – 2846	8.375 – 8.625	[8; 2]
Ξ_c^+	2467.8 ± 0.6	2216 – 2846	8.375 – 8.625	[8; 2]
Ξ_c^0	2470.88 ± 0.8	2216 – 2846	8.375 – 8.625	[8; 2]
$\Xi_c^{\prime+}$	2575.6 ± 3.1	2216 – 2846	8.375 – 8.625	[8; 2]
$\Xi_c^{\prime0}$	2577.9 ± 2.9	2216 – 2846	8.375 – 8.625	[8; 2]
$\Xi_c(2645)^+$	2645.9 ± 0.6	2216 – 2846	8.375 – 8.625	[8; 2]
$\Xi_c(2645)^0$	2645.9 ± 0.5	2216 – 2846	8.375 – 8.625	[8; 2]
$\Xi_c(2790)^+$	2789.1 ± 3.2	2216 – 2846	8.375 – 8.625	[8; 2]
$\Xi_c(2790)^0$	2791.8 ± 3.3	2216 – 2846	8.375 – 8.625	[8; 2]
$\Xi_c(2815)^+$	2816.6 ± 0.9	2216 – 2846	8.375 – 8.625	[8; 2]
$\Xi_c(2815)^0$	2819.6 ± 1.2	2216 – 2846	8.375 – 8.625	[8; 2]
$\Xi_c(2980)^+$	2971.4 ± 3.3	2846 – 3654	8.625 – 8.875	[9; −4]
$\Xi_c(2880)^0$	2968.0 ± 2.6	2846 – 3654	8.625 – 8.875	[9; −4]
$\Xi_c(3080)^+$	3077.0 ± 0.4	2846 – 3654	8.625 – 8.875	[9; −4]
$\Xi_c(3080)^0$	3079.9 ± 1.4	2846 – 3654	8.625 – 8.875	[9; −4]
Ω_c^0	2695.2 ± 1.7	2216 – 2846	8.375 – 8.625	[8; 2]
$\Omega_c(2770)^0$	2765.9 ± 2.0	2216 – 2846	8.375 – 8.625	[8; 2]
bottom baryons, $B=-1$				
Λ_b^0	5620.2 ± 1.6	4692 – 6025	9.125 – 9.375	[9; 4]
Σ_b^+	5807.8 ± 2.7	4692 – 6025	9.125 – 9.375	[9; 4]
Σ_b^-	5815.2 ± 2.0	4692 – 6025	9.125 – 9.375	[9; 4]
Σ_b^{*+}	5829.0 ± 3.4	4692 – 6025	9.125 – 9.375	[9; 4]
Σ_b^{*-}	5836.4 ± 2.8	4692 – 6025	9.125 – 9.375	[9; 4]
Ξ_b	5792.4 ± 3.0	4692 – 6025	9.125 – 9.375	[9; 4]
Σ_b^-	6165 ± 16	6025 – 7736	9.375 – 9.625	[9; 2]

Table 3. The measured masses of mesons [6], the calculated S-intervals of $\frac{1}{4}$ logarithmic units width and the corresponding calculated mass-intervals.

mesons	measured mass MeV/c^2	mass interval MeV/c^2	S-interval	S
light unflavored mesons $S=C=B=0$				
$\pi^\pm$	139.57018 ± 0.00035	110 – 142	5.375 – 5.625	[5; 2]
π^0	134.9766 ± 0.0006	110 – 142	5.375 – 5.625	[5; 2]
η	547.853 ± 0.024	495 – 635	6.875 – 7.125	[7]
$\rho(770)$	775.49 ± 0.34	635 – 815	7.125 – 7.375	[7; 4]
$\omega(782)$	782.65 ± 0.12	635 – 815	7.125 – 7.375	[7; 4]
$\rho'(958)$	957.78 ± 0.06	815 – 1047	7.375 – 7.626	[7; 2]
$f_0(980)$	980 ± 10	815 – 1047	7.375 – 7.626	[7; 2]
$a_0(980)$	980 ± 20	815 – 1047	7.375 – 7.626	[7; 2]
$\phi(1020)$	1019.455 ± 0.020	815 – 1047	7.375 – 7.626	[7; 2]
$a_0(980)$	980 ± 20	815 – 1047	7.375 – 7.626	[7; 2]
$\phi(1020)$	1019.455 ± 0.020	815 – 1047	7.375 – 7.626	[7; 2]
$h_1(1170)$	1170 ± 20	1047 – 1344	7.626 – 7.875	[8; −4]
$b_1(1235)$	1229.5 ± 3.2	1047 – 1344	7.626 – 7.875	[8; −4]
$a_1(1260)$	1230 ± 40	1047 – 1344	7.626 – 7.875	[8; −4]
$f_2(1270)$	1275.1 ± 1.2	1047 – 1344	7.626 – 7.875	[8; −4]
$f_1(1285)$	1281.8 ± 0.6	1047 – 1344	7.626 – 7.875	[8; −4]
$\eta(1295)$	1294 ± 4	1047 – 1344	7.626 – 7.875	[8; −4]
$h_1(1170)$	1170 ± 20	1047 – 1344	7.626 – 7.875	[8; −4]
$b_1(1235)$	1229.5 ± 3.2	1047 – 1344	7.626 – 7.875	[8; −4]
$a_1(1260)$	1230 ± 40	1047 – 1344	7.626 – 7.875	[8; −4]
$f_2(1270)$	1275.1 ± 1.2	1047 – 1344	7.626 – 7.875	[8; −4]
$f_1(1285)$	1281.8 ± 0.6	1047 – 1344	7.626 – 7.875	[8; −4]
$\eta(1295)$	1294 ± 4	1047 – 1344	7.626 – 7.875	[8; −4]
$\pi(1300)$	1300 ± 100	1047 – 1344	7.626 – 7.875	[8; −4]
$a_2(1320)$	1318.3 ± 0.6	1047 – 1344	7.626 – 7.875	[8; −4]
$f_0(1370)$	1200 – 1500	1344 – 1726	7.875 – 8.125	[8]
$\pi_1(1400)$	1351 ± 30	1344 – 1726	7.875 – 8.125	[8]
$\eta(1450)$	1409.8 ± 2.5	1344 – 1726	7.875 – 8.125	[8]
$f_1(1420)$	1426.4 ± 0.9	1344 – 1726	7.875 – 8.125	[8]
$\omega(1400)$	1400 – 1450	1344 – 1726	7.875 – 8.125	[8]
$a0(1450)$	1474 ± 19	1344 – 1726	7.875 – 8.125	[8]
$\rho(1450)$	1465 ± 25	1344 – 1726	7.875 – 8.125	[8]
$\eta(1475)$	1476 ± 4	1344 – 1726	7.875 – 8.125	[8]
$f_0(1500)$	1505 ± 6	1344 – 1726	7.875 – 8.125	[8]
$f_2(1525)$	1525 ± 5	1344 – 1726	7.875 – 8.125	[8]
$\pi_1(1600)$	1662 ± 15	1344 – 1726	7.875 – 8.125	[8]
$\eta_2(1645)$	1617 ± 5	1344 – 1726	7.875 – 8.125	[8]
$\omega(1650)$	1670 ± 30	1344 – 1726	7.875 – 8.125	[8]
$\omega_3(1670)$	1667 ± 4	1344 – 1726	7.875 – 8.125	[8]
$\pi_2(1670)$	1672.4 ± 3.2	1344 – 1726	7.875 – 8.125	[8]
$\phi(1680)$	1680 ± 20	1344 – 1726	7.875 – 8.125	[8]
$\rho_3(1690)$	1688.8 ± 2.1	1344 – 1726	7.875 – 8.125	[8]
$\rho(1700)$	1720 ± 20	1344 – 1726	7.875 – 8.125	[8]
$f_0(1710)$	1720 ± 6	1344 – 1726	7.875 – 8.125	[8]
$\pi(1800)$	1816 ± 14	1726 – 2216	8.125 – 8.375	[8; 4]
$\phi_3(1850)$	1854 ± 7	1726 – 2216	8.125 – 8.375	[8; 4]
$\pi_2(1880)$	1895 ± 16	1726 – 2216	8.125 – 8.375	[8; 4]
$f_2(1950)$	1944 ± 12	1726 – 2216	8.125 – 8.375	[8; 4]
$f_2(2100)$	2011 ± 80	1726 – 2216	8.125 – 8.375	[8; 4]
$a_4(2040)$	2001 ± 10	1726 – 2216	8.125 – 8.375	[8; 4]
$f_4(2050)$	2018 ± 11	1726 – 2216	8.125 – 8.375	[8; 4]
$f_2(2300)$	2297 ± 28	2216 – 2846	8.375 – 8.625	[8; 2]
$f_2(2340)$	2339 ± 60	2216 – 2846	8.375 – 8.625	[8; 2]
strange mesons $S=\pm1 C=B=0$				
$K^\pm$	493.677 ± 0.016	385 – 495	6.625 – 6.875	[7; −4]
K^0	497.614 ± 0.024	385 – 495	6.625 – 6.875	[7; −4]
$K^*(892)^\pm$	891.66 ± 0.26	815 – 1047	7.375 – 7.625	[7; 2]
$K^*(892)^0$	896.00 ± 0.25	815 – 1047	7.375 – 7.625	[7; 2]
$K_1(1270)$	1272 ± 7	1047 – 1344	7.625 – 7.875	[8; −4]
$K_1(1400)$	1403 ± 7	1344 – 1726	7.875 – 8.125	[8]
$K^*(1410)$	1414 ± 15	1344 – 1726	7.875 – 8.125	[8]
$K_0^*(1430)$	1425 ± 50	1344 – 1726	7.875 – 8.125	[8]
$K_2^*(1430)^\pm$	1425.6 ± 1.5	1344 – 1726	7.875 – 8.125	[8]
$K_2^*(1430)^0$	1432.4 ± 1.3	1344 – 1726	7.875 – 8.125	[8]
$K^*(1680)$	1717 ± 27	1344 – 1726	7.875 – 8.125	[8]
$K_2(1770)^\pm$	1773 ± 8	1726 – 2216	8.125 – 8.375	[8; 4]
$K_3^*(1780)$	1776 ± 7	1726 – 2216	8.125 – 8.375	[8; 4]
$K_2(1820)$	1816 ± 13	1726 – 2216	8.125 – 8.375	[8; 4]
$K_4^*(2045)$	2045 ± 9	1726 – 2216	8.125 – 8.375	[8; 4]
charmed mesons $S=\pm1$				
$D^\pm$	1869.62 ± 0.20	1726 – 2216	8.125 – 8.375	[8; 4]
D^0	1864.84 ± 0.17	1726 – 2216	8.125 – 8.375	[8; 4]
$D^*(2007)^0$	2006.97 ± 0.19	1726 – 2216	8.125 – 8.375	[8; 4]
$D^*(2010)^\pm$	2010.27 ± 0.17	1726 – 2216	8.125 – 8.375	[8; 4]
$D_1(2420)^0$	2423.3 ± 1.3	2216 – 2846	8.375 – 8.625	[8; 2]
$D_2^8(2460)^0$	2461.1 ± 1.6	2216 – 2846	8.375 – 8.625	[8; 2]
$D_2^8(2460)^\pm$	2460.1 ± 3.5	2216 – 2846	8.375 – 8.625	[8; 2]

mesons	measured mass MeV/c^2	mass interval MeV/c^2	S-interval	S
charmed, strange mesons $C = S = \pm 1$				
$D_S^{\pm}$	1968.49 ± 0.34	1726 – 2216	8.125 – 8.375	[8; 4]
$D_S^{*\pm}$	2112.3 ± 0.5	1726 – 2216	8.125 – 8.375	[8; 4]
$D_{S0}^{*}(2317)^{\pm}$	2317.8 ± 0.6	2216 – 2846	8.375 – 8.625	[8; 2]
$D_{S1}(2460)^{\pm}$	2459.6 ± 0.6	2216 – 2846	8.375 – 8.625	[8; 2]
$D_{S1}(2536)^{\pm}$	2535.35 ± 0.34	2216 – 2846	8.375 – 8.625	[8; 2]
$D_{S2}(2573)^{\pm}$	2572.6 ± 0.9	2216 – 2846	8.375 – 8.625	[8; 2]
bottom mesons $B = \pm 1$				
$B^{\pm}$	5279.17 ± 0.29	4692 – 6025	9.125 – 9.375	[9; 4]
B^0	5279.50 ± 0.3	4692 – 6025	9.125 – 9.375	[9; 4]
B^*	5325.1 ± 0.5	4692 – 6025	9.125 – 9.375	[9; 4]
$B_1(5721)^0$	5723.4 ± 2.0	4692 – 6025	9.125 – 9.375	[9; 4]
$B_2^*(5747)^0$	5743 ± 5	4692 – 6025	9.125 – 9.375	[9; 4]
bottom, strange mesons $B = \pm 1, S = \pm 1$				
B_S^0	5366.3 ± 0.6	4692 – 6025	9.125 – 9.375	[9; 4]
B_S^*	5415.4 ± 1.4	4692 – 6025	9.125 – 9.375	[9; 4]
bottom, charmed mesons $B = S = \pm 1$				
$B_c^{\pm}$	6277 ± 6	6025 – 7736	9.375 – 9.625	[9; 2]
cc-mesons $B = S = \pm 1$				
$\eta_c(1S)$	2980.5 ± 1.2	2846 – 3654	8.625 – 8.875	[9; −4]
$J/psi(1S)$	3096.916 ± 0.011	2846 – 3654	8.625 – 8.875	[9; −4]
$X_{c0}(1P)$	3414.75 ± 0.31	2846 – 3654	8.625 – 8.875	[9; −4]
$X_{c1}(1P)$	3510.66 ± 0.07	2846 – 3654	8.625 – 8.875	[9; −4]
$h_c(1P)$	3525.67 ± 0.32	2846 – 3654	8.625 – 8.875	[9; −4]
$X_{c2}(1P)$	3556.20 ± 0.09	2846 – 3654	8.625 – 8.875	[9; −4]
$\eta_c(2S)$	3637 ± 4	2846 – 3654	8.625 – 8.875	[9; −4]
$\psi(2S)$	3686.09 ± 0.04	3654 – 4692	8.875 – 9.125	[9]
$\psi(3770)$	3772.92 ± 0.35	3654 – 4692	8.875 – 9.125	[9]
$X(3872)$	3872.3 ± 0.8	3654 – 4692	8.875 – 9.125	[9]
$X(3945)$	3916 ± 6	3654 – 4692	8.875 – 9.125	[9]
$\psi(4400)$	4039 ± 1	3654 – 4692	8.875 – 9.125	[9]
$\psi(4160)$	4153 ± 3	3654 – 4692	8.875 – 9.125	[9]
$\psi(4260)$	4263 ± 9	3654 – 4692	8.875 – 9.125	[9]
$\psi(4415)$	4421 ± 4	3654 – 4692	8.875 – 9.125	[9]
bb-mesons				
$Y(1S)$	9460.30 ± 0.26	7736 – 9933	9.625 – 9.875	[10; −4]
$\chi_{b0}(1P)$	9859.44 ± 0.42	7736 – 9933	9.625 – 9.875	[10; −4]
$\chi_{b1}(1P)$	9892.78 ± 0.26	7736 – 9933	9.625 – 9.875	[10; −4]
$\chi_{b2}(1P)$	9912.21 ± 0.26	7736 – 9933	9.625 – 9.875	[10; −4]
$Y(2S)$	10023.26 ± 0.31	9933 – 12754	9.875 – 10.125	[10]
$\chi_{b0}(2P)$	10232.5 ± 0.4	9933 – 12754	9.875 – 10.125	[10]
$\chi_{b1}(2P)$	10255.46 ± 0.22	9933 – 12754	9.875 – 10.125	[10]
$\chi_{b2}(2P)$	10268.65 ± 0.22	9933 – 12754	9.875 – 10.125	[10]
$Y(3S)$	10355.2 ± 0.5	9933 – 12754	9.875 – 10.125	[10]
$Y(4S)$	10579.4 ± 1.2	9933 – 12754	9.875 – 10.125	[10]
$Y(10860)$	10865 ± 8	9933 – 12754	9.875 – 10.125	[10]
$Y(11020)$	11019 ± 8	9933 – 12754	9.875 – 10.125	[10]

Table 4. The measured masses of leptons [6], the calculated S-intervals of $\frac{1}{4}$ logarithmic units width and the corresponding calculated mass-intervals.

leptons	measured mass MeV/c^2	mass interval MeV/c^2	S-interval	S
electron	0.510998910 ± 0.000000013	0	0	[0]
μ	105.658367 ± 0.000004	86 – 110	5.125 – 5.375	[5; 4]
τ	1776.84 ± 0.17	1726 – 2216	8.125 – 8.375	[8; 4]

Table 5. The measured masses of gauge bosons [6], the calculated S-intervals of $\frac{1}{4}$ logarithmic units width and the corresponding calculated mass-intervals.

gauge bosons	measured mass MeV/c^2	mass interval MeV/c^2	S-interval	S
W	80398 ± 25	73395 – 94241	11.875 – 12.125	[12]
Z	91187, 6 ± 2.1	73395 – 94241	11.875 – 12.125	[12]

Schrödinger-Langevin Equation with PT-Symmetric Periodic Potential and its Application to Deuteron Cluster

Vic Christianto* and Florentin Smarandache†

*Present address: Institute of Gravitaion and Cosmology, PFUR, Moscow, 117198, Russia. E-mail: admin@sciprint.org
†Department of Mathematics, University of New Mexico, Gallup, NM 87301, USA. E-mail: smarand@unm.edu

In this article, we find out some analytical and numerical solutions to the problem of barrier tunneling for cluster deuterium, in particular using Langevin method to solve the time-independent Schrödinger equation.

1 Introduction

One of the most reported problem related to the CMNS (condensed matter nuclear science, or LENR), is the low probability of Coulomb barrier tunneling. It is supposed by standard physics that tunneling is only possible at high enough energy (by solving Gamow function).

However, a recent study by Takahashi (2008, 2009) and experiment by Arata etc. (2008) seem to suggest that it is not impossible to achieve a working experiment to create the CMNS process.

In accordance with Takahashi's EQPET/TSC model [1–3], the proposed study will find out some analytical and numerical solutions to the problem of barrier tunneling for cluster deuterium, in particular using Langevin method to solve the time-independent Schrödinger equation. It is hoped that the result can answer some of these mysteries.

One of the results of recent experiments is the lack of signature of D-D reaction as in standard fusion process; this is part of the reason to suggest that D-D fusion doesn't take place [1]. However, Takahashi suggests new possible reaction in the context of cluster deuterium, called 4D fusion [1–3], this mechanism seems to enable reaction at low temperature (CMNS). His result (2009) can be summarized as follows:

> "The ultimate condensation is possible only when the double Platonic symmetry of 4D/TSC is kept in its dynamic motion. The sufficient increase (super screening) of barrier factor is also only possible as far as the Platonic symmetric 4D/TSC system is kept. Therefore, there should be always 4 deuterons in barrier penetration and fusion process, so that 4d simultaneous fusion should take place predominantly. The portion of 2D (usual) fusion rate is considered to be negligible".

In this respect it can be noted that there are recent reports suggesting that hydrogen cluster can get reaction at very low temperature, forming the condition of superfluidity [4]. This seems to happen too in the context of Takahashi TSC condensate dynamics. Other study worth mentioning here is one that discussed molecular chessboard dynamics of deuterium [5].

The difference between this proposed study and recent work of Takahashi based on Langevin equation for cluster deuterium is that we focus on solution of Schrödinger-Langevin equation [6, 7] with PT-Symmetric periodic potential as we discussed in the preceding paper and its Gamow integral. The particular implications of this study to deuteron cluster will be discussed later.

Another differing part from the previous study is that in this study we will also seek clues on possibility to consider this low probability problem as an example of self-organized criticality phenomena. In other words, the time required before CMNS process can be observed is actually the time required to trigger the critical phenomena. To our present knowledge, this kind of approach has never been studied before, although self-organized criticality related to Schrödinger equation approximation to Burger's turbulence has been discussed in Boldyrev [8]. Nonetheless there is recent study suggesting link between diffusion process and the self-organized criticality phenomena.

The result of this study will be useful to better understanding of anomalous phenomena behind Condensed matter nuclear science.

2 Schrödinger-Langevin equation

The Langevin equation is considered as equivalent and therefore has often been used to solve the time-independent Schrödinger, in particular to study molecular dynamics.

Here we only cite the known Langevin equation [3, p. 29]

$$dX_t = p_t\, dt\,, \tag{1}$$

$$dp = -\partial_x \lambda_0(X_t) dt + K p_t dt + dW_t \sqrt{2TK}\,. \tag{2}$$

Takahashi and Yabuuchi also used quite similar form of the stochastic non-linear Langevin equation [7] in order to study the dynamics of TSC condensate motion.

3 Schrödinger equation with PT-symmetric periodic potential

Consider a PT-Symmetric potential of the form [9, 10]

$$V = K_1 \sin(br)\,, \tag{3}$$

where

$$b = \frac{|m|}{\sqrt{-i-1}}\,. \tag{4}$$

Hence, the respective Schrödinger equation with this potential can be written as follows

$$\Psi''(r) = -k^2(r)\,\Psi(r)\,, \tag{5}$$

where

$$k(r) = \frac{2m}{\hbar^2}[E - V(r)] = \frac{2m}{\hbar^2}\left[E - k_1 \sin(br)\right]. \tag{6}$$

For the purpose of finding Gamow function, in area near x=a we can choose linear approximation for Coulomb potential, such that

$$V(x) - E = -\alpha(x - a)\,. \tag{7}$$

Substitution to Schrödinger equation yields

$$\Psi'' + \frac{2m\alpha}{\hbar^2}(x - a)\,\Psi = 0\,, \tag{8}$$

which can be solved by virtue of Airy function.

4 Gamow integral

In principle, the Gamow function can be derived as follows [11]

$$\frac{d^2y}{dx^2} + P(x)y = 0\,. \tag{9}$$

Separating the variables and integrating, yields

$$\int \frac{d^2y}{y} = \int -P(x)\,dx \tag{10}$$

or

$$y\,dy = \exp\left(-\int P(x)\,dx + C\right). \tag{11}$$

To find solution of Gamow function, therefore the integral below must be evaluated:

$$\gamma = \sqrt{\frac{2m}{\hbar^2}\left[V(x) - E\right]}\,. \tag{12}$$

For the purpose of analysis we use the same data from Takahashi's EQPET model [3,12], i.e. $b = 5.6$ fm, and $r_0 = 5$ fm. Here we assume that $E = V_b = 0.257$ MeV. Therefore the integral becomes

$$\Gamma = 0.218\,\sqrt{m}\int_{r_0}^{b}\sqrt{k_1 \sin(br) - 0.257}\,dr\,. \tag{13}$$

By setting boundary condition (either one or more of these conditions)

(a) at $r = 0$ then $V_0 = -V_b - 0.257$MeV;

(b) at $r = 5.6fm$ then $V_1 = k_1 \sin(br) - 0.257 = 0.257$MeV, therefore, one can find estimate of m;

(c) Using this procedure solution of the equation (11) can be found.

The interpretation of this Gamow function is the tunneling rate of the fusion reaction of cluster of deuterium (for the given data) corresponding to Takahashi data [12], with the difference that here we consider a PT-symmetric periodic potential.

The numerical study will be performed with standard package like Maxima etc. Some plausible implications in cosmology modeling should also be discussed in the future.

Submitted on January 20, 2010 / Accepted on March 04, 2010

References

1. Takahashi A. Basics of the deuteron-cluster dynamics by Langevin equation. In: *Low-Energy Nuclear Reactions and New Energy Technologies Sourcebook*, v. 2, 2010, Chapter 11, 193–217, (*ACS Symposium Series*, v. 1029).
2. Takahashi A. and Yabuuchi N. Study on 4D/TSC condensate motion using non-linear Langevin equation. In: *Low-Energy Nuclear Reactions Sourcebook*, 2008, Chapter 4, 57–83 (*ACS Symposium Series*, v. 998).
3. Takahashi A. Dynamic mechanism of TSC condensation motion. *Proc. Intern. Conf. of Condensed Matter Nuclear Science*, Washington DC, 2008.
4. Mezzacapo F. and Boninsegni M. Structure, superfluidity and quantum melting of hydrogen clusters. arXiv: cond-mat/0611775.
5. Calvert C.R., et al. Quantum chessboards in the deuterium molecular ion. arXiv: quantph/08062253.
6. Zsepessy A. Stochastic and deterministic molecular dynamics derived from the time independent Schrödinger equation. arXiv: cond-mat/0812.4338.
7. Rusov V.D. et al. Schrödinger-Chetaev equation. arXiv: 0810.2860.
8. Boldyrev S. arXiv: hep-th/9610080.
9. Christianto V. and Smarandache F. On PT-symmetric periodic potential, quark confinement, and other impossible pursuits. *Progress in Physics*, 2009, v. 1.
10. Christianto V. and Smarandache F. Numerical solution of biquaternion radical Klein-Gordon equation. *Progress in Physics*, 2008, v. 1; also in: Smarandache F. and Christianto V. (eds.) Hadron models and related new energy issues. InfoLearnQuest Publ., USA, 2008.
11. Coddington E. A. and Levinson N. Theory of ordinary differential equations. Mc Graw-Hill, New York, 1955.
12. Takahashi A. Summary of condensed matter nuclear reactions. *J. Cond. Matter Nuclear Science*, 2007, v. 1.

Smarandache's Cevian Triangle Theorem in The Einstein Relativistic Velocity Model of Hyperbolic Geometry

Cătălin Barbu

"Vasile Alecsandri" College — Bacău, str. Iosif Cocea, nr. 12, sc. A, apt. 13, Romania. E-mail: kafka_mate@yahoo.com

In this note, we present a proof of Smarandache's cevian triangle hyperbolic theorem in the Einstein relativistic velocity model of hyperbolic geometry.

1 Introduction

Hyperbolic geometry appeared in the first half of the 19^{th} century as an attempt to understand Euclid's axiomatic basis for geometry. It is also known as a type of non-Euclidean geometry, being in many respects similar to Euclidean geometry. Hyperbolic geometry includes such concepts as: distance, angle and both of them have many theorems in common.There are known many main models for hyperbolic geometry, such as: Poincaré disc model, Poincaré half-plane, Klein model, Einstein relativistic velocity model, etc. The hyperbolic geometry is a non-Euclidian geometry. Here, in this study, we present a proof of Smarandache's cevian triangle hyperbolic theorem in the Einstein relativistic velocity model of hyperbolic geometry. Smarandache's cevian triangle theorem states that if $A_1B_1C_1$ is the cevian triangle of point P with respect to the triangle ABC, then $\frac{PA}{PA_1}\cdot\frac{PB}{PB_1}\cdot\frac{PC}{PC_1}=\frac{AB\cdot BC\cdot CA}{A_1B\cdot B_1C\cdot C_1A}$ [1].

Let D denote the complex unit disc in complex z - plane, i.e.

$$D=\{z\in\mathbb{C}:|z|<1\}.$$

The most general Möbius transformation of D is

$$z\to e^{i\theta}\frac{z_0+z}{1+\overline{z}_0z}=e^{i\theta}(z_0\oplus z),$$

which induces the Möbius addition $\oplus$ in D, allowing the Möbius transformation of the disc to be viewed as a Möbius left gyrotranslation

$$z\to z_0\oplus z=\frac{z_0+z}{1+\overline{z}_0z}$$

followed by a rotation. Here $\theta\in\mathbb{R}$ is a real number, $z,z_0\in D$, and $\overline{z}_0$ is the complex conjugate of z_0. Let $Aut(D,\oplus)$ be the automorphism group of the grupoid $(D,\oplus)$. If we define

$$gyr:D\times D\to Aut(D,\oplus),\quad gyr[a,b]=\frac{a\oplus b}{b\oplus a}=\frac{1+a\overline{b}}{1+\overline{a}b},$$

then is true gyrocommutative law

$$a\oplus b=gyr[a,b](b\oplus a).$$

A gyrovector space $(G,\oplus,\otimes)$ is a gyrocommutative gyrogroup $(G,\oplus)$ that obeys the following axioms:

(1) $gyr[\mathbf{u},\mathbf{v}]\mathbf{a}\cdot gyr[\mathbf{u},\mathbf{v}]\mathbf{b}=\mathbf{a}\cdot\mathbf{b}$ for all points $\mathbf{a},\mathbf{b},\mathbf{u},\mathbf{v}\in G$;

(2) G admits a scalar multiplication, $\otimes$, possessing the following properties. For all real numbers $r,r_1,r_2\in\mathbb{R}$ and all points $\mathbf{a}\in G$:

G1 $1\otimes\mathbf{a}=\mathbf{a}$,

G2 $(r_1+r_2)\otimes\mathbf{a}=r_1\otimes\mathbf{a}\oplus r_2\otimes\mathbf{a}$,

G3 $(r_1r_2)\otimes\mathbf{a}=r_1\otimes(r_2\otimes\mathbf{a})$,

G4 $\frac{|r|\otimes\mathbf{a}}{\|r\otimes\mathbf{a}\|}=\frac{\mathbf{a}}{\|\mathbf{a}\|}$,

G5 $gyr[\mathbf{u},\mathbf{v}](r\otimes\mathbf{a})=r\otimes gyr[\mathbf{u},\mathbf{v}]\mathbf{a}$,

G6 $gyr[r_1\otimes\mathbf{v},r_1\otimes\mathbf{v}]=I$;

(3) Real vector space structure $(\|G\|,\oplus,\otimes)$ for the set $\|G\|$ of onedimensional "vectors"

$$\|G\|=\{\pm\|\mathbf{a}\|:\mathbf{a}\in G\}\subset\mathbb{R}$$

with vector addition $\oplus$ and scalar multiplication $\otimes$, such that for all $r\in\mathbb{R}$ and $\mathbf{a},\mathbf{b}\in G$:

G7 $\|r\otimes\mathbf{a}\|=|r|\otimes\|\mathbf{a}\|$,

G8 $\|\mathbf{a}\oplus\mathbf{b}\|\leqslant\|\mathbf{a}\|\oplus\|\mathbf{b}\|$.

Theorem 1 The Hyperbolic Theorem of Ceva in Einstein Gyrovector Space *Let* $\mathbf{a}_1,\mathbf{a}_2$, *and* $\mathbf{a}_3$ *be three non-gyrocollinear points in an Einstein gyrovector space* $(V_s,\oplus,\otimes)$. *Furthermore, let* $\mathbf{a}_{123}$ *be a point in their gyroplane, which is off the gyrolines* $\mathbf{a}_1\mathbf{a}_2,\mathbf{a}_2\mathbf{a}_3$, *and* $\mathbf{a}_3\mathbf{a}_1$. *If* $\mathbf{a}_1\mathbf{a}_{123}$ *meets* $\mathbf{a}_2\mathbf{a}_3$ *at* $\mathbf{a}_{23}$, *etc., then*

$$\frac{\gamma_{\ominus\mathbf{a}_1\oplus\mathbf{a}_{12}}\|\ominus\mathbf{a}_1\oplus\mathbf{a}_{12}\|}{\gamma_{\ominus\mathbf{a}_2\oplus\mathbf{a}_{12}}\|\ominus\mathbf{a}_2\oplus\mathbf{a}_{12}\|}\cdot\frac{\gamma_{\ominus\mathbf{a}_2\oplus\mathbf{a}_{23}}\|\ominus\mathbf{a}_2\oplus\mathbf{a}_{23}\|}{\gamma_{\ominus\mathbf{a}_3\oplus\mathbf{a}_{23}}\|\ominus\mathbf{a}_3\oplus\mathbf{a}_{23}\|}\times\\ \times\frac{\gamma_{\ominus\mathbf{a}_3\oplus\mathbf{a}_{13}}\|\ominus\mathbf{a}_3\oplus\mathbf{a}_{13}\|}{\gamma_{\ominus\mathbf{a}_1\oplus\mathbf{a}_{13}}\|\ominus\mathbf{a}_1\oplus\mathbf{a}_{13}\|}=1,$$

(here $\gamma_{\mathbf{v}}=\frac{1}{\sqrt{1-\frac{\|\mathbf{v}\|^2}{s^2}}}$ *is the gamma factor).* (See [2, pp. 461].)

Theorem 2 The Hyperbolic Theorem of Menelaus in Einstein Gyrovector Space *Let* $\mathbf{a}_1,\mathbf{a}_2$, *and* $\mathbf{a}_3$ *be three non-gyrocollinear points in an Einstein gyrovector space* $(V_s,\oplus,\otimes)$. *If a gyroline meets the sides of gyrotriangle* $\mathbf{a}_1\mathbf{a}_2\mathbf{a}_3$ *at points* $\mathbf{a}_{12},\mathbf{a}_{13},\mathbf{a}_{23}$, *then*

$$\frac{\gamma_{\ominus\mathbf{a}_1\oplus\mathbf{a}_{12}}\|\ominus\mathbf{a}_1\oplus\mathbf{a}_{12}\|}{\gamma_{\ominus\mathbf{a}_2\oplus\mathbf{a}_{12}}\|\ominus\mathbf{a}_2\oplus\mathbf{a}_{12}\|}\cdot\frac{\gamma_{\ominus\mathbf{a}_2\oplus\mathbf{a}_{23}}\|\ominus\mathbf{a}_2\oplus\mathbf{a}_{23}\|}{\gamma_{\ominus\mathbf{a}_3\oplus\mathbf{a}_{23}}\|\ominus\mathbf{a}_3\oplus\mathbf{a}_{23}\|}\times\\ \times\frac{\gamma_{\ominus\mathbf{a}_3\oplus\mathbf{a}_{13}}\|\ominus\mathbf{a}_3\oplus\mathbf{a}_{13}\|}{\gamma_{\ominus\mathbf{a}_1\oplus\mathbf{a}_{13}}\|\ominus\mathbf{a}_1\oplus\mathbf{a}_{13}\|}=1.$$

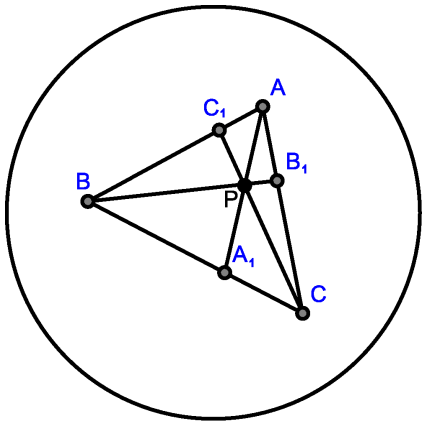

(See [2, pp. 463].) For further details we refer to A. Ungar's recent book [2].

2 Main result

In this section, we present a proof of Smarandache's cevian triangle hyperbolic theorem in the Einstein relativistic velocity model of hyperbolic geometry.

Theorem 3 *If $A_1B_1C_1$ is the cevian gyrotriangle of gyropoint P with respect to the gyrotriangle ABC, then*

$$\frac{\gamma_{|PA|}|PA|}{\gamma_{|PA_1|}|PA_1|}\cdot\frac{\gamma_{|PB|}|PB|}{\gamma_{|PB_1|}|PB_1|}\cdot\frac{\gamma_{|PC|}|PC|}{\gamma_{|PC_1|}|PC_1|}=\frac{\gamma_{|AB|}|AB|\cdot\gamma_{|BC|}|BC|\cdot\gamma_{|CA|}|CA|}{\gamma_{|AB_1|}|AB_1|\cdot\gamma_{|BC_1|}|BC_1|\cdot\gamma_{|CA_1|}|CA_1|}.$$

Proof *If we use a theorem 2 in the gyrotriangle ABC (see Figure), we have*

$$\gamma_{|AC_1|}|AC_1|\cdot\gamma_{|BA_1|}|BA_1|\cdot\gamma_{|CB_1|}|CB_1|=\gamma_{|AB_1|}|AB_1|\cdot\gamma_{|BC_1|}|BC_1|\cdot\gamma_{|CA_1|}|CA_1|. \quad (1)$$

If we use a theorem 1 in the gyrotriangle AA_1B, cut by the gyroline CC_1, we get

$$\gamma_{|AC_1|}|AC_1|\cdot\gamma_{|BC|}|BC|\cdot\gamma_{|A_1P|}|A_1P|=\gamma_{|AP|}|AP|\cdot\gamma_{|A_1C|}|A_1C|\cdot\gamma_{|BC_1|}|BC_1|. \quad (2)$$

If we use a theorem 1 in the gyrotriangle BB_1C, cut by the gyroline AA_1, we get

$$\gamma_{|BA_1|}|BA_1|\cdot\gamma_{|CA|}|CA|\cdot\gamma_{|B_1P|}|B_1P|=\gamma_{|BP|}|BP|\cdot\gamma_{|B_1A|}|B_1A|\cdot\gamma_{|CA_1|}|CA_1|. \quad (3)$$

If we use a theorem 1 in the gyrotriangle CC_1A, cut by the gyroline BB_1, we get

$$\gamma_{|CB_1|}|CB_1|\cdot\gamma_{|AB|}|AB|\cdot\gamma_{|C_1P|}|C_1P|=\gamma_{|CP|}|CP|\cdot\gamma_{|C_1B|}|C_1B|\cdot\gamma_{|AB_1|}|AB_1|. \quad (4)$$

We divide each relation (2), (3), and (4) by relation (1), and we obtain

$$\frac{\gamma_{|PA|}|PA|}{\gamma_{|PA_1|}|PA_1|}=\frac{\gamma_{|BC|}|BC|}{\gamma_{|BA_1|}|BA_1|}\cdot\frac{\gamma_{|B_1A|}|B_1A|}{\gamma_{|B_1C|}|B_1C|}, \quad (5)$$

$$\frac{\gamma_{|PB|}|PB|}{\gamma_{|PB_1|}|PB_1|}=\frac{\gamma_{|CA|}|CA|}{\gamma_{|CB_1|}|CB_1|}\cdot\frac{\gamma_{|C_1B|}|C_1B|}{\gamma_{|C_1A|}|C_1A|}, \quad (6)$$

$$\frac{\gamma_{|PC|}|PC|}{\gamma_{|PC_1|}|PC_1|}=\frac{\gamma_{|AB|}|AB|}{\gamma_{|AC_1|}|AC_1|}\cdot\frac{\gamma_{|A_1C|}|A_1C|}{\gamma_{|A_1B|}|A_1B|}. \quad (7)$$

Multiplying (5) by (6) and by (7), we have

$$\frac{\gamma_{|PA|}|PA|}{\gamma_{|PA_1|}|PA_1|}\cdot\frac{\gamma_{|PB|}|PB|}{\gamma_{|PB_1|}|PB_1|}\cdot\frac{\gamma_{|PC|}|PC|}{\gamma_{|PC_1|}|PC_1|}= \quad (8)$$
$$=\frac{\gamma_{|AB|}|AB|\cdot\gamma_{|BC|}|BC|\cdot\gamma_{|CA|}|CA|}{\gamma_{|A_1B|}|A_1B|\cdot\gamma_{|B_1C|}|B_1C|\cdot\gamma_{|C_1A|}|C_1A|}\cdot\frac{\gamma_{|B_1A|}|B_1A|\cdot\gamma_{|C_1B|}|C_1B|\cdot\gamma_{|A_1C|}|A_1C|}{\gamma_{|A_1B|}|A_1B|\cdot\gamma_{|B_1C|}|B_1C|\cdot\gamma_{|C_1A|}|C_1A|}.$$

From the relation (1) we have

$$\frac{\gamma_{|B_1A|}|B_1A|\cdot\gamma_{|C_1B|}|C_1B|\cdot\gamma_{|A_1C|}|A_1C|}{\gamma_{|A_1B|}|A_1B|\cdot\gamma_{|B_1C|}|B_1C|\cdot\gamma_{|C_1A|}|C_1A|}=1, \quad (9)$$

so

$$\frac{\gamma_{|PA|}|PA|}{\gamma_{|PA_1|}|PA_1|}\cdot\frac{\gamma_{|PB|}|PB|}{\gamma_{|PB_1|}|PB_1|}\cdot\frac{\gamma_{|PC|}|PC|}{\gamma_{|PC_1|}|PC_1|}=\frac{\gamma_{|AB|}|AB|\cdot\gamma_{|BC|}|BC|\cdot\gamma_{|CA|}|CA|}{\gamma_{|AB_1|}|AB_1|\cdot\gamma_{|BC_1|}|BC_1|\cdot\gamma_{|CA_1|}|CA_1|}.$$

Submitted on March 05, 2010 / Accepted on March 26, 2010

References

1. Smarandache F. Eight solved and eight open problems in elementary geometry. arXiv: 1003.2153.
2. Ungar A.A. Analytic hyperbolic geometry and Albert Einstein's Special Theory of Relativity. World Scientific Publishing Co., Hackensack (NJ), 2008.

Progress in Physics **is an American scientific journal on advanced studies in physics, registered with the Library of Congress (DC, USA): ISSN 1555-5534 (print version) and ISSN 1555-5615 (online version). The journal is peer reviewed and listed in the abstracting and indexing coverage of: Mathematical Reviews of the AMS (USA), DOAJ of Lund University (Sweden), Zentralblatt MATH (Germany), Scientific Commons of the University of St. Gallen (Switzerland), Open-J-Gate (India), Referential Journal of VINITI (Russia), etc.** ***Progress in Physics*** **is an open-access journal published and distributed in accordance with the Budapest Open Initiative: this means that the electronic copies of both full-size version of the journal and the individual papers published therein will always be acessed for reading, download, and copying for any user free of charge. The journal is issued quarterly (four volumes per year).**

Electronic version of this journal:
http://www.ptep-online.com

Postal address for correspondence:

Department of Mathematics and Science
University of New Mexico
200 College Road, Gallup, NM 87301, USA

Printed in the United States of America